Fall 2019

The effects of fatigue and weathering on the failure behavior of commercial soda-lime-silicate glass

Erica Ann Ronchetto

Department: Materials Science and Engineering

Recommended Citation

Ronchetto, Erica Ann, "The effects of fatigue and weathering on the failure behavior of commercial soda-lime-silicate glass" (2019). *Doctoral Dissertations*. 2845.
https://scholarsmine.mst.edu/doctoral_dissertations/2845

THE EFFECTS OF FATIGUE AND WEATHERING ON THE FAILURE BEHAVIOR OF COMMERCIAL SODA-LIME-SILICATE GLASS

by

ERICA ANN RONCHETTO

A DISSERTATION

Presented to the Faculty of the Graduate School of the

MISSOURI UNIVERSITY OF SCIENCE AND TECHNOLOGY

In Partial Fulfillment of the Requirements for the Degree

DOCTOR OF PHILOSOPHY

in

MATERIALS SCIENCE AND ENGINEERING

2019

Approved by:

Richard K. Brow, Advisor
Gregory E. Hilmas
Wayne Huebner
Dan Swiler
Chenglin Wu

ABSTRACT

The principle objective of this research is to advance our understanding of the effects of humid conditions on the strength and susceptibility to fatigue of soda-lime silicate (SLS) glass. The two-point bend method was used to evaluate the fatigue characteristics and the degradation of failure strain of fibers drawn from melts of commercial soda-lime silicate glass and exposed to various environmental conditions. Soda lime silicate glasses from two commercial products but with similar nominal compositions were examined. One glass had pristine failure strains about 10% greater than the other, but both had similar fatigue parameters. The fatigue parameter increased from 16 to 25 when SLS glass was exposed to 80% relative humidity (RH), 50°C conditions for 28 days, indicating a decrease in susceptibility to fatigue. However, failure strains decreased by 80%. These results were attributed to changes in the glass surface due to the preferential leaching of alkali ions during weathering. The dealkalized surface was less susceptible to fatigue effects, but the damage induced to these surfaces reduced failure strain. Weathering SLS fibers in 10%RH, 50°C conditions for over 30 days, however, did not change the fatigue parameter, nor did it significantly reduce failure strain. In fact, failure strain increased by about 10% over the first three days of weathering in these conditions. Similar results were also observed for fibers weathered in 40%RH at 50°C and 25°C and were attributed to the dealkalization of the glass surface without the subsequent creation of damage sites that were created after exposure to 50°C/80% RH air.

ACKNOWLEDGMENTS

First and foremost, I sincerely thank my advisor Dr. Richard Brow for his support, generous wisdom, and never-ending patience. He has continually challenged me and guided me over the last eleven years, and I will be forever grateful for what I learned from him and the career opportunities he provided.

I would like to thank my wonderful partner Alex Metcalfe, my family, and my friends for their continued support and love over the years. I would also like to thank my manager, David Schwartz, and colleagues at PARC who supported me taking a leave of absence to finish this work.

This work would not have been possible without the support of the Missouri S&T community. My committee: Gregory E. Hilmas, Wayne Huebner, Dan Swiler, and Chenglin Wu for dedicating time and guidance. Visiting researchers: Qingwei Wang and Francisco Serbena for great discussions and collaborations. Undergraduate students: Austin Stanfield, Luke Verhoff, and Noor Shoaib for their role in this work. Graduate students and post-doctorates: Lina, Xiaoming, Ali, Zea, Katie, Parker, Christian, Luciana, Char, Derek, and Rick for moral support and friendship. The MRC staff: Eric Bohannan, Clarissa Wisner, Jessica Terbush, and Ron Haas for the services and utilities that made this research possible. Lastly, Dr. Mary Reidmeyer for friendship and providing valuable stress relief through the Missouri S&T glass shop.

Finally, I would like to acknowledge Owen-Illinois, Inc. for the financial support of this work, and Dan Swiler, who helped guide these studies and tie them to the needs and interests of the commercial glass industry.

TABLE OF CONTENTS

APPENDICES

LIST OF ILLUSTRATIONS

LIST OF TABLES

1. INTRODUCTION

1.1. GLASS STRENGTH

Glass is a material of choice for applications that depend on its transparency, aesthetic appeal, chemical stability, and manufacturability, but are not constrained by its inherent brittleness [1]. One common general glass composition is soda-lime-silicate (SLS), used in consumer packaging, lighting, architectural, and automotive glazing applications. Demands for lighter, stronger, and more reliable packaging and glazing materials has increased the interest in understanding what determines the theoretical and practical strengths of glass [2]–[4].

1.1.1. Intrinsic Strength of Brittle Materials. The intrinsic strength of a flaw-free material depends on its molecular-level structure [5]. To determine an intrinsic strength, one must first assume that the initiation of failure occurs at the weakest bonds in a structure, generally considered the weakest link in a flawless material [6]. The Condon-Morse description of the bond energy between a cation and anion is a balance of the internuclear repulsion energy and the Coulombic attraction energy between those ions Figure 1.1 shows the Condon-Morse potential energy for two ions as a function of their separation distance, r [7]. The integral of this potential energy curve gives the force required to separate those ions (Equation 1.1):

$$E = \int F dr \tag{1.1}$$

When the net attraction and repulsion forces is equal to zero, and the potential energy is greatest (most negative), the atom spacing is at equilibrium (ro)[7] (Figure 1.1).

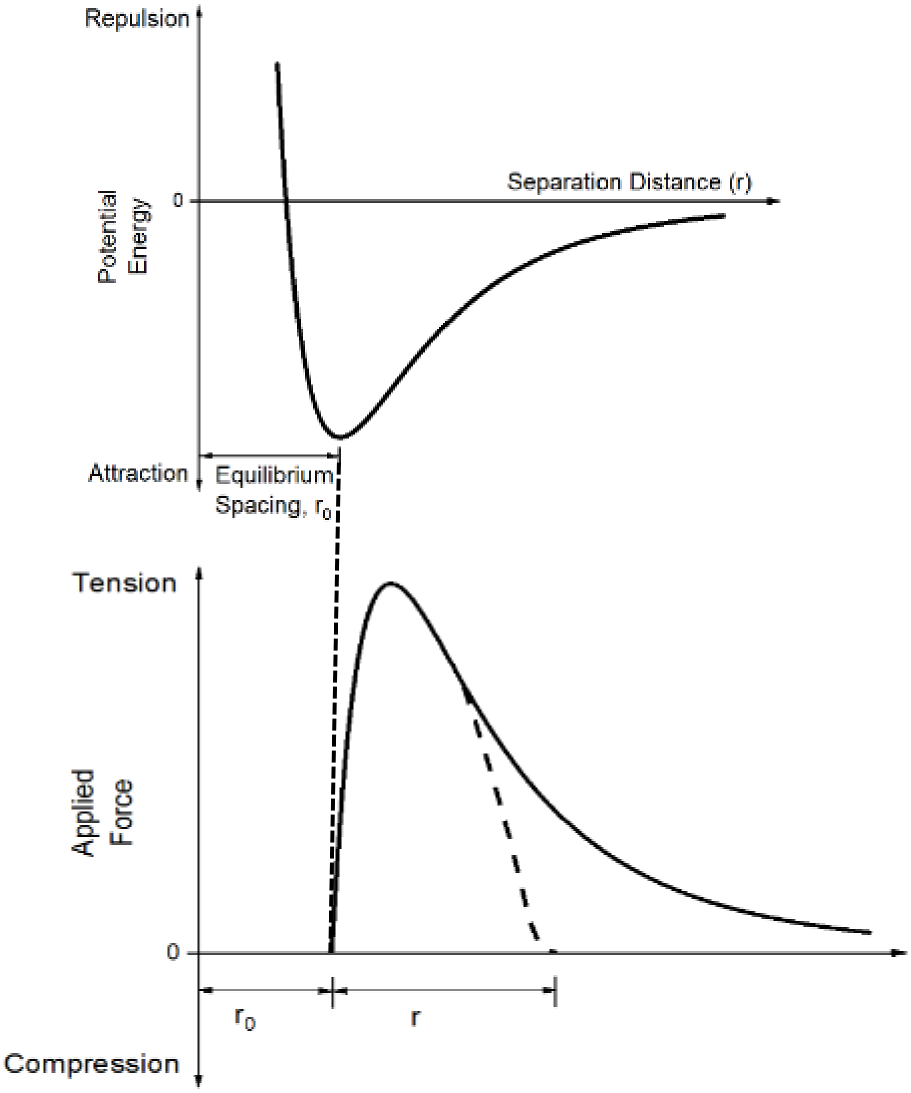

Figure 1.1. Condon-Morse potential energy curve (top) and resulting force required to separate two atoms derived from equation 1 (bottom).

Increasing the separation distance between ions from their equilibrium distances requires an application of force. In a three-dimensional material, this separation will eventually form two new surfaces. To estimate the maximum stress, σ_m, required to separate a bond, Orowan used Hooke's Law (Equation 1.2) and approximated the stress-distance curve as a one-half sine wave (Equation 1.3) where λ is a constant [8].

$$F = -kr \tag{1.2}$$

$$\sigma_m = \sigma \sin(2\pi r/\lambda) \tag{1.3}$$

Orowan defined the area under this approximated force-distance curve to be the work required to separate the atoms and equated this work to that required to create two new surfaces. From this, Orowan developed an expression for the theoretical, intrinsic strength of brittle materials (Equation 1.4)[9]:

$$\sigma_m = (\gamma_0 E/r_0)^{1/2} \tag{1.4}$$

where γ_o is the surface energy per unit area and E is the Young's modulus. The long-range, ordered spacing of atoms in a crystal provides a straight-forward way to apply the Orowan relationship. Glasses, on the other hand, have disordered structures with variations in bond distances and energies, that depend on both the glass composition and the processing conditions[1], and so identifying appropriate values for r_0 becomes problematic.

1.1.2. Extrinsic Factors on Strength of Brittle Materials. The use of Orowan's equation to predict the theoretical strength of brittle materials like glass ultimately results in values orders of magnitude higher than the observed strengths. The stark difference between the theoretical and observed strength is largely attributed to the presence of surface flaws that are created during processing, environmental exposure, and handling. Accurate predictions of glass strength rely heavily on the understanding of flaw and crack behavior in brittle materials. Inglis studied flaw geometry and determined that the local stresses were dependent on flaw shape and size[10]. He calculated that the maximum stress, σ_m (GPa), concentrated on the edge of an elliptical hole in an infinite plate with an applied stress (σ) to be:

$$\sigma_m = 2\sigma\left(\sqrt{c/\rho}\right) \tag{1.5}$$

where *c* is the half-crack length and ρ is the crack tip radius. There are shortcomings to the Inglis relationship. First, it is inadequate for estimating the strengths of pristine materials with atomically sharp defects. (σ_m goes to infinity as ρ approaches zero.) Secondly, it does not take into account the non-linear acceleration of cracks during failure[1].

Griffith used the energy conservation laws of mechanics and thermodynamics to derive a more practical relationship between a critical flaw length (c^*, m) and the failure strength of a brittle material (σ_f, GPa)(Equation 1.6)[11]:

$$\sigma_f = \sqrt{\frac{2\gamma_o E}{\pi c^*}} \tag{1.6}$$

where E is Young's modulus (GPa) and γ_o is surface energy (J/m^2). Griffith balanced the loss in strain energy during fracture with the increase in surface energy. The Griffith equation has been combined with the Orowan and Inglis relationships to predict the theoretical strength (σ_{th}) of brittle materials with atomically sharp flaws:

$$\sigma_{th} = \sigma_m = \sqrt{\frac{E\gamma_o p}{4ca_0}} = \sqrt{\frac{E\gamma_o}{8c}} \tag{1.7}$$

Similar to the Inglis equation, the Griffith equation did not account for the observed acceleration of crack growth with crack size [12]. By considering the increased stress intensity at the crack, Irwin showed that stress fields at the tip of a crack consist of three basic modes: tensile (Mode I), in-plane shearing (Mode II), and out of plane shear (Mode III) (Figure 1.2).

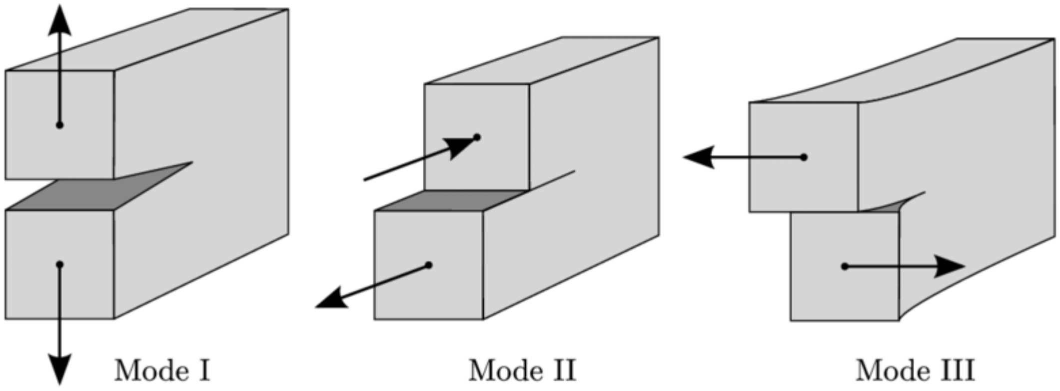

Figure 1.2. Three modes of fracture [13].

Brittle materials typically fail in Mode I, where the direction of tensile stress is normal to the plane of the crack [12]. Each mode has a scaling factor called the stress intensity factor ($K_{I,}$ K_{II}, and $K_{III,}$ respectively) that is derived from the stress fields. When the critical stress intensity factor (K_c) is reached, the crack propagates. In addition to this, Irwin also defined the relationship of the stress intensity factors to the change in strain energy as the crack propagates, known as the strain energy release rate. When the critical stress intensity factor is reached, the critical strain energy release rate is also reached, leading to unstable crack growth[12].

The ability to absorb energy prior to the propagation of a crack is known as toughness, and the critical stress intensity factor is considered a measurement of the facture toughness in a brittle material. The critical stress intensity factor is typically only derived for crystalline materials. For non-crystalline materials, the disordered structure produces inhomogeneous stress fields, and the critical stress intensity factor is thus only an approximation[14]–[16].

1.1.3. Effect of Processing Conditions on Strength. By definition, glass lacks a long-range, homogenous, and stoichiometric lattice structure. There are distributions in the atomic spacing, and the lack of stoichiometry allows for a vast range of practical compositions with tunable properties[1]. To date, it is estimated that over 200,000 compositions have been produced, which is only the merest trifle of the 10^{52} estimated compositions capable of being produced from glass-friendly elements on the periodic table[17]. For each composition, structural variations can be controlled by melting conditions including temperature, time, and atmospheric conditions. As a result, properties that are sensitive to the structure of the glass, including strength and susceptibility to damage, are sensitive to processing conditions.

When a glass melt is cooled below the temperature at which crystals are thermodynamically stable, either the melting temperature of a stoichiometric composition or the liquidus temperature of a non-stoichiometric composition, it becomes a metastable supercooled liquid that continues to relax as a liquid on further cooling (Figure 1.3). Because the viscosity of this supercooled liquid increases on cooling, the time required for the supercooled liquid to relax to the conditions of the new temperature becomes longer. In the glass transition range, this relaxation time becomes long compared with the experimental time, and the properties of the resulting glass diverge from those of the supercooled liquid as it gradually solidifies[18]. This transition is different from the freezing transition of a melt to a crystalline solid which occurs at a thermodynamically distinct temperature. The rate at which a glass-forming melt is cooled affects the structure of the resulting glass. Glass melts cooled through the glass transition range at a faster rate, for example, produce lower density glasses that departed from the supercooled liquid at a greater temperature. Likewise, slowly cooled glasses have enough time to relax to more compact structures at lower temperatures, resulting in a greater density (Figure 1.3). There is a thermodynamic driving force for glasses to continually relax towards the metastable equilibrium of the supercooled liquid, and then rearrange their structures to form a thermodynamically stable crystal, but at rates beyond observation, and so glasses can be considered to be kinetically solid materials[18].

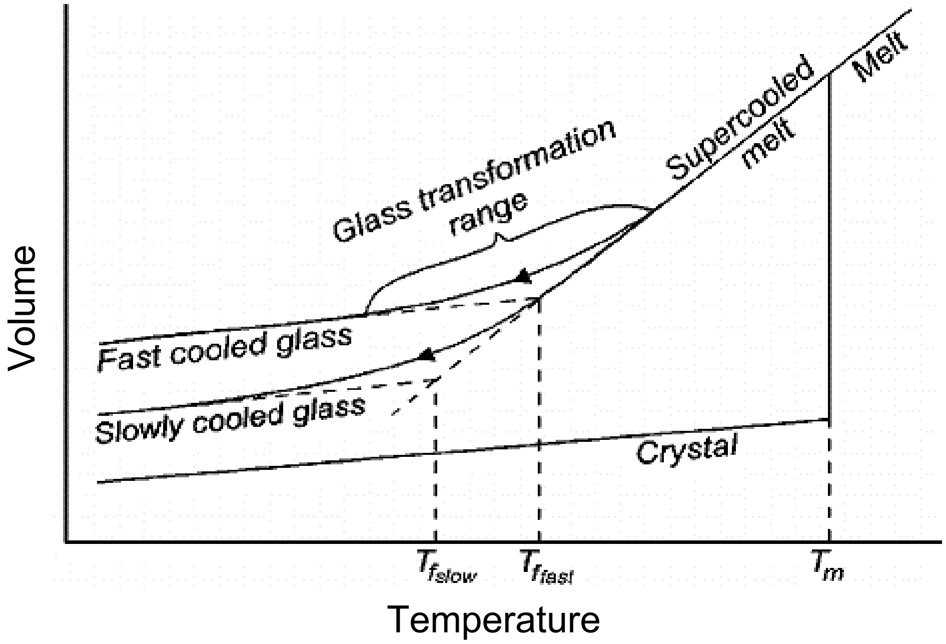

Figure 1.3. Volume-Temperature diagram showing the transition of a metastable supercooled liquid to a glass[19].

The temperature on cooling at which the properties of the material depart from those of the metastable supercooled liquid is called the fictive temperature. The fictive temperature is a useful way to represent the effects of thermal history on the properties of a glass. Rapidly cooled melts that form lower density glasses depart from the supercooled liquid at greater fictive temperatures than those cooled more slowly, creating glasses with lower fictive temperatures (Figure 1.3).

In addition to density, the thermal history (fictive temperature) of a glass affects other strength related properties such as resistance to fatigue and corrosion. Amma et. al. determined that the lower density of SLS glasses with higher fictive temperatures leads to a greater susceptibility to acidic corrosion[20]. However, SLS glasses with a higher fictive temperature have been shown to have slower crack growth rates compared to lower fictive temperature SLS glasses[21], resulting in greater mechanical strengths for higher fictive temperature glasses[22]. This is consistent with other research that has found that high fictive temperature glasses have a greater resistance to fatigue[23], which is a contributing factor to crack propagation in ambient conditions.

Melt homogeneity is another important aspect that dictates the properties of the resulting glass. The thermal history in the glass transition range differs from that of the melt when it is held above the liquidus point. Melt history effects on glass properties have been studied extensively for several glass compositions[24]–[28]. From studies of pristine fibers, it has been shown that when melts are held for longer times at various temperatures above the liquidus temperature, the failure distributions of those fibers become narrower [27], [29], [30],[31]. This has been explained by the presence of fewer heterogeneities in “well-conditioned” melts that might act as ‘critical flaws’ in the glass fibers[11]. The effect of atmosphere on the homogenization rate also plays a critical role. Depending on the composition, faster melt homogenization can be achieved with inert, high/low water content, oxidizing or reducing atmospheres[27], [32], [33].

One topic of interest is how the size, shape, and distribution of structural heterogeneities are affected by melt history and how this information can be used to improve the strength of glass[3]. In most cases, the critical flaws are estimated to have dimensions on the nanometer scale and so cannot be independently identified. Progress has been made in observing propagation of nanoscale critical flaws using atomic force microscopy. Notably, this research has provided insight into water penetration and coalescence of structural voids near the crack tip[34]. Because of the strong influence of heterogeneities on measured strength of glass, it is important to properly homogenize a melt prior to glass formation.

1.1.4. Effect of Environmental Factors on Glass Strength.

The theoretical strength limits of glass have never been observed in real-world applications and rarely observed in controlled research environments. The decrease in practical glass strength is partly due to previously discussed strength-limiting surface flaws that can form due to handling or processing. In addition to flaws, environmental factors can further degrade glass strength. Strength limiting flaws can be created from environmental reactions on glass surfaces in a process called weathering. Glass is also weaker in the presence of water (atmospheric and liquid) due to environmental fatigue. The prevention of flaw creation and environmental degradation focuses primarily around surface treatments of glass products[35], [36]; for example, the deposition of abrasion resistant tin-polymer coatings on container surfaces[37]. Kennedy and Brandt[38] showed that the fatigue sensitivity of a glass depends on its composition, and this revelation has promoted research to understand the compositional and environmental factors that affect the underlying strength of glass[39]–[48].

1.1.4.1. Effect of fatigue.

Fatigue is one of the factors that decrease glass strength. In the 1890s, Grenet observed variances in glass strength that depended on the load and environmental conditions[49]. Subsequently, Charles[38], [50]–[52] systematically studied fatigue effects, which he classified as either static or dynamic fatigue. Static fatigue is measured from the time to failure of a sample under a constant load[50], [53]. Dynamic fatigue is determined by recording the failure strength of a sample tested with different loading rates[51]. In both types of experiments, the failure strength of glass is controlled by the stress corrosion reactions at the tip of a flaw. For environmental fatigue, reactions between water in the environment and strained bonds at crack tip cause slow crack growth until a critical flaw dimension is reached and failure occurs [54]. Fatigue is also observed in pristine samples, indicating that there is also a crack initiation component[55]. This effect is greatly dependent on glass composition as well as the structure of the glass. Soda-lime silicate glasses react and exchange sodium ions from the glass with protons from the environment (Equation 1.8) to extend the flaw length and cause the glass to fail at lower applied stress[56]. Additionally, the increased pH of the ion-exchange accelerates further fatigue reaction, including the hydrolysis of the siloxane bonds that constitute the glass network (Equation

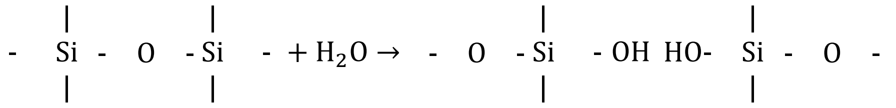

$$-\ \overset{|}{\underset{|}{\mathrm{Si}}}\ -\ \mathrm{O}\ -\overset{|}{\underset{|}{\mathrm{Si}}}\ -\ + \mathrm{H_2O} \rightarrow\ -\ \mathrm{O}\ -\overset{|}{\underset{|}{\mathrm{Si}}}\ -\mathrm{OH}\ \ \mathrm{HO}-\ \overset{|}{\underset{|}{\mathrm{Si}}}\ -\ \mathrm{O}\ -$$

(1.9)[50].

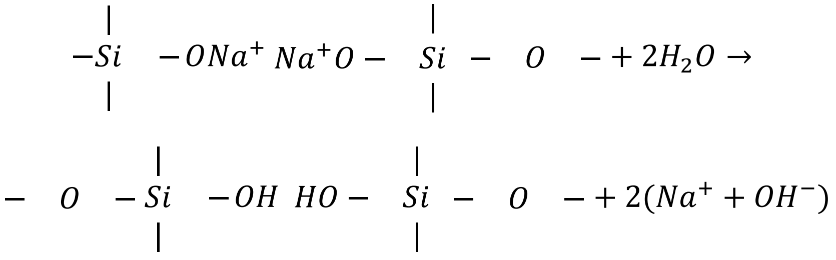

$$-\overset{|}{\underset{|}{Si}}\ -ONa^+\ Na^+O-\ \overset{|}{\underset{|}{Si}}\ -\ O\ -+2H_2O \rightarrow$$

$$-\ O\ -\overset{|}{\underset{|}{Si}}\ -OH\ \ HO-\ \overset{|}{\underset{|}{Si}}\ -\ O\ -+2(Na^+ + OH^-) \qquad (1.8)$$

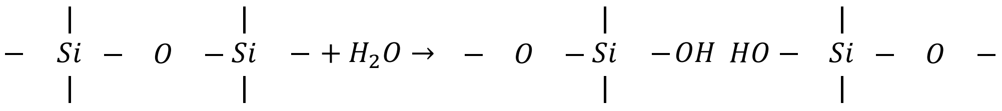

$$-\ \overset{|}{\underset{|}{Si}}\ -\ O\ -\overset{|}{\underset{|}{Si}}\ -+H_2O \rightarrow\ -\ O\ -\overset{|}{\underset{|}{Si}}\ -OH\ \ HO-\ \overset{|}{\underset{|}{Si}}\ -\ O\ - \qquad (1.9)$$

Hydrolysis is the primary fatigue mechanism for silica and other cross-linked glasses [57]. Interestingly, silica is nearly resistant to attack by water under zero strain, and it is only under stress that it undergoes rapid hydrolysis[6].

Eliminating environmental fatigue reactions in order to better understand the intrinsic strength of glass can be difficult. Fatigue reactions depend on humidity, stress rate, and temperature [50], [53]. Increasing humidity and temperature will typically result in faster fatigue reactions and lower failure strains. However, testing at a faster stress rates gives less time for these reactions to occur, resulting in greater failure strain[51].When describing the susceptibility to fatigue reactions of a particular glass composition, a value known as the fatigue parameter is used. This fatigue parameter is a way to quantify the effect of stressing rate at a constant H_2O activity on the failure strength of the glass. The greater this parameter is, the less susceptible a glass is to fatigue.

Slow crack growth studies can be used to determine the fatigue parameter. In a slow crack study, a crack with a predetermined length is introduced to the sample. While applying a constant force to the ends of the crack, the dependence of the crack velocity on the applied stress and environment of the test is measured. The typical results of a slow crack growth study are shown in Figure 1.4, where the initial growth of the crack is due to fatigue reactions previously discussed and is dependent on glass composition [54]. The plateau in crack velocity at greater applied loads is due to limited migration of water to the crack tip, before the initiation of spontaneous crack growth at the critical applied load[54].

From the initial increase in crack velocity, the stress intensity factor, *K*, is derived as a scaling factor for the amplification of applied stress at a crack tip[12]. The relationship between crack growth velocity (*V*) and the stress intensity factor is most commonly described by a model based on an empirical power law[58]:

$$V = A\left(\frac{K}{K_c}\right)^n \tag{1.10}$$

where *A* is an environmental parameter with an Arrhenius temperature dependence and *n* is the fatigue parameter. This power law model was determined to fit slow-crack growth data the best [59], but there are other models based on exponential laws[60]–[62]. For dynamic fatigue studies, the fatigue parameter can be derived analytically from the relationship between failure strength (σ_f) and stressing rate ($\dot{\sigma}$):

$$\sigma_f = D\dot{\sigma}^{(1/(n+1)} \tag{1.11}$$

where *D* is a constant.

To minimize the effects of environmental fatigue, glass strengths have been tested using samples with hermetically sealed coatings and in vacuum environments to eliminate the influence of water[63]–[65]. Another option is to rapidly stress the glass to minimize the time for fatigue reactions to occur, although this is not realistic in ambient laboratory conditions[66]. Water activity can be reduced at low temperatures to arrest fatigue reactions and allow strength measurements to be made at reasonable testing rates[5]. It should be noted that low-temperature tests, often done in liquid nitrogen, are not ever entirely fatigue-free albeit it is accepted that the observed fatigue is near zero and are representative of an inert environment[5].

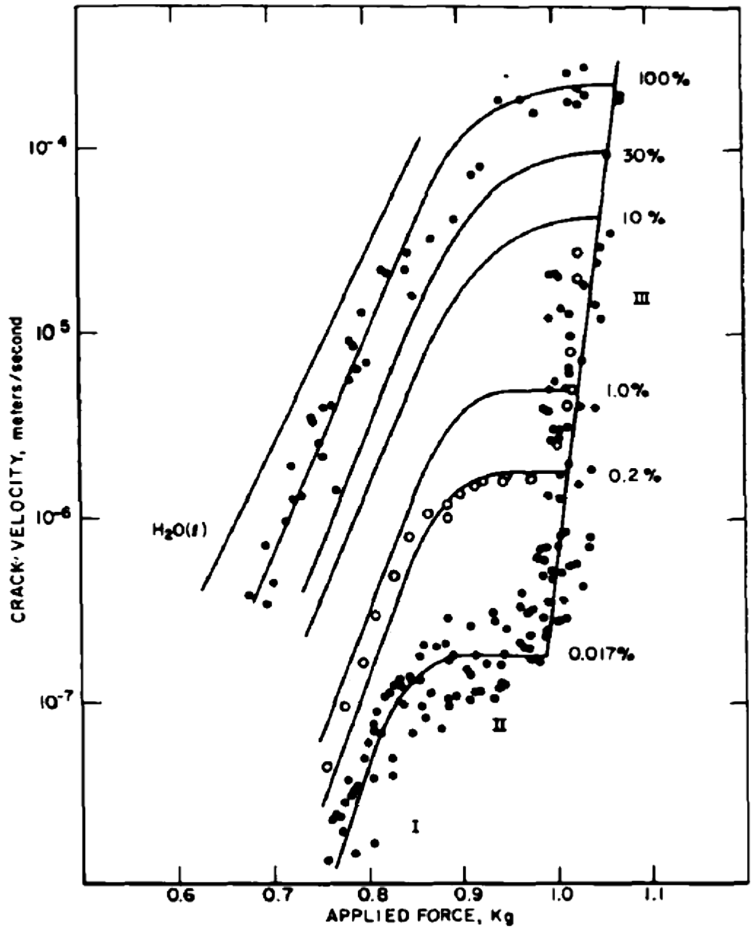

Figure 1.4. Typical results of a slow crack growth study for soda lime silicate glass tested under various humidities at 25°C.[54]

Eliminating environmental fatigue does not result in an absence of fatigue altogether. The concept of inert fatigue is controversial, but there is strong evidence of slow crack growth in inert conditions[5]. Inert fatigue is largely attributed to thermal energy, *kT*, and the probability that it contributes to the rupture of a bond. Theoretically, intrinsic strength could be measured if testing were done close to the vibration time (τ_{vib}) of the material in order to avoid inert fatigue effects. Gupta and Kurkjian proposed the following relationship between testing time (t) and measured strength (σ):

$$\tau = \tau_{vib}\ exp\left[\frac{E(X,C)}{kT}\left(1 - \left\{\frac{\sigma}{\sigma_o(T,C)}\right\}\right)\right] \quad (1.12)$$

where E(X,C) is the zero-stress environment-dependent activation energy for a glass composition (*C*), Boltzmann constant (*k*), test temperature (*T*), strength (σ) measured at the test time (τ) and $\sigma_o(T,C)$ is the fatigue-free strength [5].

1.1.4.2. Development of weathering damage. Flaws can be introduced to the surfaces of glass in many ways, often through handling and impact during the manufacture and use. However, flaws can also develop over time from exposure to the environment in a process called weathering. The decrease in failure strain with weathering time for silicate glasses has been attributed to reactions with water that lengthen critical flaws, reducing strength[27], [67]. Bunker describes three classes of potential reactions that can occur on the surface of a soda-lime-silicate glass with water in the ambient: (1) hydration, (2) hydrolysis, and (3) ion exchange [67]. It is possible in more complex glasses for all three of these reactions to occur simultaneously. Hydration of a glass occurs when a water molecule, H_2O, diffuses into a glass. This requires a certain amount of void space in the glass. Hydrolysis reactions involve the metal-oxygen bonds:

$$H_2O \ + \ M-O-M \rightarrow M-OH \ + \ HO-M \ \rightarrow M-O-M + H_2O \quad (1.13)$$

It should be noted that the hydrolysis reaction will always result in some residual hydroxyl groups since it is not fully reversible. Glasses with modifier cations, such as sodium, experience ion exchange reactions where the modifier ions are preferentially leached from the glass surface due to reactions with water. Some of these reactions are:

$$\text{Si-O-Na}^+ + H_3O^+ \rightarrow \text{Si-OH} + Na^+ + H_2O \qquad (1.14)$$

$$\text{Si-O-Na}^+ + H_2O \rightarrow \text{Si-OH} + Na^+ + OH^- \qquad (1.15)$$

The pH around the reaction sites can change because of these ion-exchange reactions, resulting in changes in the reaction rates at the surface. The ion exchange process is considered the most prevalent initial reaction with alkali containing glasses like soda-lime-silicate exposed to humid environments[68]

For soda-lime-silicate glass, as the ion exchange reactions progress, sodium is leached to the surface of the glass. This produces a silica-rich "gel" layer considerably weaker than the pristine structure (Figure 1.5a and Figure 1.5b). This silica-rich layer itself begins to degrade as the ion exchange process creates an inherently basic environment that accelerates the hydrolysis of siloxane bonds. The thickness and topology of the silica-rich layer can vary depending on whether the glass is exposed to water in atmospheric or aqueous environments. By studying the corrosion in aqueous environments, the rate of growth of the silica-rich layer has been determined to be driven initially by diffusion controlled processes where the rate of growth is proportional to the square root of time[69]. Departure from diffusion-controlled processes occur as the pH of the layer increases and the silica layers then dissolve.

In humid conditions, the leached ions of a soda lime silicate glass accumulate on the surface and consequentially react with environmental species to form a wide variety of crystalline deposits on the surface (Figure 1.5c and Figure 1.5d).

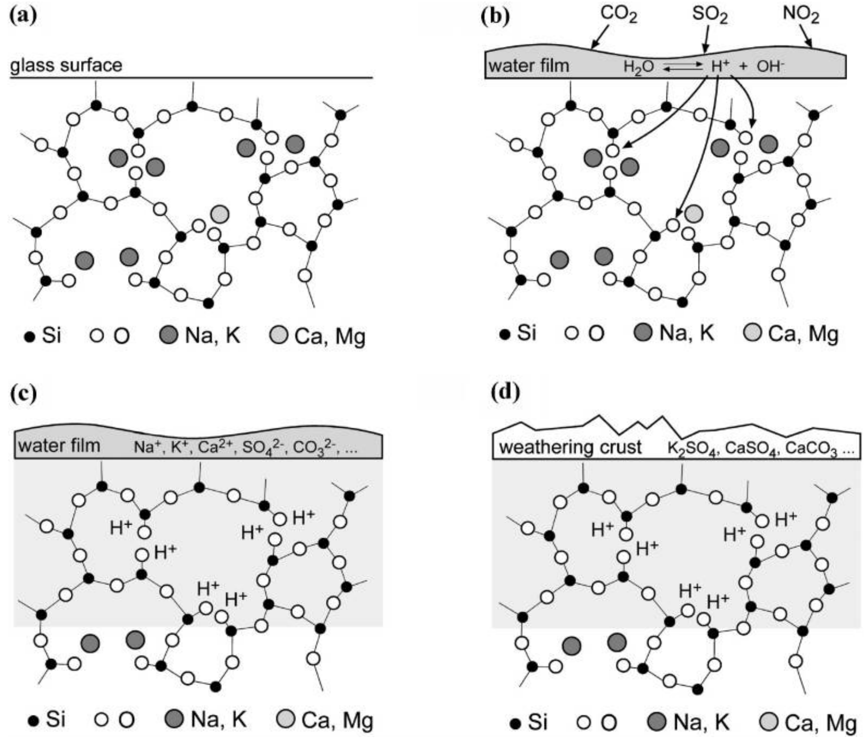

Figure 1.5. Soda-lime-silicate glass weathering process, starting with a) a clean surface, onto which b) a water film is adsorbed, followed by c) the development of an ion deficient silica-rich layer and the enrichment of environmental gases into the water film, and finally d) the precipitation of crystalline weathering products on surface[68].

The most common surface deposits are calcium and sodium carbonates, with metal nitrates and sulfates often forming as well[70], [71]. The link between the formation of crystalline weathering products on the glass surface and their direct effect on critical flaw formation is not fully known due to the inability to directly observe crack initiation and subsequent crack propagation on a glass surface. Micro-pitting has been observed on the surfaces of weathered SLS glass, and was attributed to the growth of crystallites, which were removed prior to imaging[71].

1.1.5. Modeling Strength and Fatigue of Glass. There have been several areas of focus in current glass modeling research, including property-structure prediction, predictive modeling of liquidus temperature and viscosity, glass relaxation, corrosion simulation, and nano-scopic crack initiation and propagation[3]. Because commercial glass is typically composed of several glass formers (SiO_2, Al_2O_3, B_2O_3, etc.) and different modifiers (Na_2O, CaO, K_2O, etc.), with structures that vary widely with thermal history (fictive temperature), it is inherently complex, which makes predicting structure-property relations an ongoing challenge[2], [3]. Smedskjaer, et al. have used topological constraint theory to predict some properties like hardness and ionic diffusion[72]–[74]. This theory considers glass structures as nodes on a network and eliminates considerations that do not affect the macroscopic properties of a glass[1]. However, these models are still relatively simple, ignoring considerations like fictive temperature, structural heterogeneities, and point defects.

Molecular dynamic (MD) simulations have been better adapted to understanding the dependence of mechanical properties on structure and the influence and formation of heterogeneities such as voids. In particular, the inelastic and elastic response of glass to pressure and to tensile stress have been described[6], [75]–[77]. Plastic flow has been observed at indentations and at cracks tips[77]. MD simulations of these phenomena show that SLS glass under uniform pressure behaves like an elastic solid. However, under uni-axial compressive and tensile stresses, Si-O bonds were found to repeatedly break and recombine while the distribution of network modifiers remained the same [78], [79]. On the other hand, when silica, which has a more polymerized structure, was strained in uniaxial tension, structural voids were produced. These results indicate the that controlling structural differences and void formation in silica and modified silicate glasses can suppress crack formation and growth via the increase of plastic flow. Recent advancements in observing crack growth on the nanoscale have supported the molecular dynamic models for void formation and deformation of glass structure under stress[34].

Molecular dynamic models have also been created to study the interactions of water with modified silicate glass bulk and surface structures. Taniguchi and Ito [80] provided new insight into the incorporation of -OH and H_2O in sodium silicate glasses by using MD to model mechanical behavior of ion-substituted hydrous glass (NH) and H_2O molecular-inserted hydrous glass (NM). They found that the NH glass had a significantly lower packing density resulting in easier deformation, and that the –OH groups degrade the mechanical properties of the glass more readily than do the incorporation of H_2O molecules. There have also been developments in simulating the absorption of water on silica glass surfaces and to a lesser extent, on multi-component silicate glass surfaces[81]–[85]. These studies have been used to interpret observed interactions of glass properties such as strength degradation and fatigue resistance.

1.2. MEASURING STRENGTH AND FATIGUE OF GLASS

1.2.1. Traditional Extrinsic Strength Measurements. The mechanical strength of glass can be tested using several traditional methods including tensile tests [27], [45], ring-on-ring test[47], three-point bend test[86], and four-point bend test[87], [88]. These traditional techniques have complications when used to measure the intrinsic strength of glass and are usually chosen to reflect the application of the glass being studied. For tensile testing (Figure 1.7), fibers must be gripped on both ends potentially creating damage and skewing the strength measurements. Another detrimental aspect of the tensile test is that the tested volume and surface area of the fiber are much larger compared to other methods, increasing the likelihood that an extrinsic flaw will determine the strength measured and broaden the distribution of measurements[5].

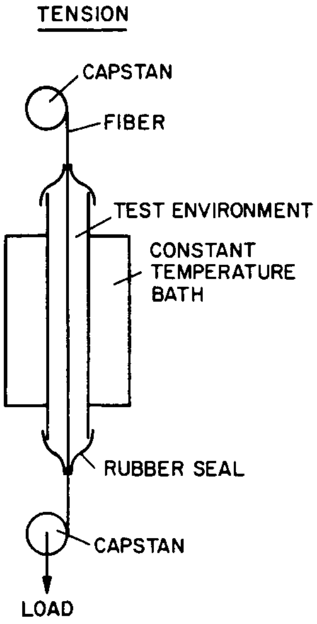

Figure 1.6. Schematic of tensile test for strength measurements of glass fibers.

Flat glass samples are typically evaluated using ring-on-ring or three- and four-point bend tests. Figure 1.6 shows the schematics of the three- and four-point bending set-ups. These tests involve relatively smaller testing volumes than typical fiber tensile tests. However, like tensile testing, these tests still risk creating damage at the points of contact between the glass surface and the testing apparatus. Fracture analysis is often combined with these testing methods as a way to discern whether the origin of fracture is due to the test or is intrinsic with the sample; e.g., bubbles, pre-existing sample damage, etc.

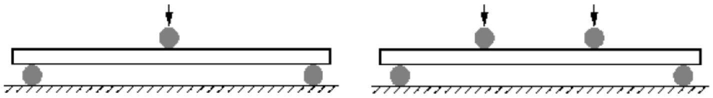

Figure 1.7. Schematic diagram of a three-point bend test (left) and a four-point bend test (right).

1.2.2. Measuring Pristine or Intrinsic Strength of Glass. Many of the studies described above were designed to evaluate the effects of extrinsic flaws and, to a lesser extent, processing-induced variables like inhomogeneity. These measurements were then extrapolated to predict glass material performance in a particular application. Flaw-free samples are needed to study the intrinsic strength of brittle materials like glass. Gupta defined three criteria to determine if the measured strength is intrinsic[89]:

1. There should be no sample size dependence for the measured strength
2. The distribution of measured strengths should be narrow
3. The measured strength should be high

To achieve these criteria, common strategies are to minimize the probability of an extrinsic flaw being included in the testing volume, minimize handling between fabrication and testing to avoid inducing flaws, and/or apply a surface treatment such as an HF rinse to eliminate surface flaws[5], [39], [66]. Glass plate and rod samples tend to be unsuitable due to the processing and handling steps necessary to create the samples prior to the test itself. However, fibers can be processed more quickly than plates or rods and can be tested with less handling. Fibers with a diameter less than 0.5mm can be prepared without residual stresses [90], [91], allowing immediate testing after fiber formation. Fibers are also easy to handle and store to avoid incurring damage to the surface. Due to the ease of handling and fabrication, hundreds of samples can be produced in a fraction of the time required to prepare other sample forms, allowing for large sample sizes that have near identical processing conditions to eliminate variances that can occur for samples that require more extensive processing, such as polishing. Failure studies of fibers have been found to satisfy Gupta's three criteria. Several studies have shown that if a melt is sufficiently homogenized, then there is no dependence of strength on the diameter of the fiber[24], [44]. Additionally, tight distributions of fibers have been observed in both tensile and two-point bend testing. Under inert conditions, the highest observed strength of glass to date have been observed with fibers [41], [92], [93].

Two Point Bend Method. Predecessors to the two-point bend method go as far back as 1950, when Sinclair defined the "loop" method for testing fiber strength by bending a fiber into a loop and closing the loop until failure. This test produced failure strengths that were two or three times greater than were previously achieved. Thirty years later, Matthewson et al. determined the failure strains of silica optical fibers using a refined version of the loop test known as the two-point bend test[91]. The two-point bend (TPB) method is a quick way to evaluate the failure characteristics of glass and poses many advantages over traditional mechanical testing methods. In particular, the fibers are not gripped like they are in a conventional tensile test, but are instead bent into a 'U' shape and placed between two parallel face-plates (Figure 1.8). Fibers can be tested in either dynamic or static conditions, but dynamic conditions are more typical due to the shorter testing times[94], [95]. During a dynamic test, one of the face plates closes at constant velocity, the faceplate velocity (v_{fp}), reducing the gap between the two face plates, increasing the stress on the fiber which is maximized on the outer surface of the "U", until the fiber snaps. The maximum tensile stress is concentrated at the tip of the "U", creating an effective gauge length of microns, instead of millimeters-to-centimeters in a typical tensile test[91], [96]. Faceplate velocities between 50-10,000μm/sec can be achieved with the TPB apparatus used in the present study. An acoustic sensor detects the snap of as broken fiber and the distance between the face-plates (D) at failure is recorded. The diameters (d) of the two broken ends of the fiber are recorded and used to calculate the failure strain, ε_f, using [91]:

$$\varepsilon_f = 1.198\left(\frac{d}{D-d}\right) \tag{1.16}$$

There are several benefits to the TPB technique. As mentioned before, the technique does not require unusual handling or preparation of the fiber samples. Uncoated fibers can be tested in pristine condition, but coated fibers can also be tested. The testing volume is much smaller than those tested using other techniques. The apparatus also allows for easy environmental control, like immersion in liquid nitrogen or water, because the testing set up is compact and easily encased. With other methods, particularly tensile testing, immersion in liquid nitrogen can be difficult.

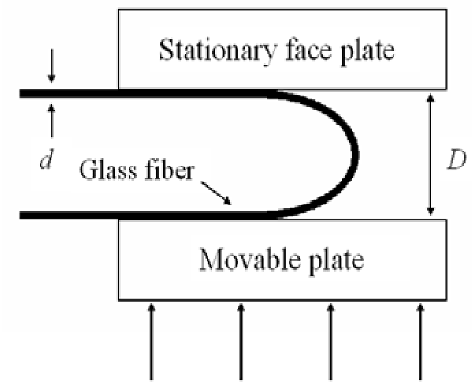

Figure 1.8. Schematic of the two-point bend method test set up.

Due to control of the environmental conditions, a dynamic TPB test can be used to determine the dynamic fatigue parameter ‘n’ with relative ease. With dynamic fatigue, failure strains decrease with increasing relative humidity, decreasing stress/strain rate, or increasing temperature[44]. Shiue and Matthewson[97] compared several models for measuring fatigue in glass using TPB. By fitting various models to the failure strain vs strain rate TPB data, it was determined that a power law model fit the fatigue data the best, although an exponential law model has parameters with better physical meaning. Using the power law model, the slow crack growth and dynamic fatigue studies can be directly compared, which is not possible using the exponential models. Therefore the power law model is widely preferred [44].

Using the TPB method, Rondinella and Matthewson found correlations between fatigue parameters measured at constant strain rates ($\dot{\varepsilon}$), constant stress rates ($\dot{\sigma}$), and constant faceplate velocity rates (v_{fp}) [98]. Rondinella and Matthewson determined 'n' from constant faceplate velocity using equation[98]:

$$n = 1 + \frac{1}{d\left(\frac{\log \varepsilon_f}{\log v_{fp}}\right)} \tag{1.18}$$

where '$d(\log(\varepsilon_f)/d\log(v_{fp}))$' is the slope of the fitted line for each set of data in an average failure strain vs. the faceplate velocity experiment.

There are downsides to the two-point bend method. Data is reported in terms of failure strain because it is difficult to calculate the failure strength of a glass from the failure strains due to the non-linear elastic modulus at failure strains greater than ~2%[99]. Limited data exists to calculate the non-linear elastic behavior of glass because of the difficulty and limitations of measuring the third and fourth order elastic constants with current testing methods[99]. Another downside to the two-point bend method is that the origin of the failure has not been observed because of the extensive damage that occurs to the ends of the fiber on failure. Atomic Force microscopy, optical microscopy, and Scanning Electron microscopy have all failed to identify the failure source of glass fibers[100]. Despite these drawbacks, the TPB technique and its applications has been extensively discussed in the literature[24], [30], [39]–[42], [44], [90], [91], [101], [102].

The two-point bend method has been used in a variety of studies of the failure characteristics of glass. For example, melt history effects have been described for fibers drawn from melts at various temperatures and after different times, to yield a link between melt homogeneity and the resulting distribution of fiber strains. Melting for longer times and at higher temperatures almost always results in narrower distributions and higher failure strains of fibers[27], [44]. However, it was observed that melts with a volatile component eventually produced fibers with broader distributions of failure strains due to the resulting structural heterogeneities[44]. Figure 1.9 shows the average failure strains of commercial SLS glass fibers measured in liquid nitrogen using the two-point bend technique. As time and temperature of melting increase, the failure strains distributions narrow (increasing the Weibull Modulus) and the average failure strains increase. After longer periods of time, although the failure strains see little decrease, the distribution of failure strains begin to broaden (decrease in Weibull modulus).

TPB experiments have also been done to characterize and quantify the inert and environmental fatigue characteristics of different compositions of glass. The fatigue susceptibility of SLS glass is independent of testing humidity whereas silica and E-glass (an alkaline earth aluminoborosilicate glass) showed a clear dependence on humidity (Figure 1.10). The phenomena were attributed to the reaction order increasing with increasing humidity[42]. Studying the inert failure strains of fibers has also yielded new insights into the effect of composition on the failure of glass. Lower studied various alkali silicate, aluminosilicate, and sodium calcium silicate glasses and was able to determine how relatively small changes in glass composition affect the inert failure characteristics [30]. For these glasses, the inert failure strains were shown to increase with increasing modifier content. This trend was attributed to the decrease in Young's modulus with increasing fractions of non-bridging oxygen that constitute the glass structure. The decrease in Young's modulus allowed structures to deform when stressed, allowing for greater failure strains to be achieved (Figure 1.11)[30].

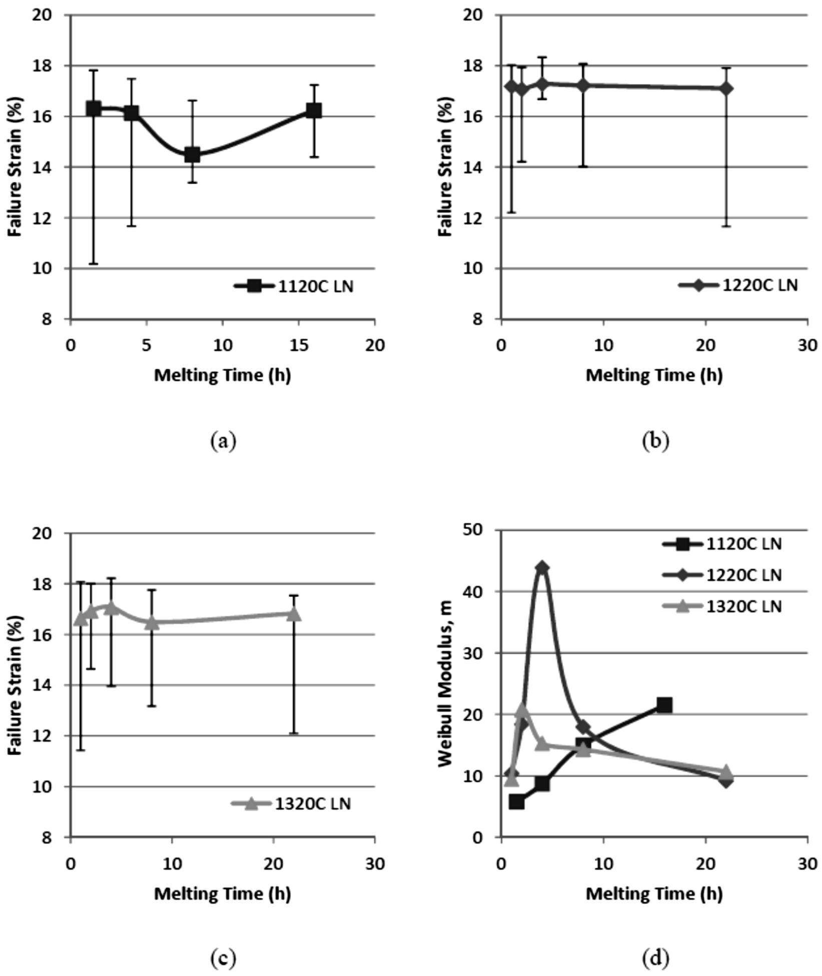

Figure 1.9. Average failure strains of commercial SLS glass fibers measured in liquid nitrogen using two-point bend technique. Fibers were formed from melts homogenized at (a) 1120^{o}C, (b) 1220^{o}C, and (c) 1320^{o}C for varying lengths of time. The corresponding Weibull modulus for these glasses are shown in figure (d).[44]

Most intriguing from TPB studies of inert failure is the observation of the inert delayed failure effect (IDFE)[39]. For 'normal' glasses, like silica, failure strains decrease with decreasing rates of applied stress, a behavior predicted by Gupta and

Kurkjian's description of inert fatigue. However, for 'anomalous' glasses, failure strain increases with decreasing rates of applied stress, as shown for a series of soda-lime silicate glasses in Figure 1.12.[30] Data like this have been used to quantify the IDFE, according to:

$$IDFE = 100 * \frac{(\varepsilon_{f1} - \varepsilon_{f2})}{\varepsilon_{f1}} \tag{1.19}$$

where ε_{f1} and ε_{f2} are failure strains measured at different faceplate velocities (v_{fp}), and $v_{fp}(1) < v_{fp}(2)$.

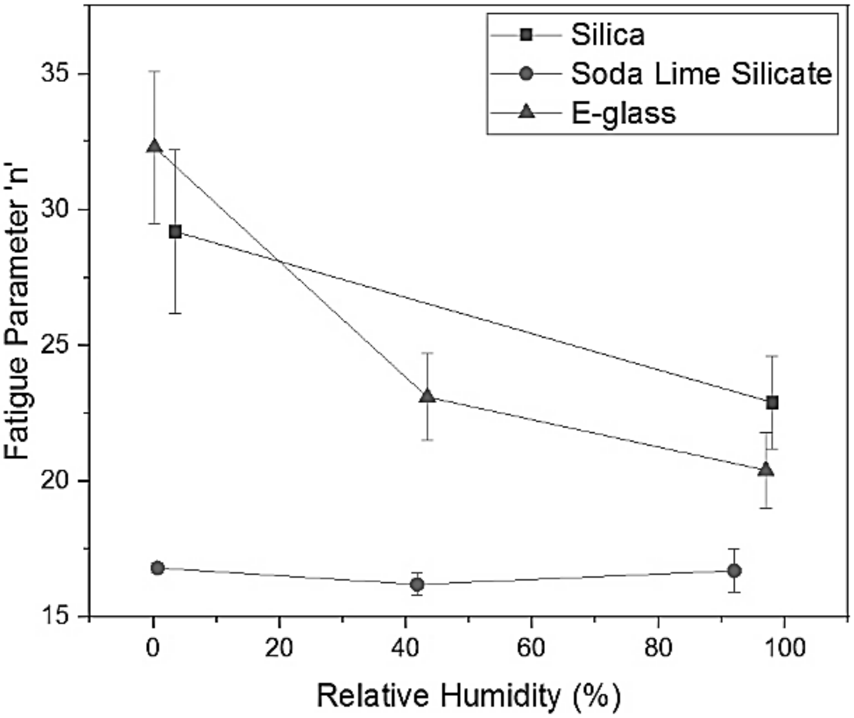

Figure 1.10. Fatigue parameter values for commercial silica, E-glass, and soda-lime silicate glasses. Lines are guides for the eyes[42].

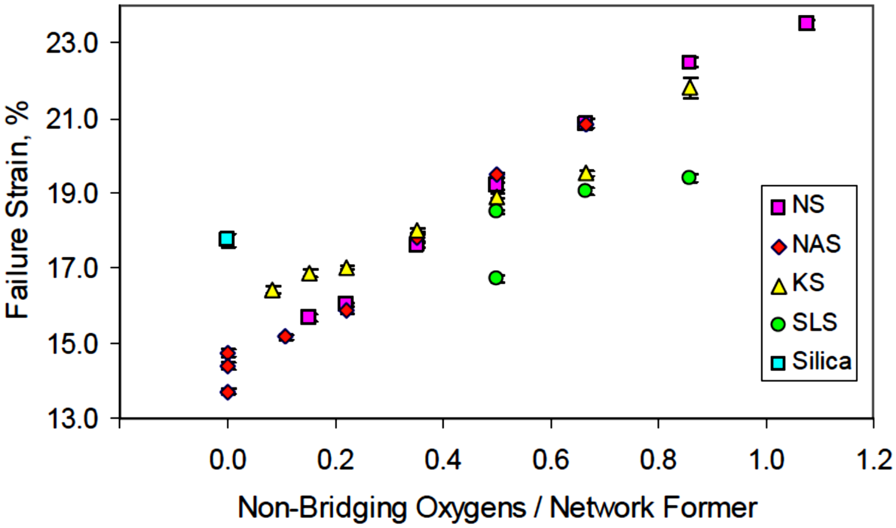

Figure 1.11. The effect of increasing non-bridging oxygens due to increasing modifier content on the failure strains of several glasses. Glasses shown include $v\mathrm{Na_2O}*(1-v)\mathrm{SiO_2}$ (NS), $0.25\mathrm{Na_2O}*w\mathrm{Al_2O_3}*(0.75-w)\mathrm{SiO_2}$ (NAS), $x\mathrm{K_2O}*(1-x)\mathrm{SiO_2}$ (KS), $y\mathrm{Na_2O}*z\mathrm{CaO}*(1-y-z)\mathrm{SiO_2}$, and silica (mol%). All measurements were done in liquid nitrogen with a faceplate velocity of 4000µm/s.

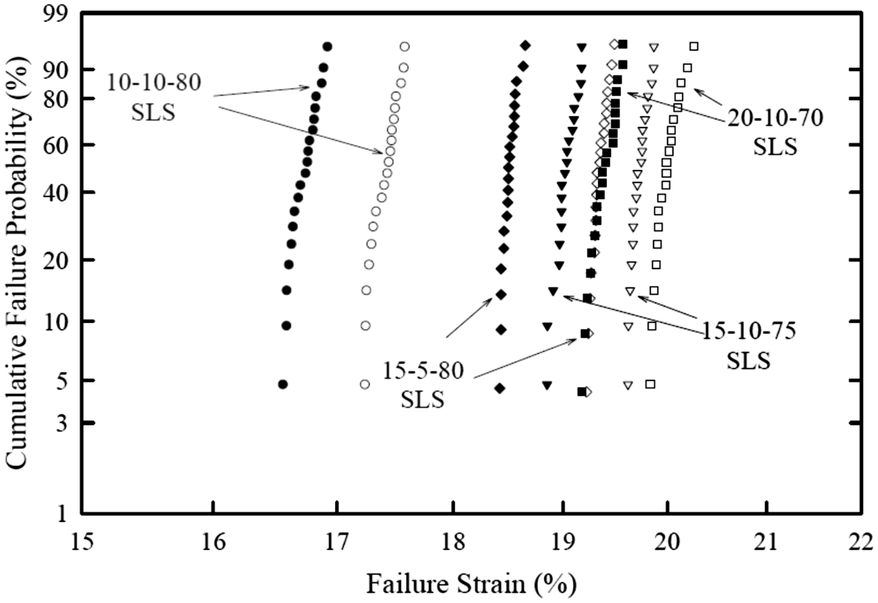

Figure 1.12. Failure strain distributions of fibers from various sodium calcium silicate glass compositions (mol%) measured in liquid nitrogen. Open symbols represent fibers broken with a faceplate velocity of 50µm/s, and closed symbols represent fibers broken with a faceplate velocity of 4000 µm/s.[43]

There is an interesting correlation between IDFE and the indentation behavior of silicate glasses. In anomalous glasses such as silica, diamond indentors densify the glass structure in the indentation zone, whereas in normal glasses like SLS, shear bands are observed [57]. Coincidentally, glasses with a negative IDFE have been classified as 'normal' whereas glasses with a positive IDFE have been classified as 'anomalous'[5]. Table 1.1 summarizes the effects of silicate glass composition on IDFE behavior and elastic anomaly.

Table 1.1. List of IDFE parameters and elastic anomalies for various glasses (mol%) [30]

Glass	IDFE	Elastic Anomaly
Silica (SiO_2)	≤ 0	anomalous
E-Glass	≤ 0	anomalous
Soda-lime-silicate (15%Na_2O, 5%CaO, 80%SiO_2)	> 0	normal
Sodium Silicate (Na_2O < 15%)	≤ 0	anomalous
Sodium Silicate ($Na_2O \geq$ 15%)	> 0	normal
Potassium Silicate (K_2O < 13%)	≤ 0	anomalous
Potassium Silicate (13% < K_2O < 25%)	≤ 0	normal
Potassium Silicate (K_2O > 25%)	> 0	normal

Molecular dynamic models of normal and anomalous glasses support these observations, revealing that alkali modified glasses exhibit increased plastic flow in uniaxial stress, whereas silica responds more like an elastic solid to the applied stress[79]. The indentation and molecular dynamic studies support the theory that anomalous IDFE glasses experience structural reorganization during the slow stressing rates possible under inert conditions[80], [103], [104]. The IDFE effect has also been observed to be greater in glasses that exhibit a lower level of brittleness from indentation studies[39]. Soda lime silicate glasses have been shown as one of these anomalous glasses. Proposed theories suggest densification, plastic flow, or deformation are responsible for the decrease in brittleness. In an effort to observe these structural changes in inert environments, Lower used the TPB system to strain fibers under liquid nitrogen to 90% of the failure strain under liquid nitrogen. When the fibers were removed, no permanent deformation of the bent fibers was observed[30]. However, Yoshida used micro-Raman spectroscopy to reveal stress-induced structural changes near the fracture source of sodium borosilicate fibers (Figure 1.13) [105]. These structural changes included an increase in the average Si-O-Si bond angle and a decrease in the number of Si-O small ring structures.

The TPB technique has also been used to quantify the effect of stress-induced structural changes induced by temperature and water vapor. Lezzi et. al. demonstrated increases in failure strains for fibers held under a tensile load at temperatures above ambient, but lower than the glass transition temperature[106]. This observation was made under both tensile load (silica fibers) and bending load (E-glass and SLS fibers) (Figure 1.14). The increase in failure strains was attributed to the surface of the fiber structurally relaxing while under tension or bending, which induced a surface compression layer. This surface stress relaxation effect was further explored for strained fibers held at elevated temperature in air with different humidity values for extended periods of time[107]. After removal from the fixture, the fibers had residual curvature from the induced residual compressive layer. It was found that this compressive layer could be removed, and the fiber gradually straightened after washing with HF solution. Additionally, they showed a clear increase in residual compressive layer with increased humidity during stressing, which indicates that water plays a crucial role in mechanism of surface stress relaxation. The dependence of the surface stress relaxation phenomenon on the presence of water was attributed stress relief from H_2O reactions on the fiber surfaces, which was observed in both silica and modified silicate glasses[106]. These studies on stress relaxation have given quantifiable explanation into why ion-exchange glasses experience a degradation of strength due to compressive relaxation over time[108].

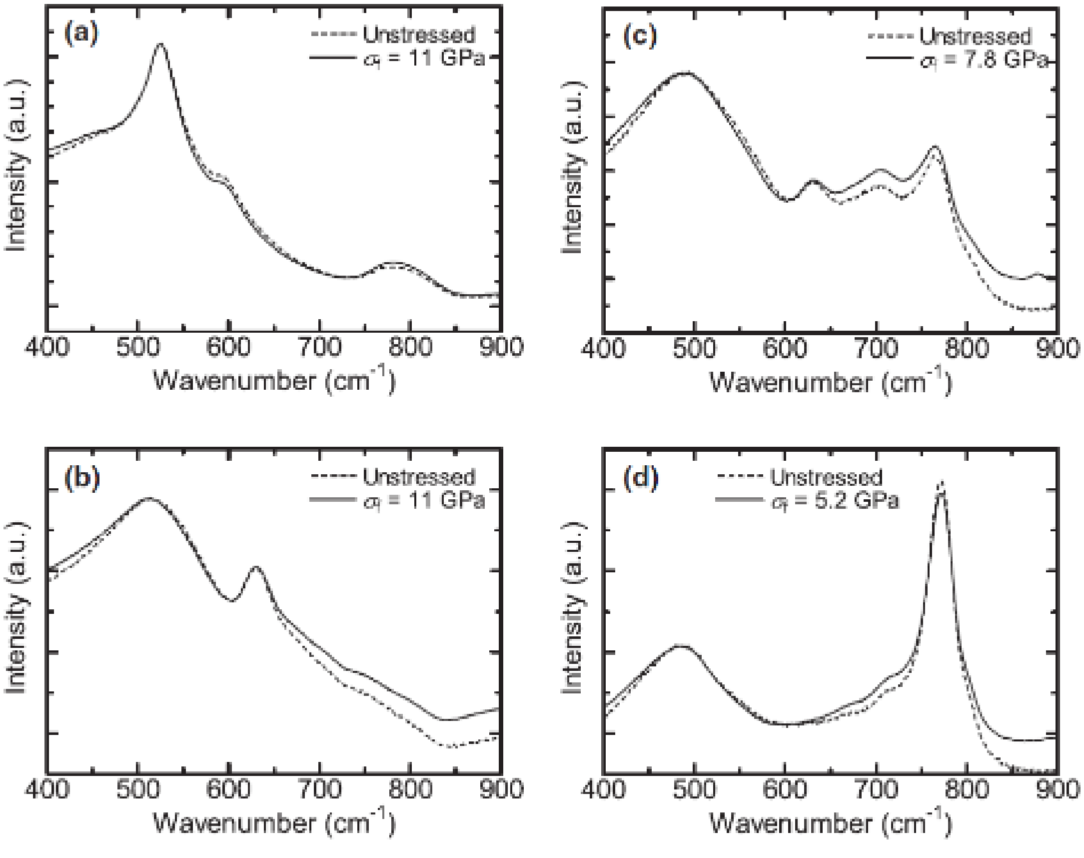

Figure 1.13. Raman spectra of sodium borosilicate fibers with a composition of $1Na_2O$-$40xB_2O_3$-$(80-40x)SiO_2$ where (a) x=0 (b) x=0.5 (c) x=1 (d) x=1.5, before (dotted) and after (solid) deformation in failure using TPB. The estimated fracture stress, σ_f, is noted.

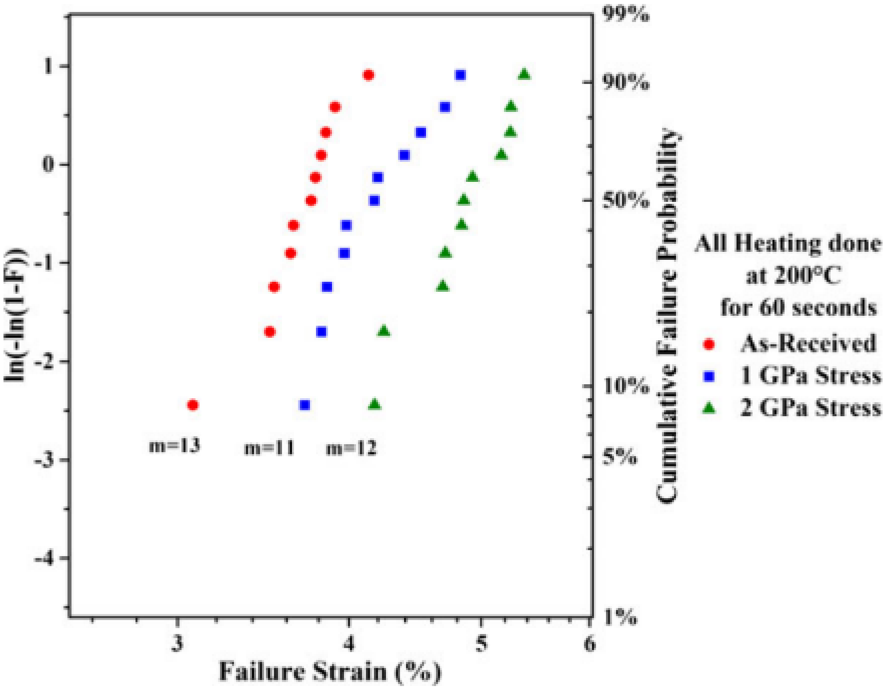

Figure 1.14. Failure strains of 125µm commercial soda-lime silicate glass fibers after applied bending stress while in a 200°C with ~6 Torr H_2O atmosphere[106].

The two-point bend technique has been used to study surface stress relaxation and the compositional dependence of failure and fatigue. Few studies have been done on glass fibers weathered in zero-stress conditions for extended periods of time, which are more representative of storage conditions of commercial glass products. In one study, the TPB technique was used to study the time dependence of mechanical strength degradation of pristine silica fibers under zero-stress. It was determined that at near ambient temperatures, degradation was due to well-known water interactions, but at higher temperatures, the strength degradation was attributed to surface crystallization [109]. Additionally, TPB has been used to study the weathering characteristics of E-glass fibers under various environmental conditions [110], [111]. The fatigue susceptibility of E-glass fibers was shown to be independent of weathering time or conditions despite a marked decrease in failure strains over the 90 day weathering period, and this was attributed to weathering reactions on the fiber surfaces developing critical flaws[110], [111]. These findings indicate that the effect of fatigue decreases over the weathering period as flaws become more consequential. The ability to relate zero-stress weathering mechanisms, mechanical failure, surface degradation, and fatigue susceptibility to each other can reveal valuable information about the long-term performance of glass products.

1.3. SUMMARY

The purpose of this work was to understand the effects of environment and zero-stress weathering on the failure characteristics of commercial soda-lime silicate container glass. The two-point bend method was used to characterize the failure strains of freshly-drawn fibers produced from melts of the commercial SLS glasses. The reproducibility of the pristine fiber fatigue parameter and failure behavior is consistent with respective values reported in the literature. The changes in fatigue behavior, surface characteristics, and failure strains after weathering in ambient air, in 50°C water, 80%RH/50°C air, and 10%RH/50°C air, have been examined. The role of surface reaction layers and the activity of water to the subsequent degradation of mechanical properties is discussed, and changes in fatigue behavior have been related to the reactivity of the weathering conditions. The effects of water incorporated into the glass during processing on the weathering characteristics has also been evaluated. These experiments provide information about the relative sensitivity of glass to fatigue and the mechanisms by which fatigue occurs and provide a means to test whether environmental reactions and forming conditions make a glass more or less susceptible to fatigue. By understanding the sources of fatigue and weathering, strategies for improving, or retaining, the strength of glass objects can be developed.

2. METHODS

2.1. GLASS PREPARATION

Two sources of commercial soda-lime-silicate (SLS) container glass, provided by Owen-Illinois, Inc. (Perrysburg, OH) and designated OI-A (ketchup bottles) and OI-B (spirit bottles), were used in these experiments (Figure 2.1). Both sets of containers came from the same O-I container manufacturing facility but were manufactured about two years apart. The nominal composition of these glasses, provided by the manufacturer, is $13Na_2O$-$11CaO$-$0.5K_2O$-$0.5MgO$-$1Al_2O_3$-$74SiO_2$ (wt%). The bottles were crushed using a steel crusher to produce a coarse powder, with particle sizes between about 50 and 500 microns, as shown in a representative particle size distribution in Figure 2.2. 60g or 160g of cullet was then remelted in a platinum crucible with a volume of 30mL or 84mL, respectively. These masses were selected to provide reproducible fiber diameters from the respective crucibles. Initial experiments with OI-A were done with fibers pulled from the smaller crucible. However, the larger crucible was used to pull larger quantities of fibers from both OI-A and OI-B, required in the later experiments.

All cullet samples were remelted in ambient air except for several melts where the water content was intentionally controlled. All melts were conditioned the same way. The crucible was placed in a furnace at 1000°C and heated at 225°C /hour to 1450°C and held at that temperature for 4 hours. The melt was them cooled to 1220°C, the 1000 P isokom temperature for this glass, and then held for four hours to produce a well-conditioned, bubble-free melt suitable for pulling homogenous fibers. These processing conditions are similar to those used by Tang for drawing homogenized commercial SLS glass fibers [44]. To increase the residual water content of the glass, distilled water was added to the cullet in the platinum crucible until the water level was at the top of the crucible. The crucible was then melted in a furnace under a cap of humid air that was bubbled through 70°C water. To obtain low water content melts, some cullet was melted in a vacuum furnace (~135 torr) at 1100°C for 1 hour. The low water content melt was cooled to room temperature and then transferred to a high temperature furnace at 1000°C, heated at 225°C /hour to 1450°C under a cap of dry argon gas and held at that temperature for 4 hours.

Figure 2.1. Soda-lime silicate bottles designated OI-A (left) and OI-B (right).

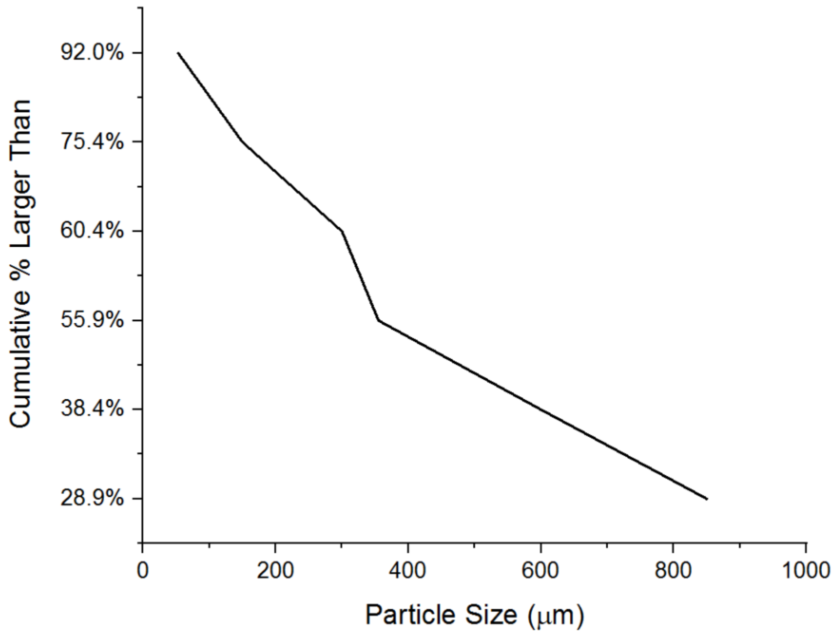

Figure 2.2. Cumulative mass (greater than) distribution of cullet size after crushing.

2.2. FIBER FORMATION

A well-conditioned, bubble free melt was transferred to a furnace located below the fiber-pulling mechanism and the temperature of this furnace was set based on the crucible size and melt viscosity; the latter varied with residual water content. Pulling temperatures are summarized in Table 2.1. A water-cooled copper coil was lowered to about 4 cm above the crucible through a hole in the top of the furnace. The copper coil controled the fiber surface viscosity to ensure a continuous and consistent pull. The fiber pulling system is shown in (Figure 2.3).

A silica glass rod was used to draw the initial fiber from the melt surface through the copper coil and straight up onto a rotating cage positioned above the furnace (Figure 2.3). Double-sided tape was used to secure the drawn fiber to the cage allowing the cage to draw the fiber upwards and around the cage as it rotated. The cage moved 1.6mm horizontally per rotation to separate the fibers as they are drawn to ensure a pristine surface condition. Two different cages were used. The cage shown in Figure 2.3 was used only for pristine fibers that were tested immediately after drawing. For fibers used in the weathering experiments, a cage with removable racks, shown in Figure 2.4, was used.

Table 2.1. Pulling temperatures for glass melt.

Crucible Size	Water Content	Pulling Temperature
30mL	Average	1120°C
84mL	Low	1100°C
84mL	Average	1090°C
84mL	High	1075°C

The fiber diameter was monitored by eye throughout the entire fiber pulling process. Fiber diameters could be adjusted by increasing the temperature of the crucible furnace, the fiber drawing speed, or adjusting the height of the copper cooling coil relative to the melt surface. For a typical run, the furnace temperature was increased approximately 10°C every 5 minutes to maintain a consistent fiber thickness. The pulling temperature was dependent on crucible size because the larger crucible retained more heat during fiber pulling and therefore was not as sensitive to the temperature of the furnace at the start of pulling. Water content of the glass affects the viscosity of the melt and therefore the high and low water content glasses required different pulling temperatures (Table 2.1). If the fibers were initially drawn too thin or too thick, the copper cooling coil was lowered or raised, respectively. In the early experiments with OI-A, the cage rotation speed was also adjusted to maintain a consistent fiber diameter.

However, for later experiments with OI-B, the cage rotation speed was held constant, in the range of 1.5-2 m/s. Roughly 1800 samples, ten centimeters long, could be drawn from a single large cullet melt.

Figure 2.3. The fiber pulling system.

Pulling conditions were adjusted to draw fibers with a consistent diameter of 125±25µm over the 15-minute drawing period. Fiber diameters were measured with an Mitutoyo micrometer. At the conclusion of a run, the diameters of ten fibers distributed across the cage were measured and if these diameters did not fall in the range of 125±25µm, the run was scrapped. There were practical issues to avoid testing fibers outside of this preferred range. Fibers with diameters less than about 100 µm were difficult to test because they failed at faceplate separation distances smaller than what could be obtained without running the risk of forcing the faceplates together. Fibers with diameters greater than about 150 μm could be tested without issue when pristine but were difficult to test after prolonged weathering. The first 10 rows of fibers were always discarded because the diameters were typically too small at the start of a draw. Occasionally, the last 10% of the fibers drawn from a cooler melt were considerably thicker the rest of the draw. These fibers were also discarded.

Figure 2.4. The removable frame cage for fiber pulling.

2.3. WEATHERING FIBERS

Fibers were either tested immediately in their pristine state or weathered under zero-stress conditions in controlled environments, before testing. Some fibers were aged in distilled water by immersing the fiber racks in a water-filled container that was sealed and then held in an environmental chamber (VWS Scientific Humidity Cabinet) set at 50°C. Other fibers were weathered in 10%RH/50°C and 80%RH/50°C air; dry or wet air was moved through the respective environmental chamber (Lindberg Blue and VWS Scientific Humidity Cabinet). Fibers weathered in ambient conditions were stored in a vented container on a laboratory bench.

2.4. TWO-POINT BEND TESTING OF FIBERS

The failure strains of pristine and weathered fibers were determined using a custom-built two-point bending (TPB) system [42,84] (TNL Tool and Technology, LLC). A fiber was removed from the rack by handling the ends to prevent contact to the surfaces in the middle of the sample where the maximum stress was applied during testing. The first fiber tested was taken from the left side of a rack, the second fiber tested was taken from the middle of a rack, and the third fiber was taken from the right side of the rack. This order was repeated until at least 20 fibers were tested from each rack. Each fiber was bent into a 'U' shape and placed between the two parallel face-plates of the TPB system. One of the face plates was then closed at a constant velocity, the faceplate velocity (v_{fp}), reducing the gap distance between the two face plates, increasing the stress applied to the outer tip of the bent fiber until the fiber failed. An acoustic sensor detected the fiber failure and the distance between the face-plates (D) at failure was recorded. The fiber diameter (d) at the two broken ends of the fiber was measured using a Mitutoyo digital micrometer, with a resolution of 0.001 mm, and recorded. The failure strain, ε_f, was then calculated using[48]:

$$\varepsilon_f = 1.198\left(\frac{d}{D-d}\right) \tag{2.1}$$

Faceplate velocities were varied between 100-10,000μm/sec. The relative humidity during testing was controlled by an air handling system that mixes dry and wet air to achieve the desired relative humidity. Air with the desired humidity flowed through a shroud that covered the TPB face plates and was allowed to equilibrate for 30 seconds prior to the start of each measurement made in air. The relative humidity was measured during this time with a digital psychrometer [Extech RH305] with an accurate measurement range between 5-85%±3%RH. Failure strains were also measured after immersing the fiber-loaded TBP face plates in a container of liquid nitrogen. During liquid nitrogen testing, the ambient relative humidity was kept lower than 30% to avoid formation of frost on the TPB fixture. The TPB fixture was periodically warmed to room temperature and water condensation was removed before the next test.

2.5. STATISTICAL ANALYSIS OF FAILURE STRAINS

2.5.1. Weibull Statistics. Weibull statistics were used to describe the distributions of failure strain data acquired by two-point bend testing. The Weibull modulus, m, is a parameter that describes the critical flaw density in the set of samples. Weibull proposed that the risk of failure is proportional to a function of the stress, *f(σ)*, in the volume of a body[112]:

$$f(\sigma) = \left(\frac{\sigma}{\sigma_0}\right)^m \tag{2.2}$$

where σ_o is a characteristic strength which is dependent on the distribution function and m, known as the Weibull modulus, is a constant describing the material homogeneity. A high Weibull modulus is derived from tight failure distributions which are a result of uniform critical flaw distributions.

Weibull statistics were used to describe the failure probability of the glass fibers at various strains. To determine the Weibull modulus from the TPB data, the cumulative failure probability was plotted against the natural logarithms of failure strain, ε_f, and the Weibull modulus (m) was determined from the slope of the resulting distributions:

$$m = \frac{\ln\left(ln\left(\frac{1}{P_S}\right)\right)}{\ln(\varepsilon_f)} \tag{2.3}$$

where P_s is the probability of survival and was determined using:

$$P_s = 1 - \frac{i-0.5}{n} \tag{2.4}$$

Weibull statistics were determined to be suitable for analyzing fiber failures strains because the natural log of the failure strain to double natural log of the failure probability data was usually linear.

2.5.2. One-Way ANOVA and Statistical Significance Analysis. When comparing two independent sets of failure strains, a two-sample T-test was used to determine the significance of the differences in the means of the two sets. For three or more independent failure strain distributions, one-way analysis of variance (ANOVA) was used to determine the statistical significance of any differences. Origin 2018 software was used to calculate the significance levels for both the T-test and one-way ANOVA.

2.6. SURFACE CHARACTERIZATION OF FIBERS

Fiber surfaces were imaged using a FEI Helios NanoLab 600 DualBeam scanning electron microscope. Two-centimeter sections of fibers were attached to a graphite adhesive surface and then coated with Gold/Palladium (Denton Vacuum Coating System). At least three fibers from each experimental data set were examined. In some cases, fibers were first washed by dipping for five seconds, three times, in distilled water to remove crystalline deposits prior to SEM analysis. The fibers were examined using a voltage of 5kV and magnification range of 500x- 20,000x. Atomic Force Microscopy (AFM) was also used to image fiber surfaces and to measure the surface roughness. The AFM was a Nanoscope IIIa Scanning Probe Microscope.

Quantitative compositional analyses were done with energy dispersive x-ray spectroscopy (EDS. The Helios SEM has an Oxford Energy Dispersive X-ray Spectrometer. Fiber surfaces were examined using a 7kV voltage over the area of interest. Oxford's INCA software and database were used to analyze EDS peaks and intensities and perform x-ray compositional mapping.

Raman Spectroscopy measurements were made with either a Horiba Jobin Yvon LabRAM Aramis or a Horiba Jobin-Yvon Xplora µRaman spectrometer. Fibers were taped to a glass microscope slide. For the Aramis system, a 632.5nm HeNe laser was focused onto the surface with a 10x objective. For the Xplora system, a 532nm laser was focused onto the surface with a 10x objective

A Continuum Infrared Microscope was used to collect IR spectra from polished glass patties to estimate residual water contents. To make the glass patties, the glass melts after fiber drawing were immediately reheated in a furnace at 1450°C for 15min and then poured into three-inch diameter glass patties on a steel plate. The patties were annealed at 550°C for 2 hours before cooling to room temperature and cut into ~1 inch square samples. The samples were then polished to a 2500 grit finish using progressively finer SiC polishing pads and kerosene as a non-aqueous lubricant. The final samples were ~3mm thick.

3. FATIGUE AND FAILURE CHARACTERISTICS OF PRISTINE COMMERCIAL SODA-LIME-SILICATE GLASS

3.1. OVERVIEW

Multiple trials were done on pristine samples of both OI-A and OI-B to determine the reproducibility of the failure strain measurements. Each trial was a set of at least 20 fibers drawn from separate melts processed in ambient conditions, and the measurements were made over the course of three years. In addition, melts from OI-B glass were prepared either under vacuum (OI-BV) or in water-saturated conditions (OI-BH) to vary the residual water contents of the glass, compared to melts processed under ambient conditions. Failure strain distributions of OI-A and OI-B fibers were determined in room temperature (25°C) air and relative humidities (RH) controlled between 10%-80%, and under liquid nitrogen. The fatigue parameter was determined for both OI-A and OI-B under different values of RH, using failure strains collected at different faceplate velocities. OI-BV and OI-BH failure strains were determined in room temperature air at 40% RH and in liquid nitrogen, and their fatigue parameters were determined in room temperature air at 40%RH.

3.2. RESULTS

3.2.1. Reproducibility of Failure Strain Distributions. Figure 3.1 shows the distributions of failure strains collected in 40%RH/25°C air and under liquid nitrogen for five trials of OI-A. With a 95% confidence, there are no significant differences between the means of the five trials for either respective testing condition. Fibers tested in liquid nitrogen have much higher failure strains than those tested in 40%RH/25°C air. Fibers tested in ambient conditions had tighter failure strain distributions, and so greater average Weibull moduli (49.6 – 68.6), than those tested in liquid nitrogen (m=24.4 – 29.7) (Table 3.1).

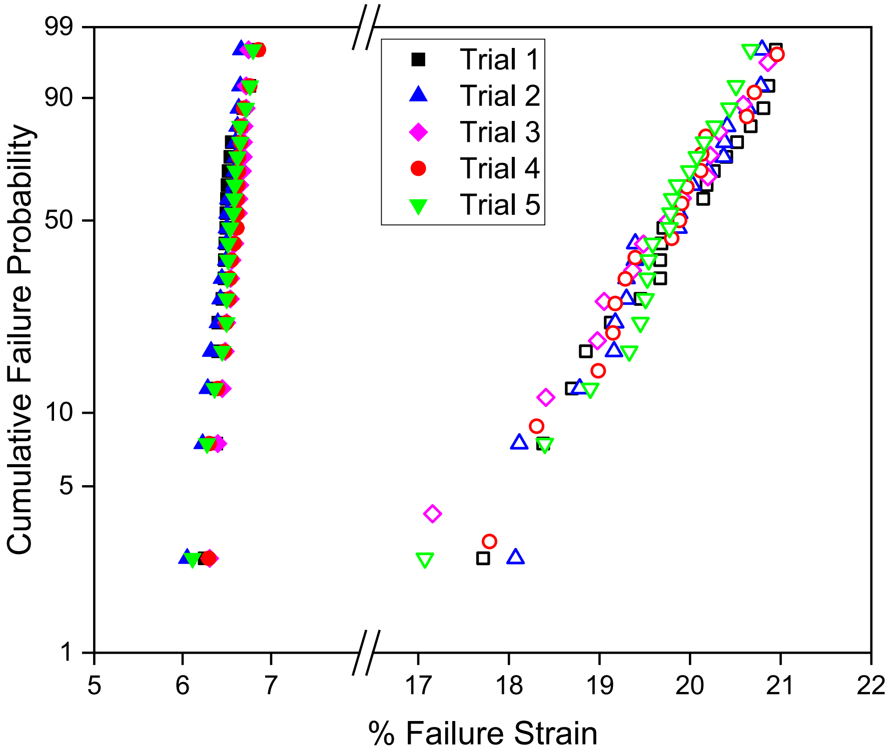

Figure 3.1. Failure strains of five independently drawn sets of OI-A glass, measured at a 4000μm/sec faceplate velocity in either room temperature air at 40%RH (closed symbols) or in liquid nitrogen (open symbols).

Figure 3.2 shows the failure strains for the five trials of OI-B container glass. Similar to OI-A, with a 95% confidence, there is not a significant difference between the mean failure strains of the five trials tested in either liquid nitrogen or 40%RH/25°C air. The fibers tested in ambient conditions have a greater Weibull modulus (50.6 – 79.4) than those tested in liquid nitrogen (33.6 - 57.7). Table 3.1 summarizes the average failure strain and Weibull modulus for each trial of pristine OI-A and OI-B fibers.

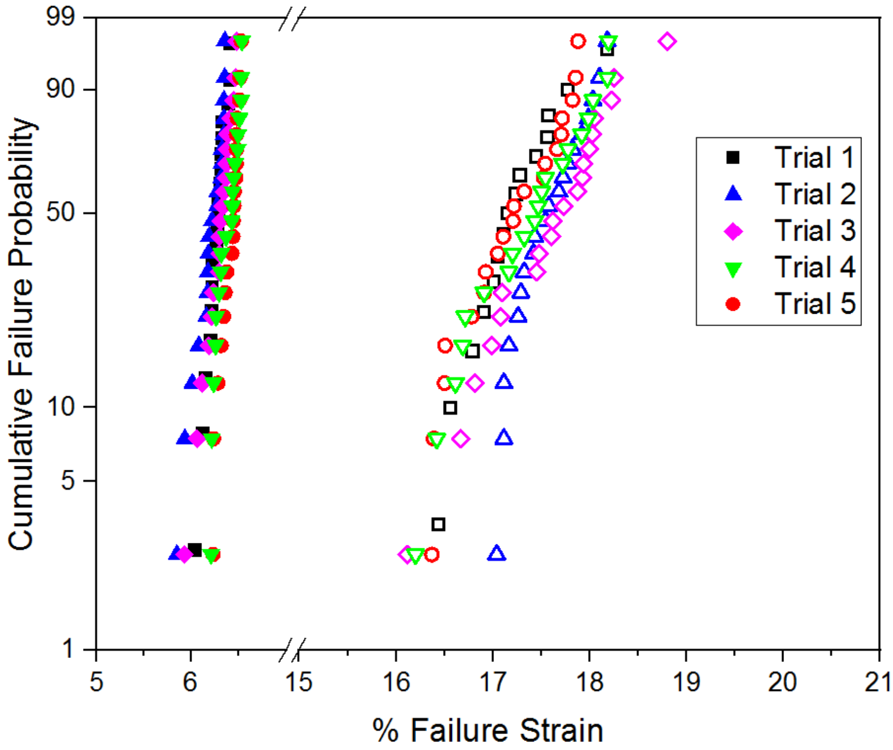

Figure 3.2. Failure strains of five independently drawn sets of OI-B glass, measured at a 4000μm/sec faceplate velocity in either room temperature air at 40%RH (closed symbols) or in liquid nitrogen (open symbols).

The OI-A fibers consistently had failure strains that were 3% greater than the OI-B fibers (Figure 3.3) when tested in 40%RH/25°C air, and ~13% greater failure strains when tested in liquid nitrogen (Figure 3.4). The failure strains of both OI-A and OI-B fibers tested in 40%RH/25°C air are similar to those collected under similar conditions for a commercial soda lime silicate by Tang et. al.[42], and to those collected by Lower

[43] on fibers drawn from a laboratory melt with the nominal composition15.5 Na_2O-9.4 CaO-75.1 SiO_2 (mol%) (Table 3.1).

Table 3.1. Average failure strains for commercial and laboratory SLS glass tested with the TPB in similar condition[42], [43].

Source	Testing Conditions	Average Failure Strain	Weibull Modulus
Commercial SLS[42]	LN_2: 4000μm/sec	16.35±0.14	43.9
Laboratory SLS (15.5-9.4-75.1 mole%)[43]	LN_2: 4000μm/sec	19.03±0.10	287
Laboratory SLS (10.4-9.4-80.2 mole%)[43]	LN_2: 4000μm/sec	16.73±0.11	179
OI-A Commercial SLS Trial 1	LN_2: 4000μm/sec	19.78±0.88	24.7
OI-A Commercial SLS Trial 2	LN_2: 4000μm/sec	19.69±0.80	29.7
OI-A Commercial SLS Trial 3	LN_2: 4000μm/sec	19.56±1.00	24.4
OI-A Commercial SLS Trial 4	LN_2: 4000μm/sec	19.67±0.83	28.5
OI-A Commercial SLS Trial 5	LN_2: 4000μm/sec	19.63±0.81	28.0
OI- B Commercial SLS Trial 1	LN_2: 4000μm/sec	17.20±0.46	44.8
OI- B Commercial SLS Trial 2	LN_2: 4000μm/sec	17.59±0.64	57.7
OI- B Commercial SLS Trial 3	LN_2: 4000μm/sec	17.20±0.51	33.6
OI- B Commercial SLS Trial 4	LN_2: 4000μm/sec	17.35±0.60	37.4
OI- B Commercial SLS Trial 5	LN_2: 4000μm/sec	17.58±0.36	35.1
Commercial SLS[42]	42%RH: 4000μm/sec	6.42±0.12	66.6
OI-A Commercial SLS Trial 1	40%RH: 4000μm/sec	6.51±0.14	54.7
OI-A Commercial SLS Trial 2	40%RH: 4000μm/sec	6.48±0.16	49.3
OI-A Commercial SLS Trial 3	40%RH: 4000μm/sec	6.59±0.12	68.6
OI-A Commercial SLS Trial 4	40%RH: 4000μm/sec	6.58±0.14	57.6
OI-A Commercial SLS Trial 5	40%RH: 4000μm/sec	6.54±0.16	49.6
OI- B Commercial SLS Trial 1	40%RH: 4000μm/sec	6.27±0.10	79.4
OI- B Commercial SLS Trial 2	40%RH: 4000μm/sec	6.21±0.15	50.6
OI- B Commercial SLS Trial 3	40%RH: 4000μm/sec	6.30±0.14	54.6
OI- B Commercial SLS Trial 4	40%RH: 4000μm/sec	6.39±0.12	65.4
OI- B Commercial SLS Trial 5	40%RH: 4000μm/sec	6.42±0.10	83.8

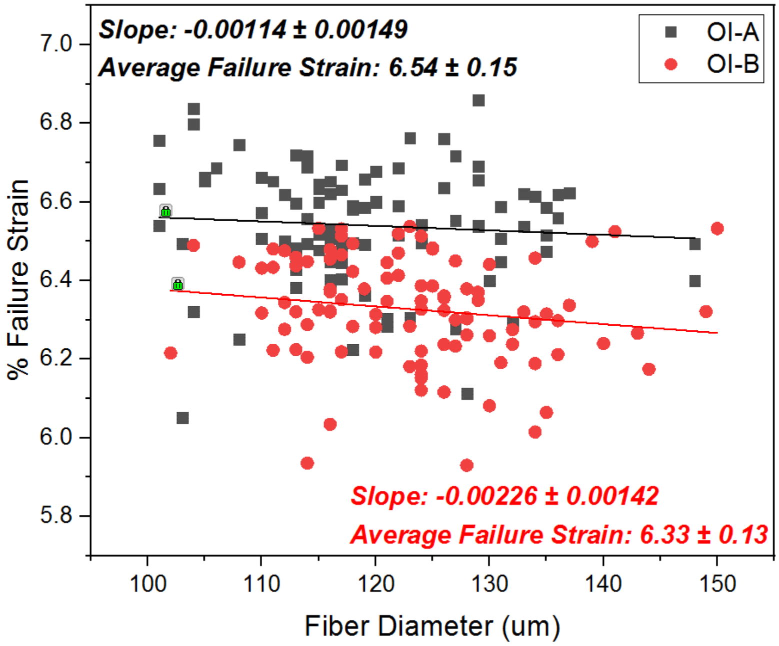

Figure 3.3. Fiber failure strains dependence on fiber diameter for OI-B and OI-A glass tested room temperature air at in 40%RH.

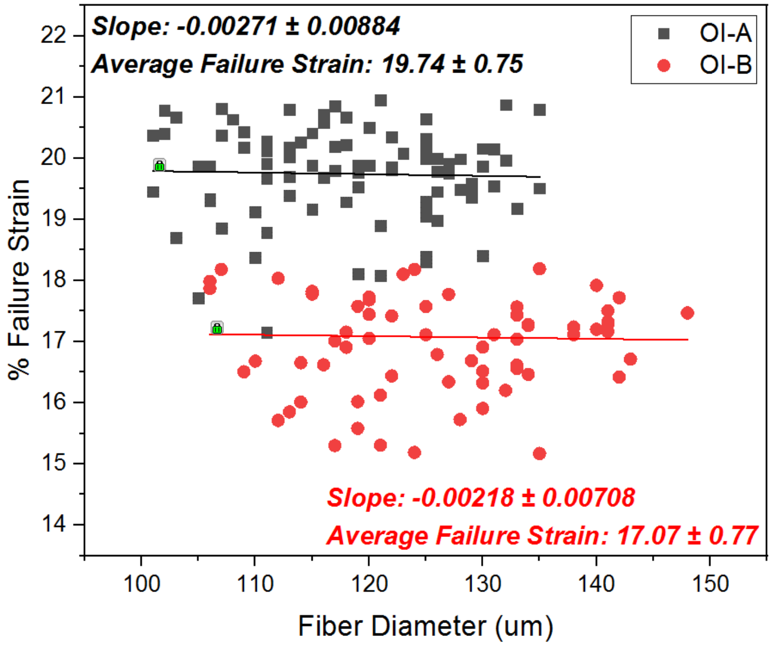

Figure 3.4. Fiber failure strains dependence on fiber diameter for OI-B and OI-A glass tested in room temperature air at 40%RH.

The dependence of fiber failure strains on fiber diameter, measured for both glasses in room temperature air at 40%RH and in liquid nitrogen, are also shown in Figure 3.3 and Figure 3.4, respectively. Regression analyses, the results of which are given in each figure, indicate slight negative correlations of failure strain with fiber diameter.

3.2.2. Fatigue Parameter of Pristine Fibers. The Weibull distribution of failure strains for pristine OI-A and OI-B fibers tested in room temperature air with different levels of relative humidity are shown in Figure 3.5 and Figure 3.6, respectively. As seen in previous studies, the failure strains increase with decreasing relative humidity[42]. Figure 3.7 and Figure 3.8 show the effects of faceplate velocity on the failure strains of pristine OI-A and OI-B fibers, respectively, tested in air with 40% relative humidity. Here, failure strains increase with greater faceplate velocity.

Rondinella and Matthewson used the faceplate velocity dependence of failure strain to calculate the fatigue parameter, ‘n’, according to[98]:

$$n = 1 + \frac{1}{d\left(\frac{log\varepsilon_f}{logv_{fp}}\right)} \tag{3.1}$$

Figure 3.9 and Figure 3.10 show the logarithmic plots of faceplate velocity and average failure strain, tested at varied levels of humidity, for OI-A and OI-B fibers, respectively. The slopes of the fitted lines were used with Equation 3.1 to calculate values of ‘n’ for the different experimental conditions.

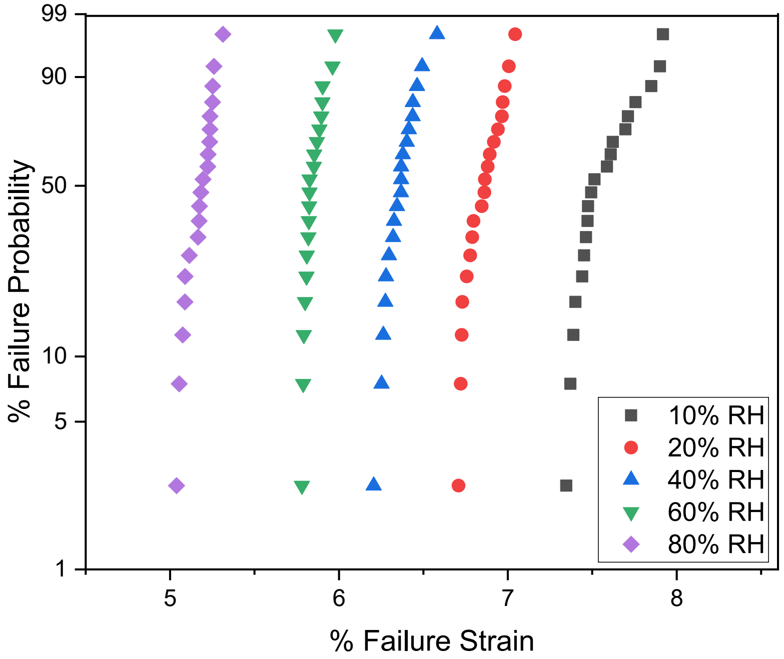

Figure 3.5. Weibull distributions of failure strains for OI-A fibers tested at 4000μm/sec in room temperature air with different levels of relative humidity.

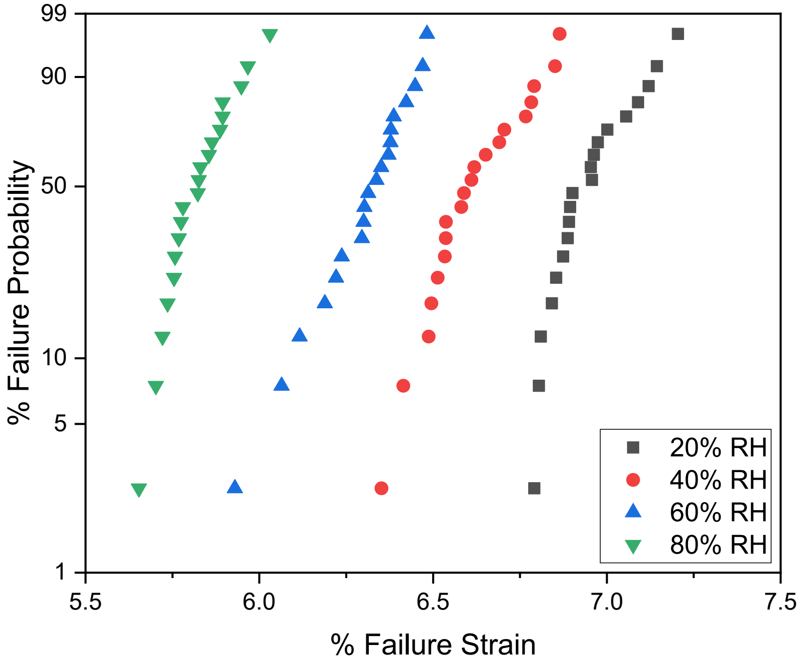

Figure 3.6. Weibull distributions of failure strains for OI-B fibers tested at 4000μm/sec in room temperature air with different levels of relative humidity.

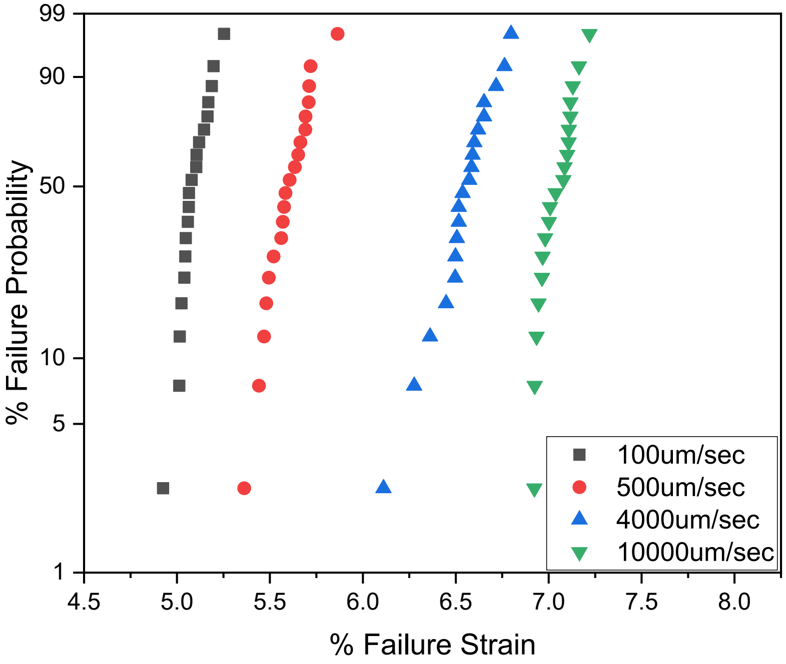

Figure 3.7. Weibull distributions of failure strains for OI-A fibers tested in room temperature air, 40%RH at various faceplate velocities.

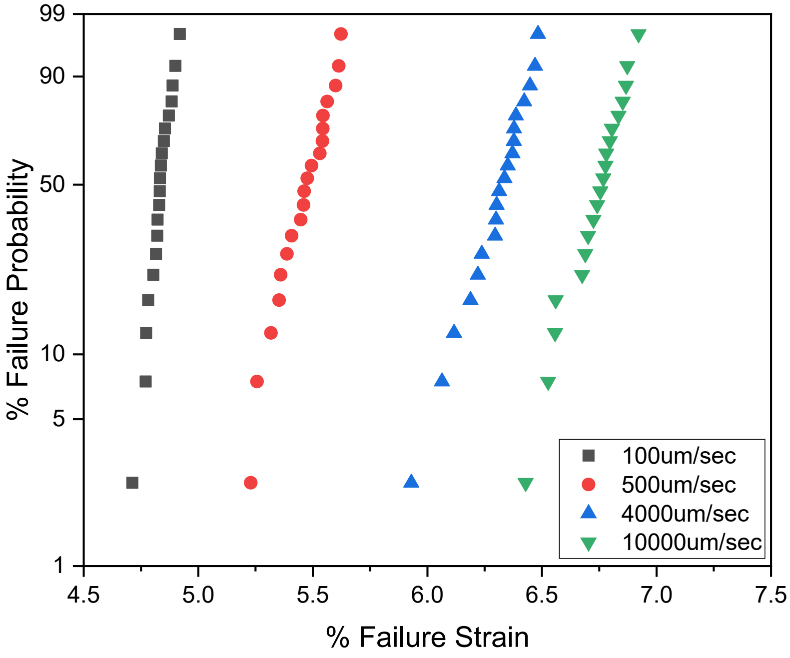

Figure 3.8. Weibull distributions of failure strains for OI-B fibers tested in room temperature air, 40%RH at various faceplate velocities.

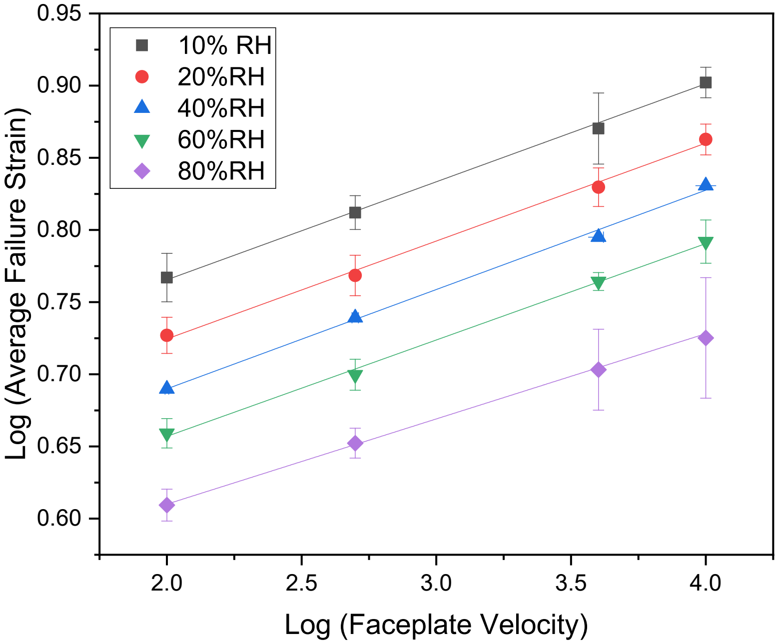

Figure 3.9. Average failure strains of pristine OI-A glass fibers measured as a function of faceplate velocity in room temperature air with different values of relative humidity.

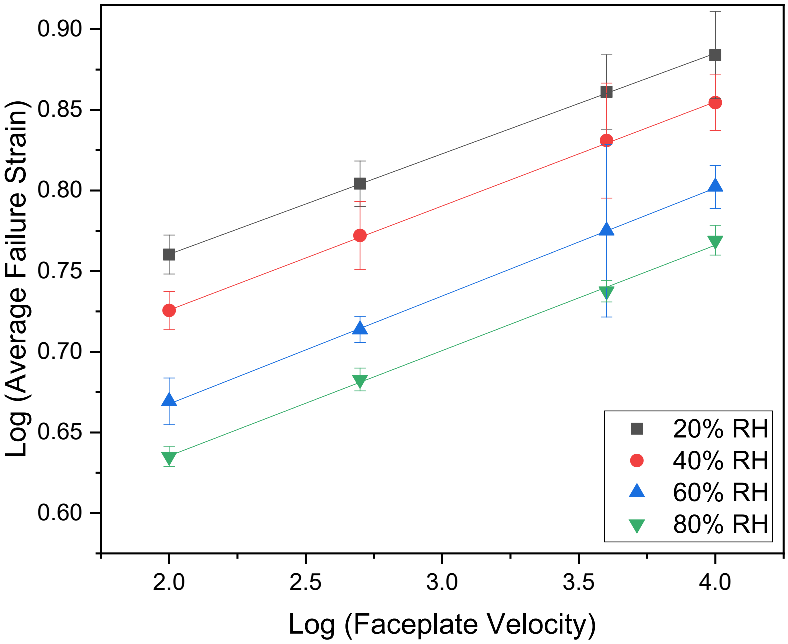

Figure 3.10. Average failure strains of pristine OI-B glass fibers measured as a function of faceplate velocity in room temperature air with different values of relative humidity.

Figure 3.11 shows the values of the fatigue parameter measured at different levels of humidity for OI-A and OI-B fibers. The 95% confidence and prediction bands are shown in dark grey and light grey, respectively. The linear fit of the data shows a slope of -0.00399±0.00624. The fatigue parameter values are similar for OI-A and OI-B at 60 and 80% RH but are lower for OI-A at 20 and 40% RH. Table 3.2 compares the fatigue parameter values measured in this study with those determined for soda-lime silicate glasses by a variety of techniques and reported in the literature,

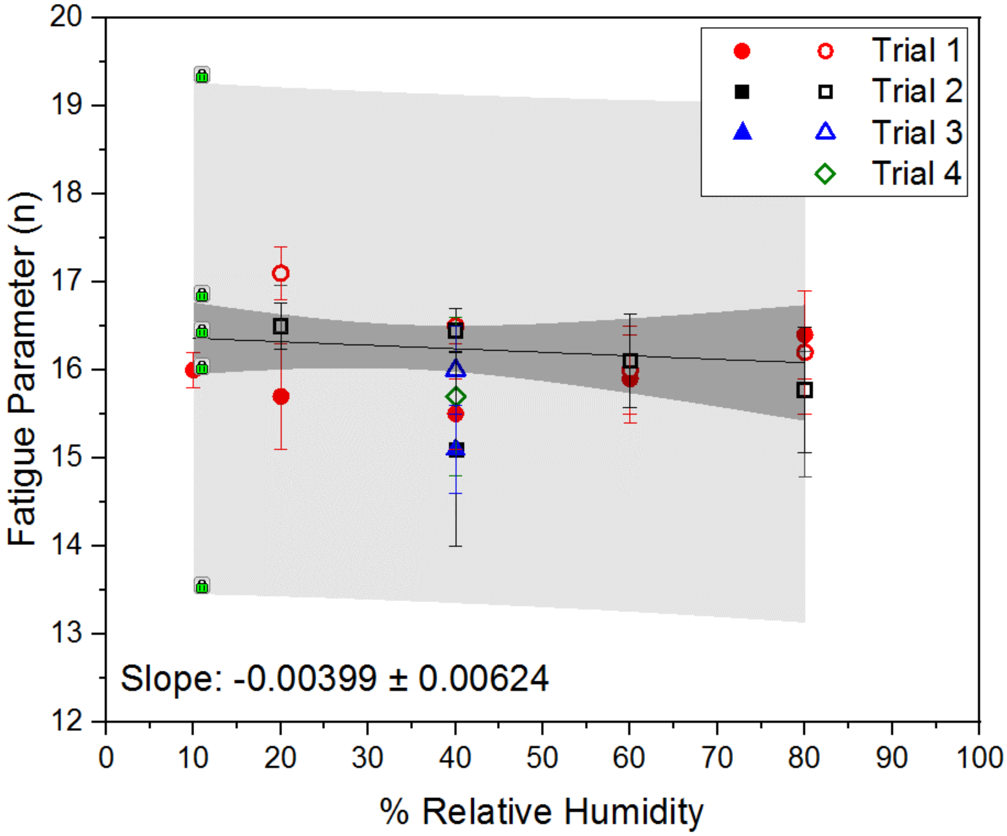

Figure 3.11. Fatigue parameters of OI-A (closed symbols) and OI-B (open symbols) glass over a range of humidity. 95% confidence and prediction band are shown in dark and light grey, respectively. The line shows the linear fit of all the data.

Table 3.2. Fatigue parameter values for soda-lime silicate glass from this study and fatigue parameters values reported in the literature that were determined by other testing methods. All measurements were taken at room temperature (RT).

Sample Form	Testing Method	Testing Environment	Fatigue Parameter	Ref
Fiber	Two Point Bend	10-80%RH	16.3 ± 2.9	Current Study
Fiber	Two Point Bend	0.7-92%RH	16.5 ± 4.1	[42]
Plate	Slow Crack Growth	RT Water	16.1 ± 3.1	[113]
Strips	Four Point Bend	RT Water	15.5 ± 3.4	[114]
Plate	Symmetric Bending	RT Water	13.6 ± 3	[88]
Abraded Rod	Slow Crack Growth	RT Water	16.9	[35]
Rod	Four Point Bend	100%RH	16	[51]
Strips	Four Point Bend	RT Water	14.7	[88]
Abraded Rod	Three Point Bend	RT Water	15.5	[88]
Abraded Rod	Three Point Bend	RT Water	16.8	[88]
Abraded Rod	Three Point Bend	RT Water	16.2	[88]
Bars	Indentation	Air	16.1	[115]
Bars	Indentation	RT Water	18.9	[115]
Plate	Slow Crack Growth	0.017-100%RH and RT Water	~20	[54]
Plate	Slow Crack Growth	0.002%RH and RT Water	~16.4	[58]

3.2.3. Failure and Fatigue of Fibers with Different Residual Water Contents.

FTIR spectroscopy was used to determine the water content of the glasses processed under ambient, dry, and wet conditions. The ambient processed glass is OI-B Trial 5, discussed previously, and the wet- and dry-processed samples were also from OI-B, prepared at a similar time as OI-B Trial 5. Figure 3.12 shows the FTIR spectra for the three glasses processed in the different conditions. There are clear peaks at 2800cm^{-1} and 3500 cm^{-1} which are attributed to strongly and weakly bonded –OH, respectively[116]. The magnitude of the peaks increases for glasses processed with increasing water activity.

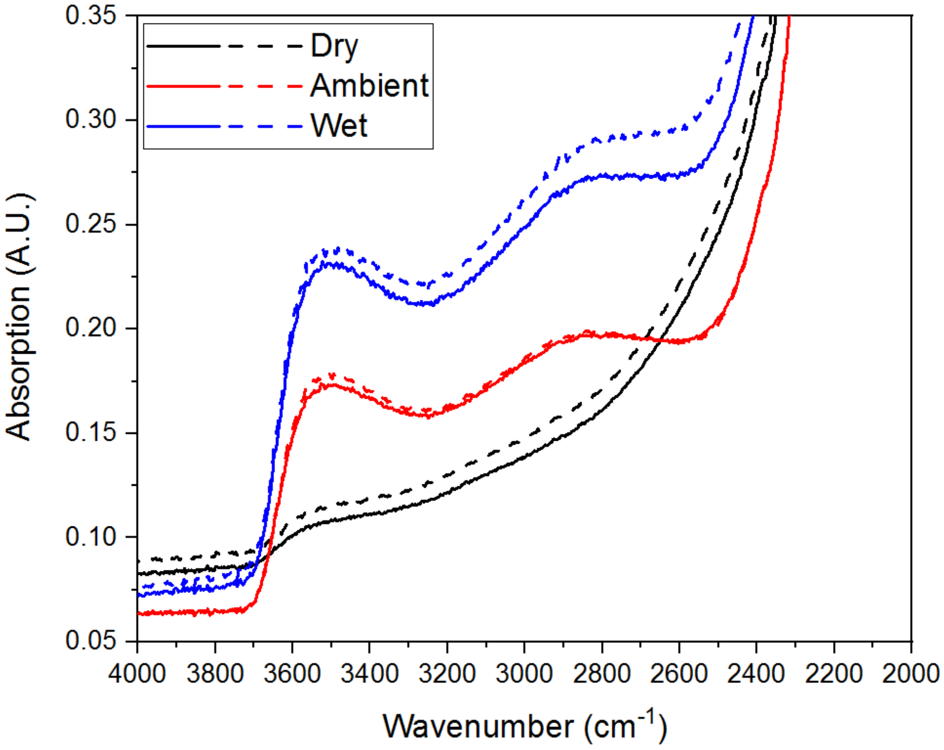

Figure 3.12. FTIR spectra of OI-B glasses processed under dry, ambient, and wet conditions. Solid lines indicate the spectra from the first sample while dashed lines indicate spectra from the second sample.

The intensity of the absorption peak at 2800cm^{-1} was used to determine the water concentration, following the procedure described by Stuke, et al. [117]. The water content of the glasses was calculated using the Beer-Lambert Law:

$$C_i = \frac{A_{2800}}{\rho \cdot t \cdot \varepsilon_{2800}} \tag{3.2}$$

where ρ is the glass density, t the sample thickness, and A_{2800} and ε_{2800} are the absorbance and extinction coefficient at the 2800cm^{-1} band, respectively. The density was assumed to be consistent at 2.50x10^{-3}kg/m^3 among the glasses based on prior work showing that the density of SLS glass is unaffected by water contents up to 500ppm [118], [119]. The value used for ε_{2800} was 50.8 $\mathrm{L} \cdot \mathrm{mol}^{-1} \cdot \mathrm{cm}^{-1}$ [117]. The water contents were then determined to be 140±7 ppm-wt, 180±1 ppm-wt, and 270±14 ppm-wt for the dry, ambient and wet processed glasses, respectively. These glasses will be referred to as 140ppm, 180ppm, and 270ppm, respectively.

Figure 3.13 shows the Weibull distributions of failure strains for the pristine fibers drawn from 140ppm, 180ppm, and 270ppm melts. At a 95% confidence level, the mean of the inert failure strain measured in liquid nitrogen of the 270ppm fibers is significantly lower than those for the 140ppm and 180ppm fibers, whereas the means of the inert failure strains for the 140ppm and 180ppm fibers, are not significantly different from each other. The failure strains from testing in 40%RH conditions appear to have the reverse dependence on water content. With a 95% confidence level, the failure distributions are all significantly different, and the 270ppm glass has the highest failure strain in ambient conditions and 140ppm and 180ppm fibers have lower failure strains. Table 3.3. shows the fatigue parameters measured for all three glasses in 40%RH, room temperature air; each of these values falls within the 15.5 – 16.5 range typical for pristine OI-B fibers (Figure 3.11).

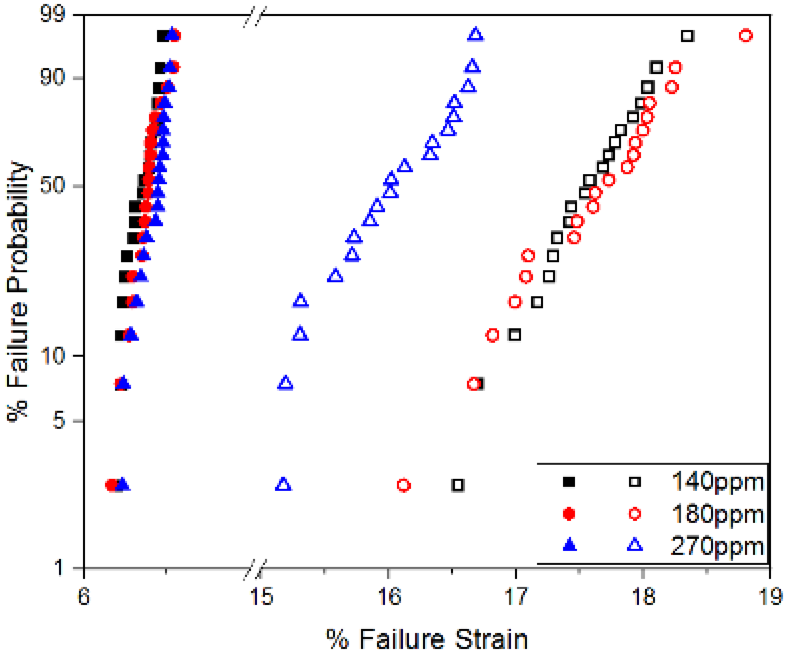

Figure 3.13. Weibull distributions of failure strains for pristine fibers with varying water content. Open symbols are fibers tested in liquid nitrogen and closed symbols represent fibers tested in 40%RH, room temperature air.

Table 3.3. Fatigue parameters determined in 40%RH, room temperature air for OI-B glasses with different residual water contents.

Water Content	**Fatigue Parameter**
140 ppm	16.0 ± 0.6
180 ppm	15.5 ± 0.9
270 ppm	15.6 ± 0.4

3.3. DISCUSSION

3.3.1. Intrinsic Strength of SLS. For the commercial soda-lime silicate glasses in this study, the average failure strains of pristine OI-A and OI-B glass fibers, measured in room temperature air at 40% RH and in liquid nitrogen compare well with previous two-point bend studies of similar glasses[43], [44] (Table 3.1), although OI-A had a 13%

greater inert failure strain than OI-B. It has been argued that the high failure strains and low standard deviations for fibers tested in inert conditions using the two point bend method are representative of the intrinsic strength of different glasses[66], [102]. To estimate the failure stress (σ_f) of the fibers from the failure strain (ε_f), Hooke's law can be used where E is the first order elastic modulus:

$$\sigma = E \times \varepsilon \tag{3.3}$$

However, for strains above about 2%, the elastic modulus is non-linear, but can be estimated by [120]:

$$E = E_o + E_1\varepsilon + \frac{1}{2}E_2\varepsilon^2 \tag{3.4}$$

where E_0, E_1, and E_2 are the second, third, and fourth order elastic moduli, respectively. The stress-strain relationship can then be described as:

$$\sigma = E_o\varepsilon + \frac{1}{2}E_1\varepsilon^2 + \frac{1}{6}E_2\varepsilon^3 \tag{3.5}$$

Cavaill determined the second- and third-order elastic moduli for a soda-lime-silicate glass using Brillouin scattering[121]. However, it is difficult to measure the fourth-order modulus. Gupta and Kurkjian [99] were able to estimate the fourth-order elastic modulus by assuming, for a flawless material, the intrinsic failure stress (σ^*) is at a maximum compared to the intrinsic failure strain (ε^*). Therefore:

$$E(\varepsilon^{*}) = E_{o} + E_{1}\varepsilon + \frac{1}{2}E_{2}\varepsilon^{2} = 0 \tag{3.6}$$

Solving for the fourth order elastic constant, *E_2*, in Equation 3.6 and subbing it into Equation 3.5 gives:

$$\sigma = E_{0}\varepsilon + \frac{1}{2}E_{1} - \left(\frac{\varepsilon^{3}}{3}\right)\left(\frac{E_{0}+E_{1}\varepsilon^{*}}{(\varepsilon^{*})^{2}}\right) \tag{3.7}$$

Table 3.4 summarizes the results from using the Kurkjian-Gupta method[99] to convert the failure strains to failure stress, and compares these failure strengths to those reported in the literature. OI-B and OI-A failure strengths in ambient conditions compare well to those reported by Tang[41]. In inert conditions, OI-B failure strengths are similar to literature values, whereas the OI-A failure strengths are somewhat greater. The variance in inert strength between OI-A and OI-B indicates that there may be some compositional or structural differences between the two glasses.

Table 3.4. Failure Strength Data for SLS glass fibers tested in ambient or inert environments from this study and reported in the literature.

Glass	**Testing Condition**	**Estimated Failure Strength**	**Reference**
OI-A FIBERS	Liquid Nitrogen	10.2±0.2GPa	Present Study
OI-B FIBERS	Liquid Nitrogen	8.9±0.2GPa	Present Study
SLS FIBERS	Liquid Nitrogen	8.4±0.1GPa	[41]
SLS FIBERS	Liquid Nitrogen	7.4±0.6GPa	[122]
SLS FIBERS	Liquid Nitrogen	7.5 GPa	[86]
OI-A FIBERS	40%RH/RT	4.7±0.1GPa	Present Study
OI-B FIBERS	40%RH/RT	4.5±0.1GPa	Present Study
SLS FIBERS	40%RH/RT	4.0±0.1GPa	[42]
SLS FIBERS	25^{o}C Air	3.4±0.4GPa	[122]

A Weibull modulus from a strength study of a brittle material is usually between 5 and 10, and a Weibull modulus above 25 is considered to be high[123]. The Weibull moduli for the failure strains of the OI-B and OI-A fibers are consistently greater than 25 when measured in both ambient and inert testing conditions, and are similar to values determined from two-point bending study of other remelted commercial SLS glass[42], Table 3.1. Two-point bend studies of laboratory batched and melted silicate glasses have yielded Weibull moduli greater than 100[43]. These differences may reflect a greater degree of structural homogeneity for the simpler, laboratory processed glasses. In modified silicate glasses, different modifiers have different interatomic spacing and bond angles within the glass network[124]. Molecular dynamic studies have shown that alkali-rich regions form on the nano-scale in modified glasses [125], [126]. The inherent inhomogeneity of interatomic spacing and distribution of alkali-rich regions could contribute to the broader failure strain distribution observed in commercially produced glasses compared to compositionally simpler laboratory prepared glasses.

The Weibull modulus for failure strains of fibers tested in inert conditions is lower than the Weibull modulus of fibers tested in ambient conditions (Table 3.1). Tang observed a similar trend in a two-point bend study of commercial soda-lime silicate fibers tested in ambient and inert conditions, for melts processed at 1120°C for up to 16 hours [44]. The presence of water in ambient conditions could nucleate and grow new flaws during the test, rather than only propagating pre-existing flaws. In inert conditions, the source of failure is likely at pre-existing flaws, which may or may not be present near the highest stressed area at the tip of the u-shaped fiber. Therefore, the failure strains of the fibers will be higher when the pre-existing flaw is farther from the tip. However, in ambient conditions the critical flaw might be from the nucleation and growth of a new flaw at the tip of the u-shape where strained bonds are being attacked by water. In this case, the distribution of pre-existing flaws has less influence on the distribution of failure strains.

Alternatively, the narrowing of the distribution of failure strains could be related to the relative effect of pre-existing flaws compared to the effect of fatigue. The distribution of inert failure strains represents the variation in intrinsic flaw size. If the effect of fatigue is significantly greater than the effect of the size of the intrinsic flaws, then the failure strains at room temperature are more representative of the effect of fatigue, rather than the effect of flaw size. Because the failure distributions are narrower in ambient conditions, it is likely that to some extent sufficiently small flaw sizes do not affect the rate of fatigue reactions.

There is a small, negative correlation between the failure strain and fiber diameter (Figures 3.3 and 3.4). Lower [42] noted a similar, but smaller negative correlation (-0.00013/μm) for the failure strains of E-glass fibers. The negative correlations in this study have a large standard deviation so it is possible that they are insignificant. However, these correlations might reflect a probability that a larger critical flaw will be activated when a larger fiber is tested, similar to the sample size dependence of the strengths of brittle materials[112]. A second possibility is that some residual stress is retained in the larger fibers and this residual stress reduces failure strain (strength) in the larger fibers. Residual stresses in the fibers could possibly occur from “tempering” of the fiber during rapid cooling. The residual stress in tempered glass can be calculated using[127]:

$$\sigma = \frac{E \cdot \alpha}{1-\mu} \cdot \frac{\rho \cdot c_p}{\lambda} \cdot h \cdot d^2 \cdot b \tag{3.2}$$

where σ is the residual stress; E is the elastic modulus; α is the coefficient of thermal expansion (CTE); μ is Poisson's ratio; ρ is the density; c_p is the specific heat; λ is the thermal conductivity; h is the cooling rate; d is the characteristic dimension (in this case the radius of the fiber); and b is the shape factor of the glass. In the case of tempering, the residual stresses will be compressive. From equation 3.2, a thicker fiber would have a larger residual compressive stress than a thinner fiber, and therefore, should have a higher failure strain compared to thinner fibers. This is the opposite of the trend observed in Figures 3.3 and 3.4 so it is unlikely that tempering stress is present in the fibers.

The dynamic fatigue parameters for OI-A and OI-B glass fibers at room temperature appear to agree well with each other and appear to be independent of humidity, at least above 40%RH RH (Figure 3.11). The fatigue parameter at values of relative humidity between 10-40% is less consistent between OI-B and OI-A; OI-B has a consistently greater fatigue parameter at lower values of humidity than OI-A indicating a lower susceptibility to fatigue compared OI-A glass.

Wiederhorn [40], Tang et. al. [51], and Krohn et. al. [110] all found that the fatigue parameter for SLS remained unchanged over a wide range of humidity and in room temperature water. However, there is plenty of evidence that the fatigue parameters of silica and of E-glass are dependent on humidity (Figure 1.10)[42]. Studies of the fatigue process for SLS show that it depends on an exchange of the Na^+ ions in the glass with H_3O^+ ions at the tip of a critical flaw (Equation 1.3)[46], [72]. In contrast, the fatigue mechanism of cross-linked glasses like E-glass and silica is primarily through the hydrolysis of Si-O-Si bonds[69]. Tang et. al. argued that the fatigue parameter for SLS is independent in atmospheres with humidity values above 1%RH. They attributed the independence of the fatigue parameter to the faster kinetics of ion-exchange reactions compared to the hydrolysis reactions that account for fatigue in silica and E-glass [42].

The average fatigue parameter for the SLS glass over the 10-80% RH range of testing environments in the present study agrees very well with values obtained by several other methods on different sample geometries (Table 3.2). With the exception of Wiederhorn's fatigue parameters derived from a slow crack growth method[54], all values in Table 3.2 fall within the predicted interval (~13-19) in Figure 3.11. Wiederhorn noted that for slow crack growth, crack propagation behavior dominates, whereas for pristine surfaces, crack initiation prior to crack propagation must be taken into account[54]. This difference results in an increase in fatigue parameter for slow crack growth studies due to a limiting factor like diffusion of water to the crack tip, slowing the effect of fatigue reactions. For glass surfaces exposed to the ambient, there is not a similar barrier that potentially limits the influence of water.

3.3.2. Effect of Residual Water Content on Pristine Glass Failure and Fatigue.

Water is dissolved into the glass structure as either OH- species or water molecules. Figure 3.14 shows the concentration of OH and water molecules as a function of cumulative water content in soda lime silicate glass[69]. At water concentrations below 0.5wt% (5000ppm-wt), the water is almost entirely incorporated as OH species into the glass structure (Figure 3.14). Commercial container glasses typically have a water contents between 100ppm-wt and 300ppm-wt [128], which is consistent with the range of water contents, 140ppm-wt to 270ppm-wt, noted in this study, and this water is expected to be dominated by OH- species.

The pristine failure strains of the glass show some dependence on water content. The 180ppm and 140ppm fibers are similar, but the 270ppm fibers have a 9% lower failure strain when measured under liquid nitrogen (Figure 3.13). McMillan and Chlebik reported a 10% decrease in inert failure strengths for soda lime silicate glass with increasing OH content up to 400ppm-wt[129], but increasing fracture strength with water concentrations above 400ppm. Other studies on glasses with increasing water contents above 1wt% have consistently shown an increase in fracture strength [130], [131]. This has been attributed to the increased plasticity due to the increase in non-bridging oxygens (NBO) for higher water content glasses[131]. When the water is only dissolved as OH species, the NBOs formed are significantly different than the NBOs associated with alkali and alkaline earth ions. Hydroxyl species act as a terminal species in the glass network, whereas alkali and alkaline earth ions maintain an oxygen metal ion bridge ($O^- - M^+ - O^-$). This creates a complete break in the silicate network, which weakens the structure. Under stress, these weaker sites could become the critical flaws.

The susceptibility to fatigue for soda lime silicate glasses in ambient conditions has been shown to increase with increasing water contents above 79ppm[129], [130]. The increase in fatigue susceptibility was attributed to the decreased chemical durability of water-containing alkali and alkaline earth silicate glasses. Further studies of the fatigue susceptibility of sodium silicate glasses measured in inert environments also observed an increase in susceptibility to fatigue with increasing water content[130]. The increase in inert environment was attributed to the molecular water in the glass inducing fatigue reactions. All three glasses in the present study have similar fatigue parameters of 15.5-16 (Table 3.3). It is likely that any decrease in the fatigue parameter with increasing water content is obscured by the margin of error in this study.

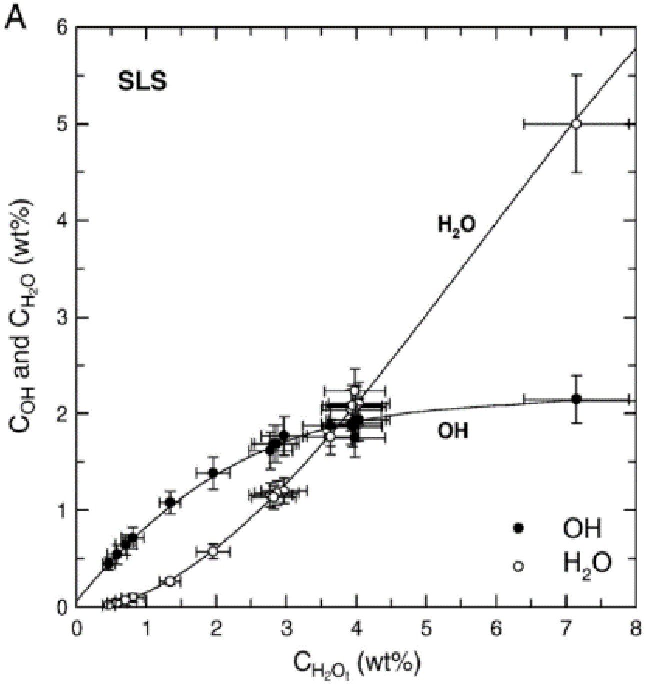

Figure 3.14. Concentrations of OH groups and H_2O molecules in commercial soda lime silicate glass as a function of total water content for SLS [69].

4. EFFECT OF WEATHERING AND CORROSION ON FATIGUE AND FAILURE OF SODA LIME SILICATE GLASS

4.1. OVERVIEW

In this section, the effects of weathering and corrosion on the failure, fatigue, and surface characteristics of soda lime silicate glasses with different water contents is examined. SLS fibers were exposed to 10-80%RH air at 50°C, ambient laboratory air, and immersed in 50°C water for up to for up to 95 days. The susceptibility to fatigue was evaluated over the exposure period for these different conditions. The changes in the fiber surfaces were also characterized using analytical Scanning Electron Microscopy (SEM), Raman Spectroscopy, and Atomic Force Microscopy (AFM). The effects of weathering on the failure strain and fatigue susceptibility of glasses with different residual water contents was also determined.

4.2. RESULTS

4.2.1. Failure Strains. The Weibull distributions of failure strains for OI-A and OI-B fibers exposed to 80%RH/50°C air and tested in room temperature air (40%RH, 4000μm/s faceplate velocity) are shown in Figure 4.1 and Figure 4.2, respectively. For OI-A, the failure strain distributions initially broaden with weathering time, although after 14 days of weathering, the distributions begin to narrow again. The failure strain distributions of OI-B fibers remain relatively narrow throughout the entire period of weathering. Similar trends in the failure strain distributions of weathered fibers tested in liquid nitrogen were also noted for the OI-A fibers (Figure 4.3) and the OI-B fibers (Figure 4.4). These failure strains were also collected at 4000μm/s faceplate velocity.

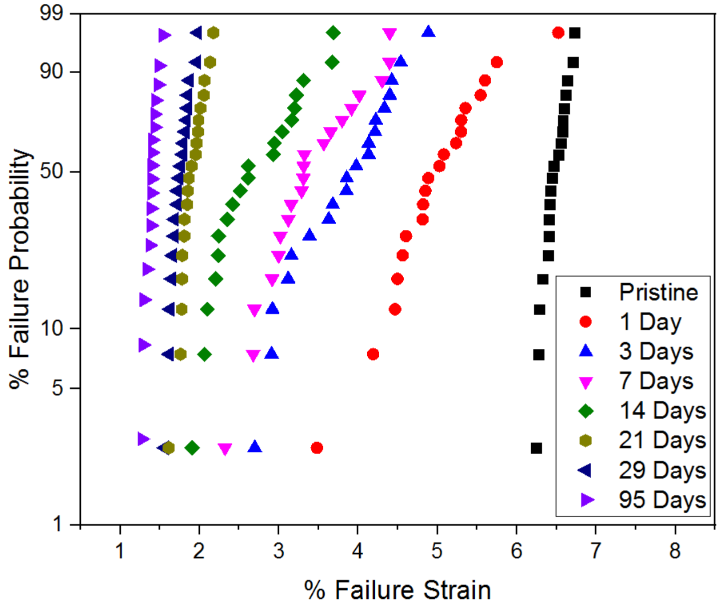

Figure 4.1. Failure strain distributions of OI-A fibers weathered in 80%RH/50°C air for up to 95 days and tested in 40%RH, room temperature air.

Figure 4.5 and Figure 4.6 show the average failure strains for OI-A and three trials of OI-B fibers weathered in 80RH/50°C conditions, measured in room temperature air (40% RH) and in liquid nitrogen, respectively. The average failure strains for both testing conditions decrease over the entire weathering period of 95 days for OI-A fibers and 28 days for OI-B fibers. The failure strains for both glasses initially decrease rapidly to approximately 30% of the initial failure strain over the first 21 days of weathering, then continue to decrease more slowly after that.

Average failure strains of OI-B fibers measured in room temperature, 40%RH air and in liquid nitrogen after being aged in 50°C water are compared to those weathered in 80%RH/50°C air in Figure 4.7. Failure strains decreased for fibers aged in water for the first three days, then leveled off after that, whereas failure strains continued to decrease for samples weathered in 80%RH/50°C air. Figure 4.8 shows the Weibull modulus for the failure strain distributions in Figure 4.7. The fibers tested in ambient conditions have a greater Weibull modulus (52.3 – 62.0) than those tested in liquid nitrogen (21.0 – 47.2). However, there does not appear to be a notable difference between the Weibull modulus of fibers aged in 50°C water and fibers weathered in 80%RH/ 50°C conditions.

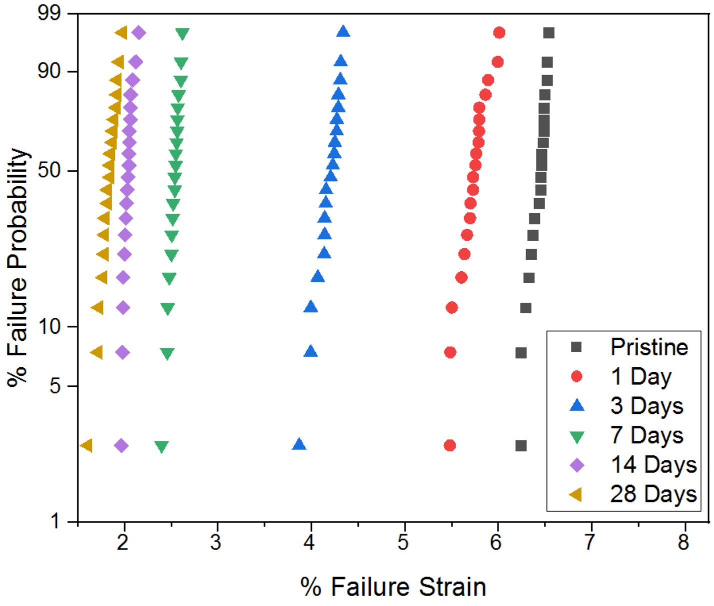

Figure 4.2. Failure strain distributions of OI-B fibers weathered in 80%RH/50°C air for up to 95 days and tested in 40%RH, room temperature air.

Fibers with different water contents were weathered in 80%RH/50°C air, and those failure strain data are shown Figure 4.9 and Figure 4.10, for measurements made in room temperature, 40%RH air and in liquid nitrogen, respectively. After 28 days of weathering in 80%RH/50ºC, the failure strain (ε) is only 20-25% of the pristine failure strain (ε_p), for both testing conditions. There was a greater decrease in failure strain for weathered 270ppm glass, particularly when measured in ambient conditions; viz., Figure 4.8.

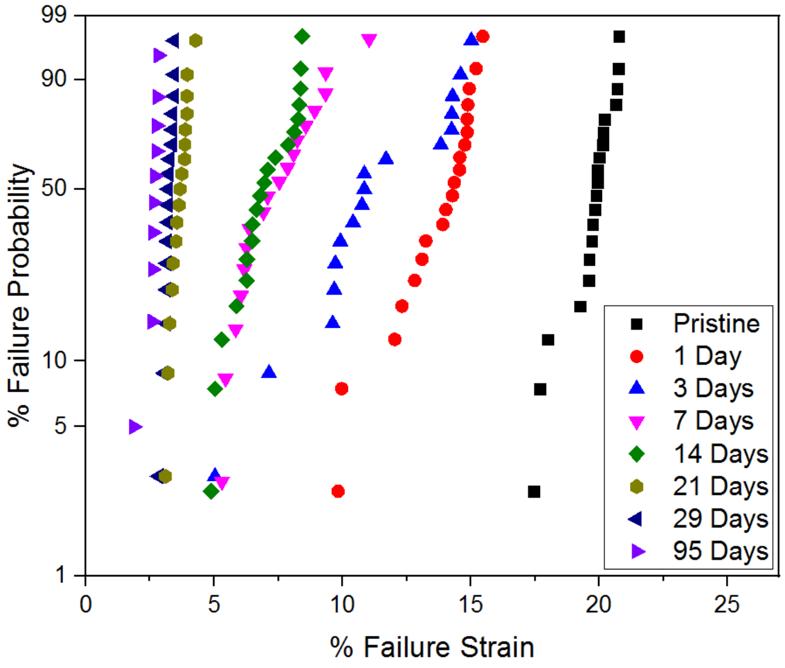

Figure 4.3. Failure strain distributions of OI-A fibers weathered in 80%RH/50°C air for up to 95 days and tested in liquid nitrogen.

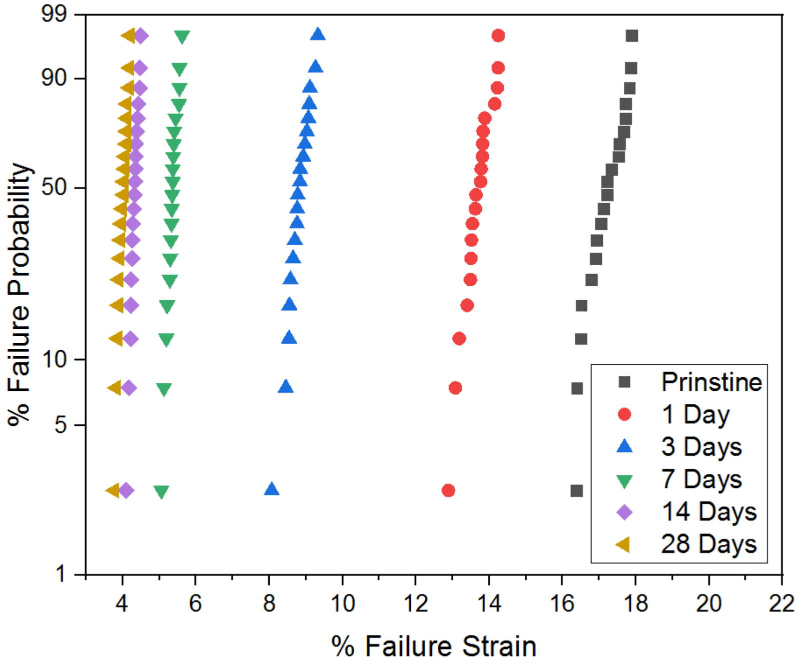

Figure 4.4. Failure strain distributions of OI-B fibers weathered in 80%RH/50°C air for up to 95 days and tested in liquid nitrogen.

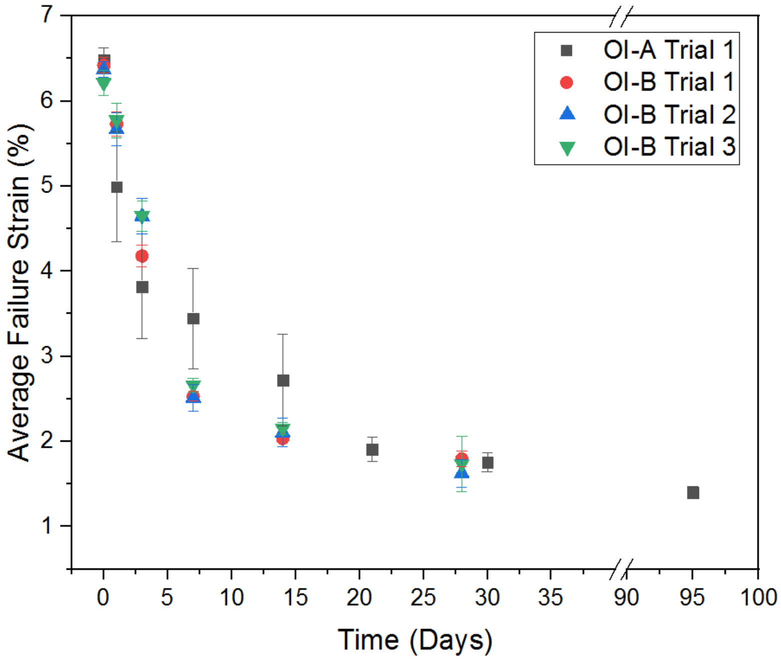

Figure 4.5. Average failure strains of OI-A and OI-B fibers weathered in 80%RH/50°C air and tested in 40%RH, room temperature air.

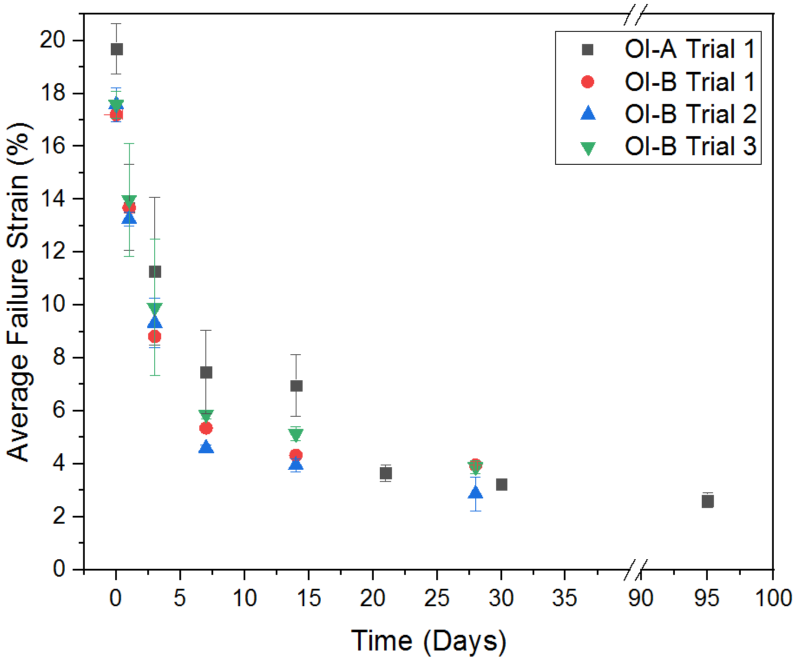

Figure 4.6. Average failure strains of OI-A and OI-B fibers weathered in 80%RH/50°C air and tested in liquid nitrogen.

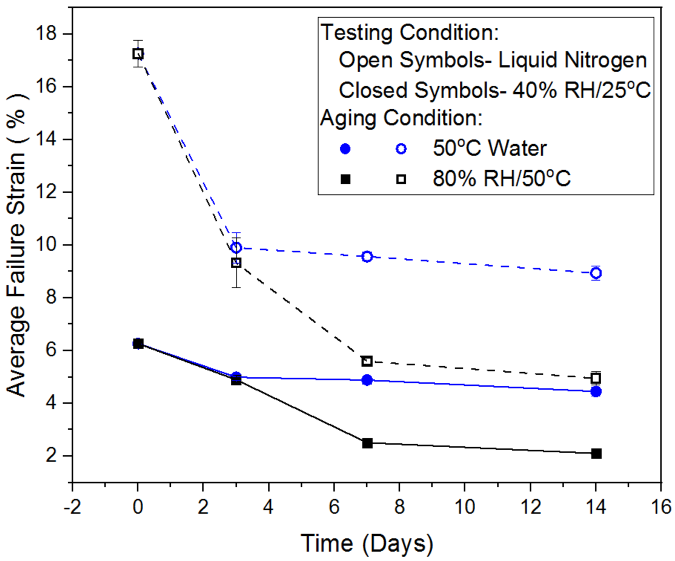

Figure 4.7. Average failure strains, measured at room temperature in air (40% RH) (closed symbols) and under liquid nitrogen (open symbols), for OI-B fibers aged in either 50°C water or 50°C/80%RH air. Lines are guides for the eyes.

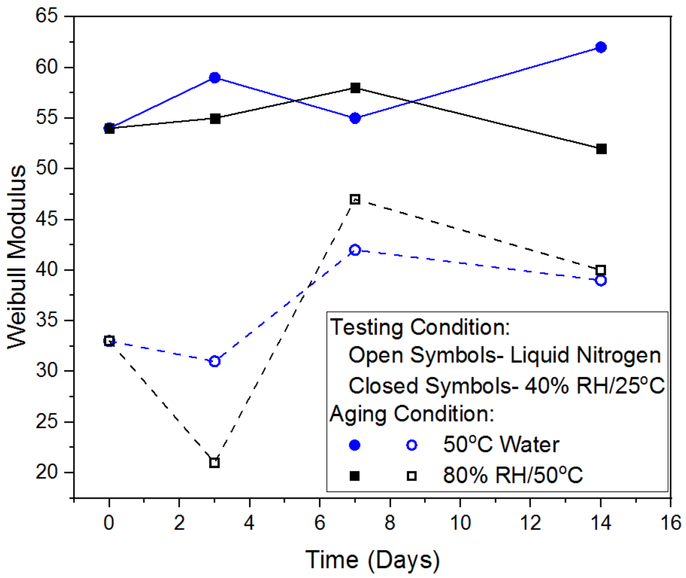

Figure 4.8. Weibull modulus for failure strain distributions, measured at room temperature in air (40% RH) (closed symbols) and under liquid nitrogen (open symbols), for OI-B fibers aged in either 50°C water or 50°C/80%RH air. Lines are guides for the eyes.

Figure 4.11 and Figure 4.12 summarize the time-dependent failure strains normalized to the pristine failure strain and measured in room temperature, 40%RH air and in liquid nitrogen, respectively, for fibers weathered in lower humidity conditions. The failure strains of both OI-A and OI-B fibers initially increase when the fibers are exposed to 10%RH/50°C air, and then after about three days, failure strains decrease, but to a much smaller degree than what happens in 80%RH/50°C air (Figure 4.5). Fibers weathered under ambient conditions and in 40%RH/50°C air show similar initial increases in failure strain. The scatter in the liquid nitrogen data (Figure 4.11) is greater than in the 40%RH air data (Figure 4.10), but the former also show some increases in failure strains for fibers aged 3-5 days, then little fall-off in failure strain for fibers weathered for longer times, in contrast to the significant loss in failure strain for fibers weathered in 80%RH/50°C air (Figure 4.6).

Figure 4.13 and Figure 4.14 show similar weathering time-dependences for the normalized failure strains for fibers with different residual water contents exposed to 10%RH/50°C air, tested in room temperature, 40%RH air and in liquid nitrogen, respectively. All three glasses with different residual water contents appear to follow the same weathering trends. When tested in air, failure strains increase by about 5% over the first 3-7 days of exposure, then gradually fall to about 93% of the pristine values after 28 days exposure (Figure 4.12). When tested in liquid nitrogen, failure strains increase by 10-15% over the first week of exposure, with little loss over 28 days (Figure 4.13). In contrast, when these fibers are exposed to 80%RH/50°C air, failure strains decrease to 20% of their original values after two weeks of exposure (Figure 4.9).

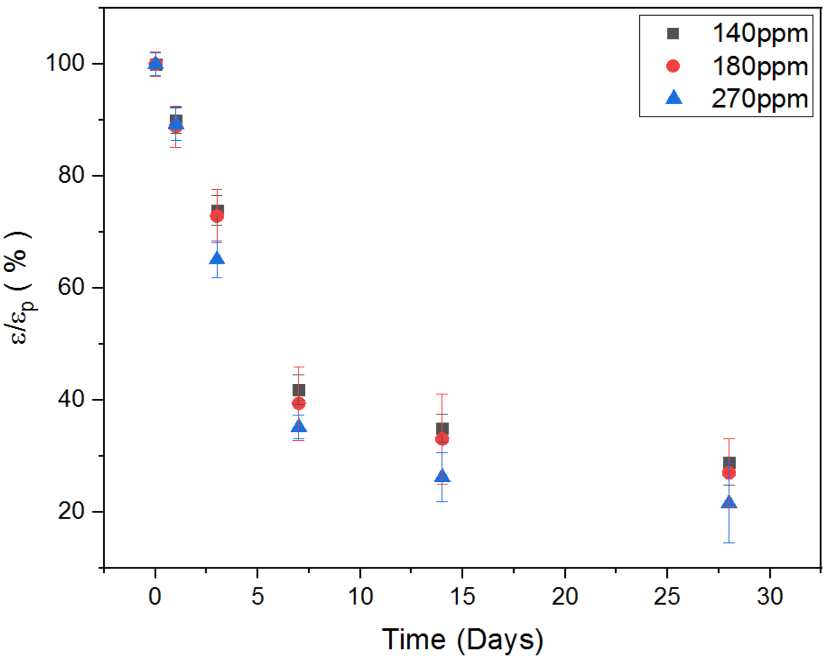

Figure 4.9. Normalized failure strains of OI-B fibers with different residual water contents tested in room temperature, 40%RH air at 4000μm/sec after weathering in 80%RH/50°C air.

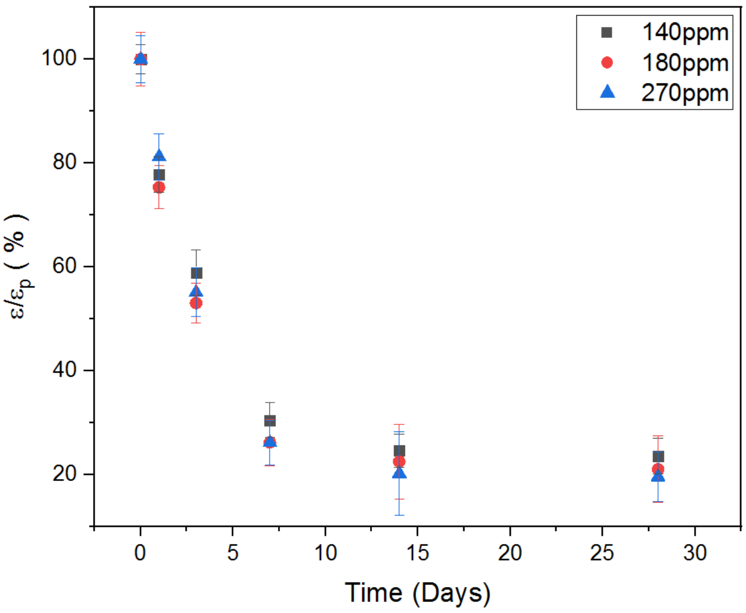

Figure 4.10. Normalized failure strains of OI-B fibers with different residual water contents tested in liquid nitrogen at 4000μm/sec after weathering in 80%RH/50°C air.

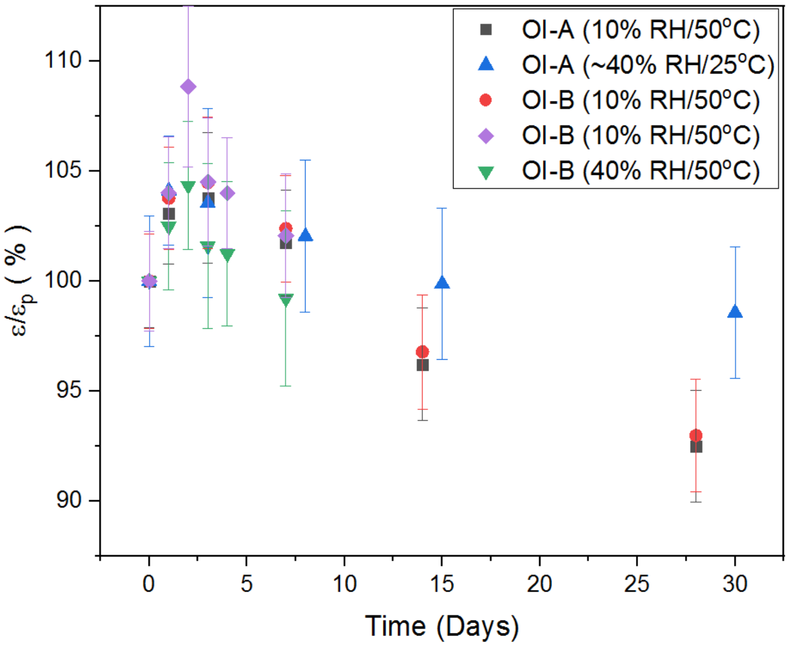

Figure 4.11. Normalized failure strains of OI-A and OI-B fibers weathered in the conditions indicated and tested in room temperature, 40%RH air at 4000µm/sec.

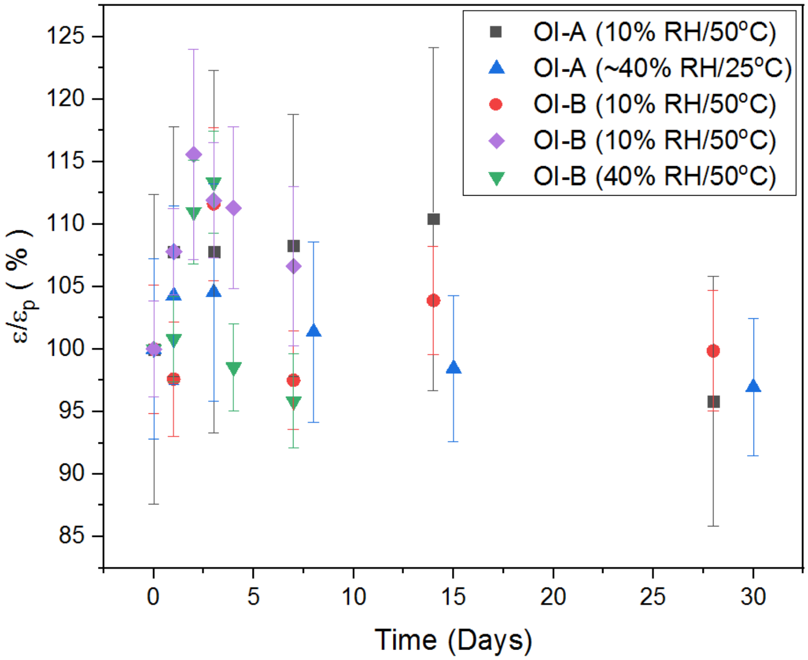

Figure 4.12. Normalized failure strains of OI-A and OI-B fibers weathered in the conditions indicated and tested in liquid nitrogen at 4000µm/sec.

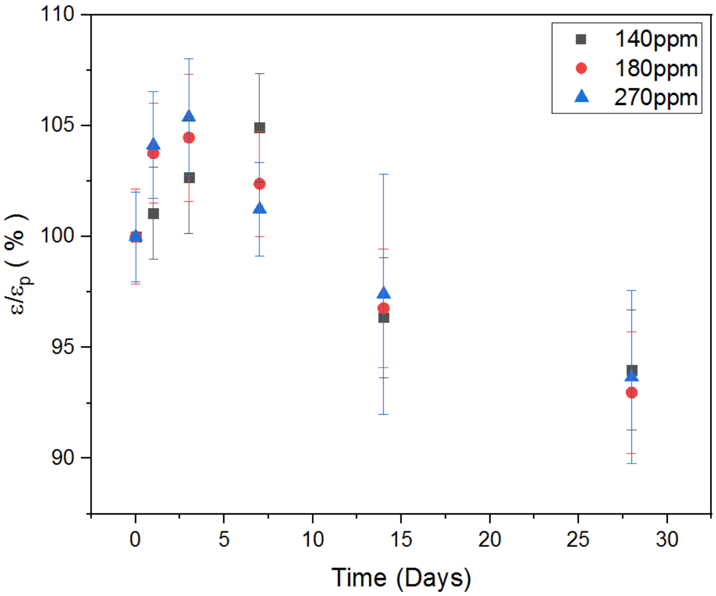

Figure 4.13. Normalized failure strains of OI-B fibers with different residual water contents after weathering in 10%RH/50°C air and tested in room temperature 40%RH air at 4000μm/sec .

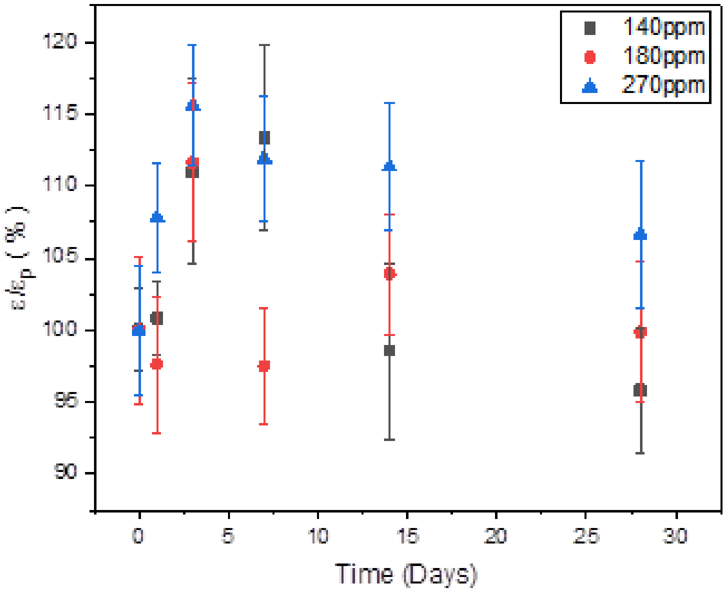

Figure 4.14. Normalized failure strains of OI-B fibers with different residual water contents after weathering in 10%RH/50°C air and tested in liquid nitrogen at 4000μm/sec.

4.2.2. Fatigue Susceptibility. The fatigue parameter for both OI-A and OI-B glass fibers weathered in 50°C/80%RH air increases with weathering time, from about 15 to about 22-25, as shown in Figure 4.15. For comparison, the fatigue parameters measured under similar conditions for E-glass are in the range 21-25 [42] and for fused silica fibers, fatigue parameters are 23-27 [64]. Thus, the sensitivity to fatigue of the weathered SLS fibers is less than it is for fresh SLS fibers, becoming more similar to those reported for more durable glasses. Figure 4.15 also shows that the fatigue parameters of fibers aged in 50°C water increased at the same rate as those of fibers weathered in 80%RH/50°C air over a similar time period.

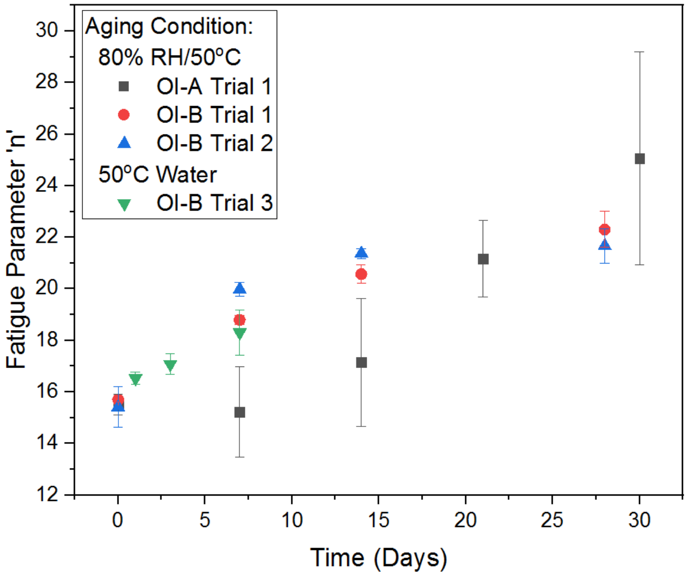

Figure 4.15. Fatigue parameters for OI-A and OI-B fibers measured in 40%RH, room temperature air. Fibers were weathered in either 50°C/80%RH air or aged in water at 50°C for up to 28 days.

Figure 4.16 shows the fatigue parameters of OI-B fibers held in 50°C water for 0, 3, or 7 days, and then tested in room temperature air at different levels of humidity, from

20%RH to 80%RH. The fatigue parameter appears to be independent of humidity for the pristine fibers and for fibers immersed in water for 3 days, although the latter were consistently greater. Fatigue parameters measured from fibers immersed in 50°C water for 7 days were significantly greater than those from the 0 and 3 day samples, particularly at 20%RH.

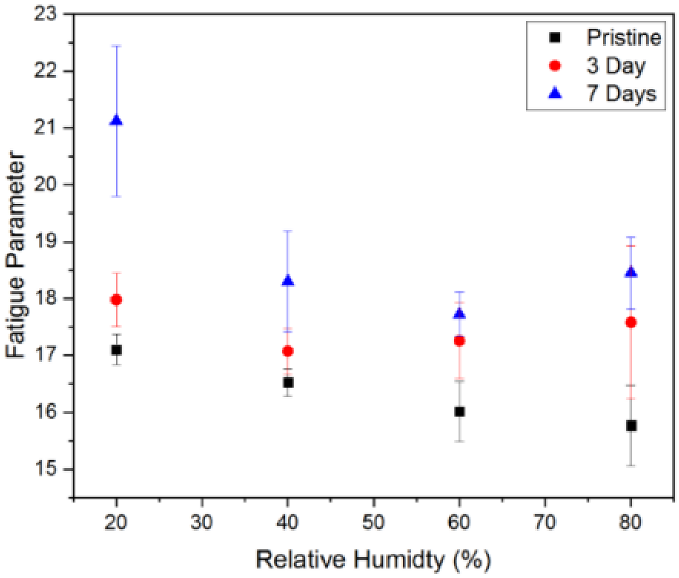

Figure 4.16. Fatigue parameters for OI-B fibers aged 50°C water for 0, 3, and 7 days, and tested in room temperature air at different levels of humidity.

For glasses with different water contents, the fatigue parameter of all fibers steadily increases from 15.5-16 to 21-23 after weathering in 80%RH/50°C air (Figure 4.16). The 270ppm water content glass has the greatest fatigue parameter, 23, after weathering for 28 days. In contrast, the fatigue parameters after weathering in 10%RH/50°C air for up to thirty days varied little from the values measured for the pristine glasses, remaining in the range 15-16.5 (Figure 4.16). As was the case for the

270ppm fibers weathered in 80%RH/50°C air, the 270ppm fibers weathered in 10%RH/50°C air had a greater fatigue parameter than the other two sets of fibers.

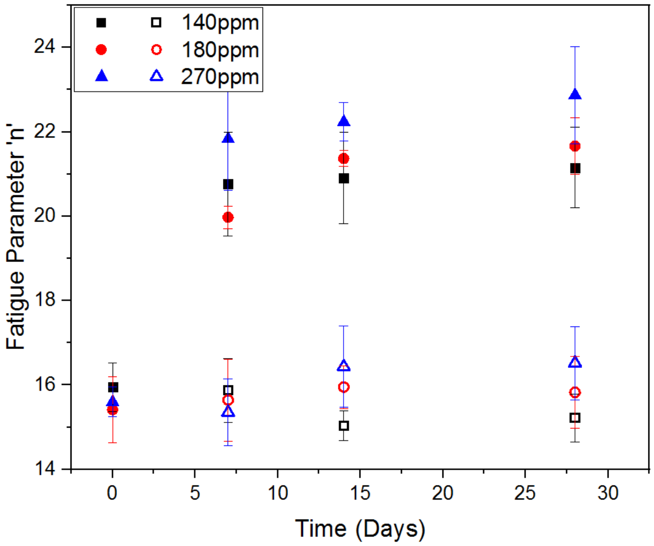

Figure 4.17. Fatigue parameters of OI-B fibers with different residual water contents, weathered in 10%RH/50°C air (open symbols) and in 80%RH/50°C air (closed symbols).

4.2.3. Surface Characterization. The surfaces of pristine and weathered fibers were examined by atomic force microscopy (AFM). Figure 4.18 shows the flattened images collected from OI-A fibers after three days exposure to 50°C/80%RH air. The root-mean square (RMS) surface roughness, R_q, of the pristine fiber is 1.0±0.5nm. After one day of weathering in 50°C/80%RH air, tiny dendritic features appear on the surface, increasing the surface roughness to 51±5nm. Also present on the surface after one day of weathering are surface features that were too large to be captured by the AFM. The AFM image from day three captures the edge of one of these features.

Scanning electron microscopy (SEM) images of OI-A glass surfaces weathered in 50°C/80%RH air for up to 30 days are shown in Figure 4.19. Corrosion features larger than those in the AFM images are apparent after one day of weathering. The surface features get progressively larger over time, evolving from micron-sized circular features (1-7 days) to more crystalline features that are tens of microns long (30 day). Similar features formed on the surfaces of weathered OI-B fibers (Figure 4.20).

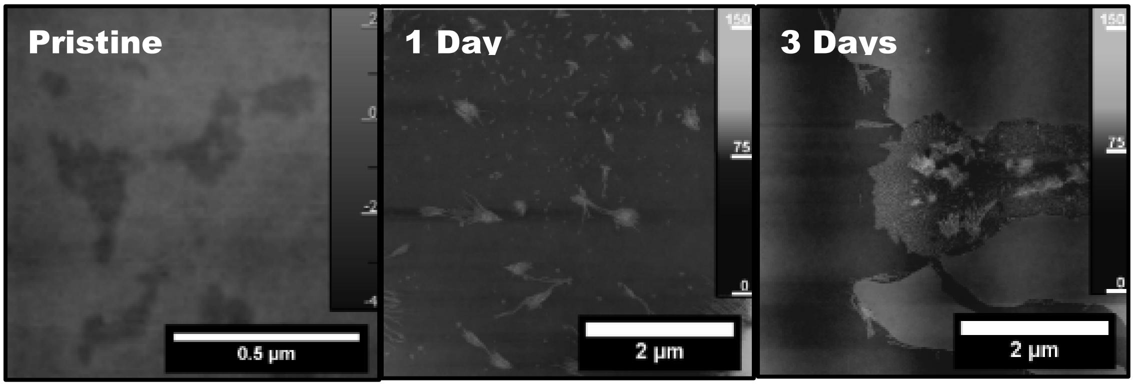

Figure 4.18. AFM images of a SLS surface weathered for up to 3 days in 80%RH/50°C air.

Figure 4.21 shows a comparison of fibers before and after rinsing with distilled water. Many of the surface features appear to have been removed with rinsing. However, there are still several features remaining. Fibers aged in 50°C water for 7 days show no visible surface features (Figure 4.22).

Figure 4.23 shows images collected from the surfaces of OI-A fibers after 100 days of weathering in 80%RH/50°C air. Large deposits are present, including those that extend several microns above the fiber surface (Figure 4.23B). Figure 4.23C shows surface features at higher magnifications. These features were rinsed off the surfaces in distilled water to reveal sub-micron etch pits (Figure 4.23D and E).

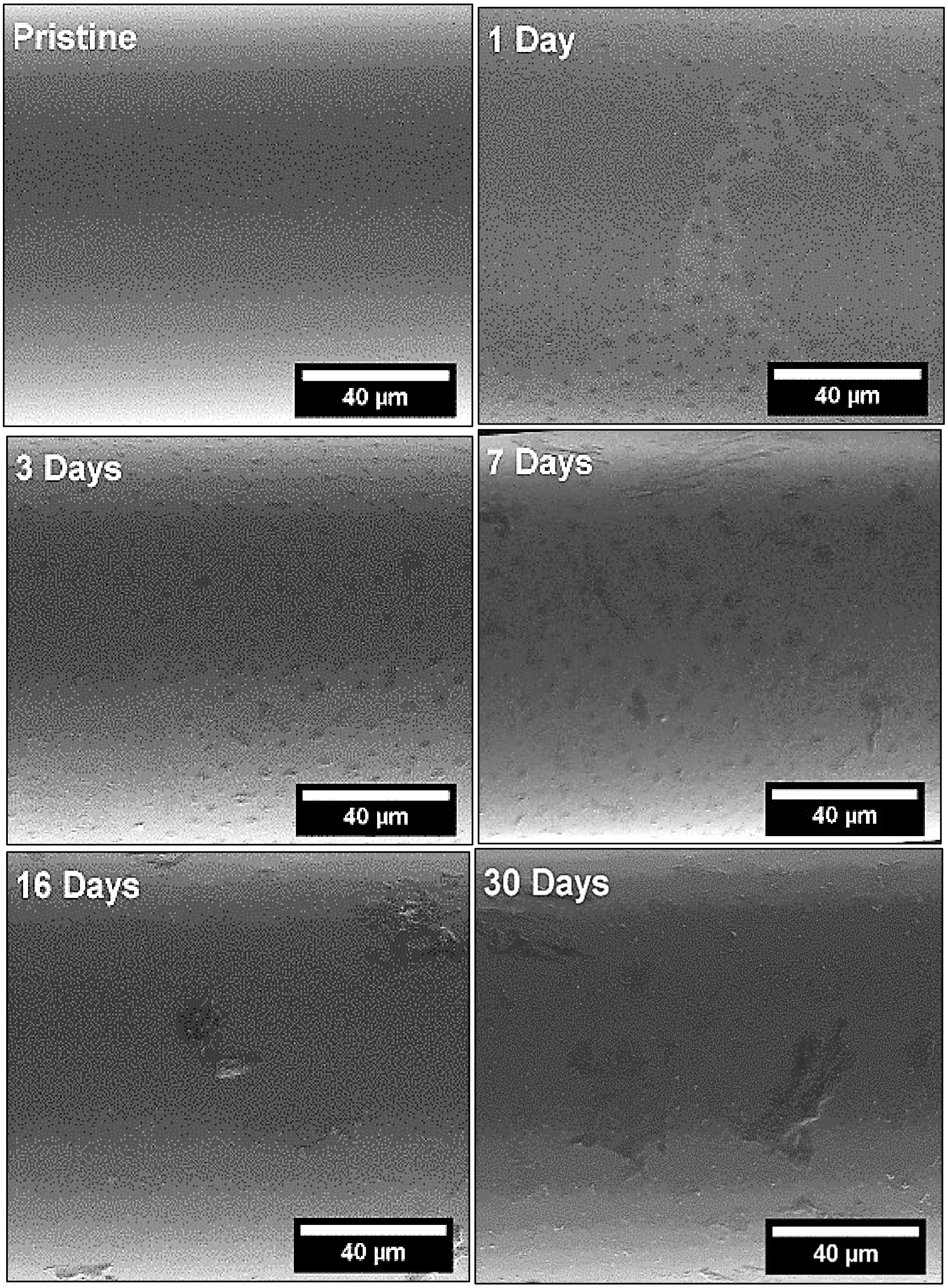

Figure 4.19. SEM images of OI-A fiber surfaces after weathering in 80%RH/50°C air for up to 30 days.

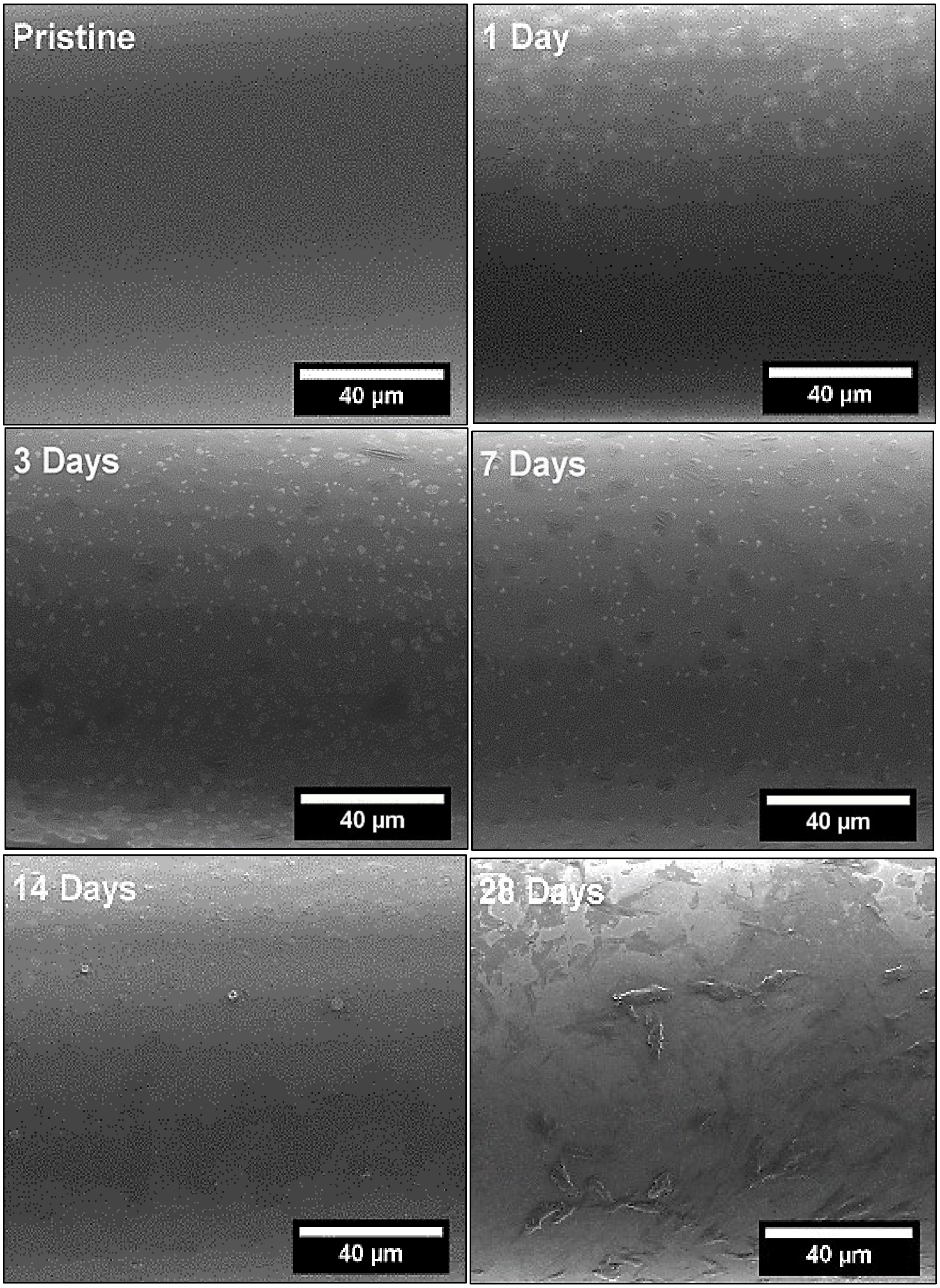

Figure 4.20. SEM images of OI-B fiber surfaces during weathering in 80%RH/50°C air for up to 28 days.

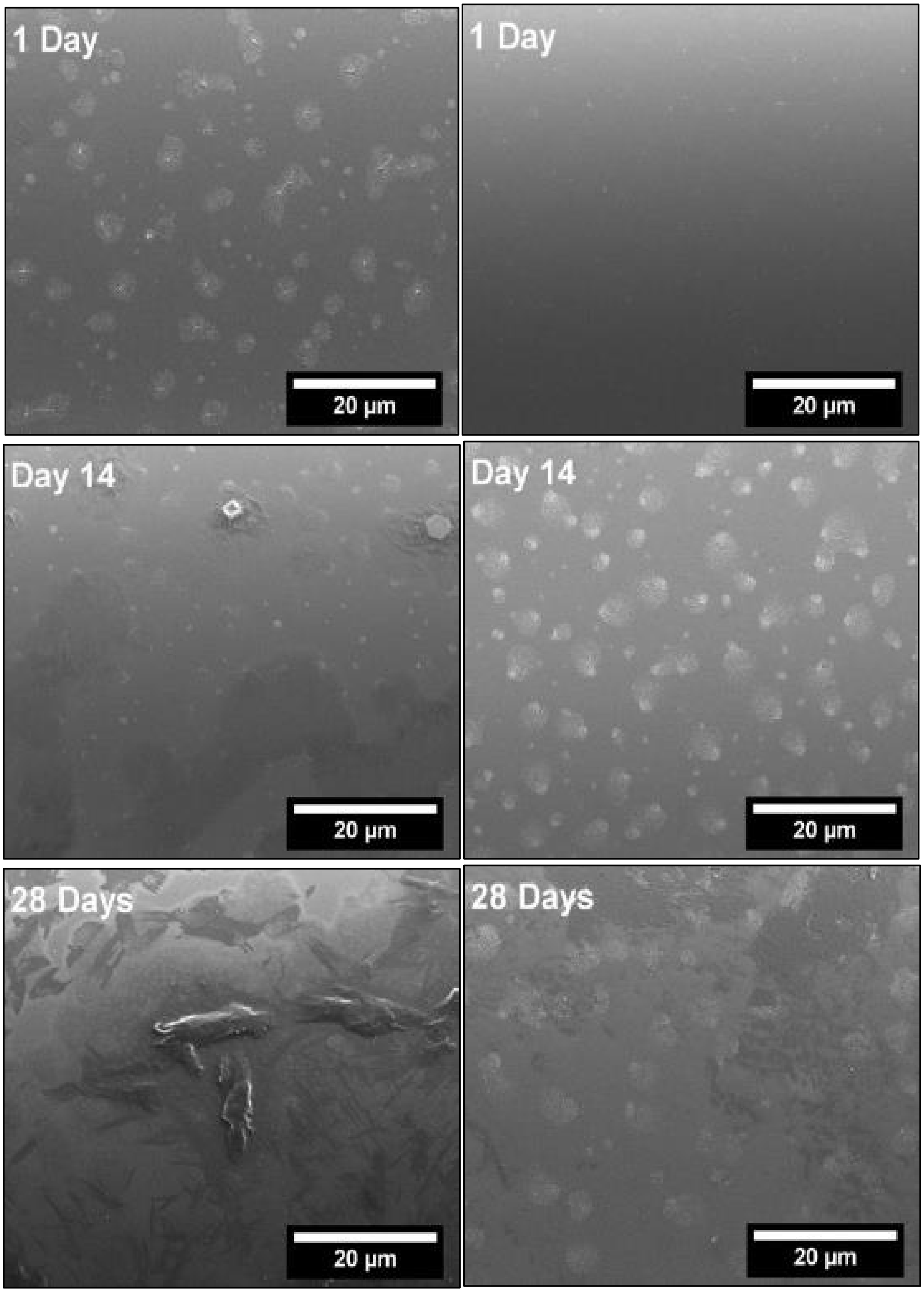

Figure 4.21. SEM images of OI-B fibers weathered in 80%RH/50°C air before rinsing (left side) and after rinsing (right side) in distilled water.

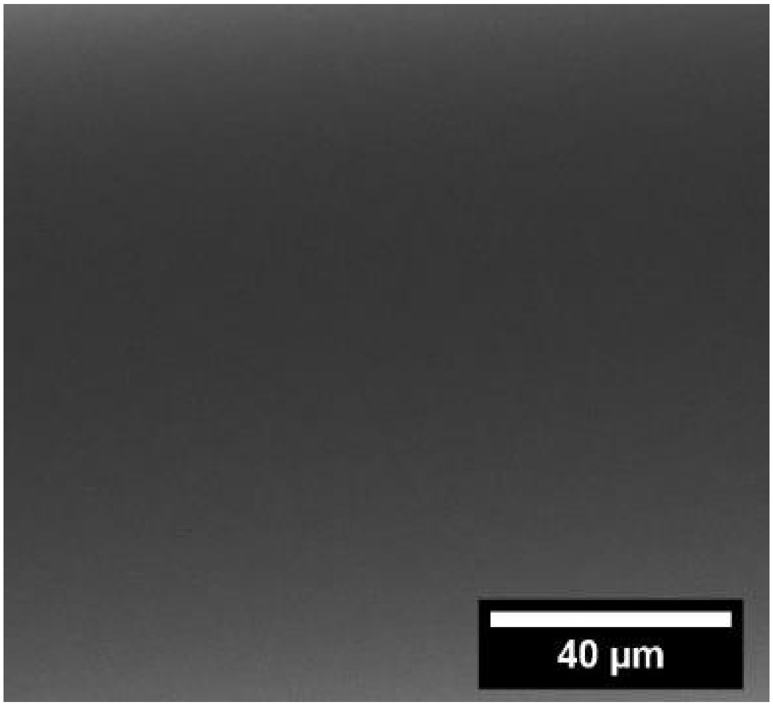

Figure 4.22. SEM image of an OI-B fiber surface after weathering in 50°C water for 7 days.

Figure 4.24 shows SEM images of the surfaces of pristine OI-B fibers and fibers exposed to 80%RH/50°C air for 28 days. The weathered samples show the presence of surface species similar to those shown above. EDS data was collected from the areas outlined in each of the images in Figure 4.24, and the resulting atom ratios are listed with each image. Clearly, these surface features are enriched in Ca and Na relative to the pristine glass surface.

Figure 4.25 shows EDS maps of sodium- and calcium-rich deposits that formed on the surfaces of OI-A fibers weathered for 100 days in 80%RH/50°C air. These maps also show that these features are rich in carbon, indicating that they are likely Na-carbonates.

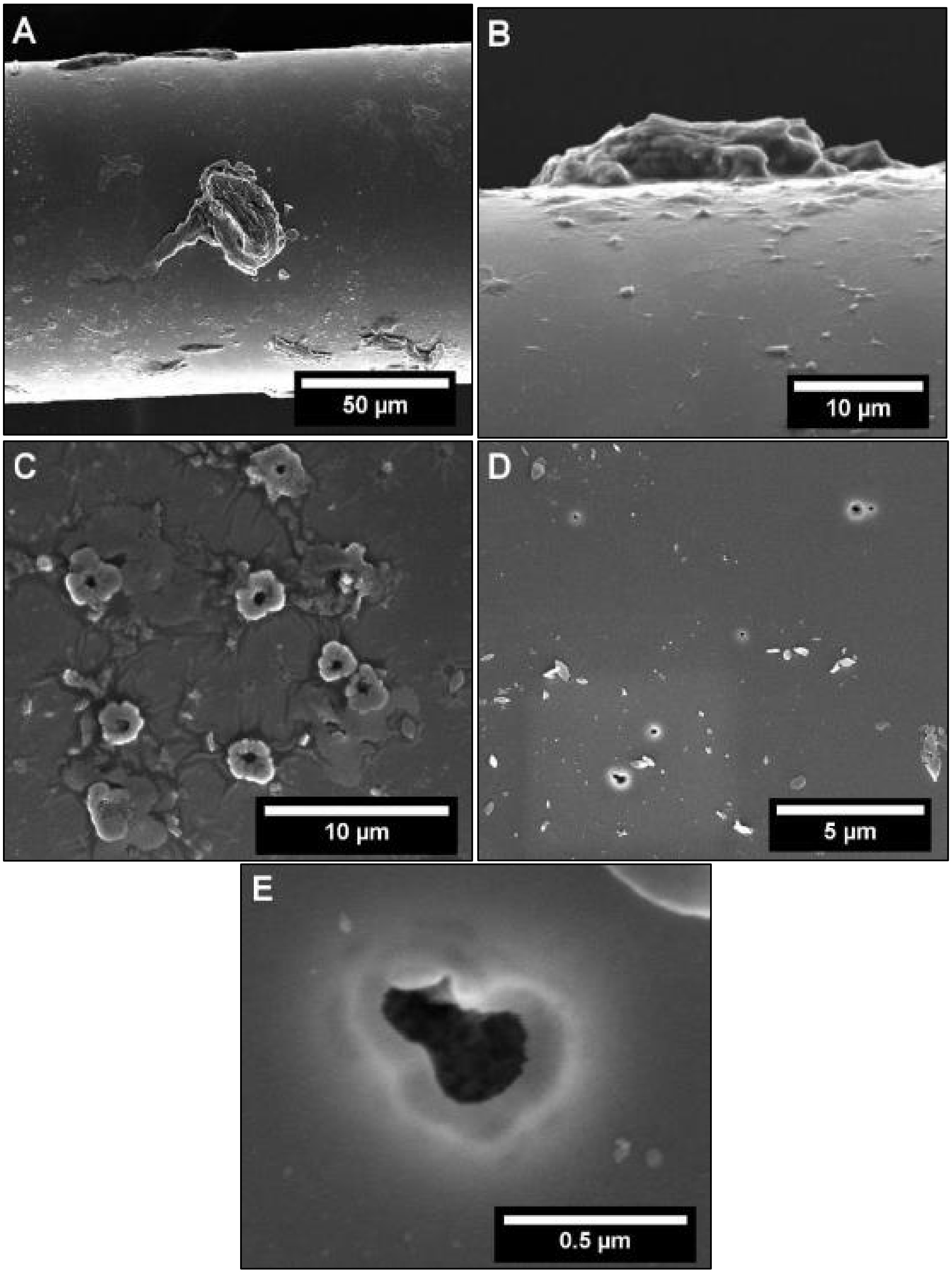

Figure 4.23. SEM images of OI-A fibers weathered for 100 days in 80%RH/50°C air; A) low magnification image of deposited crystals; B) magnified image of a surface feature; C) magnified image of surface bloom; D) image of a fiber surface after it was rinsed in distilled water; E) magnified image of an etch pit revealed after the fiber was rinsed in distilled water.

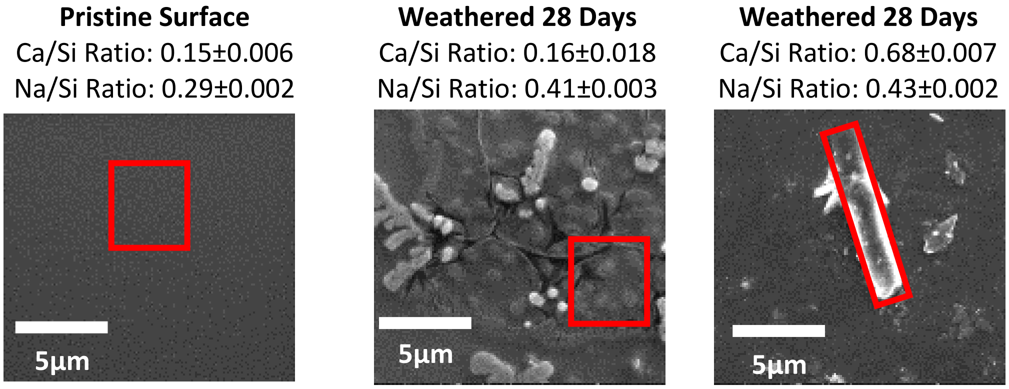

Pristine Surface
Ca/Si Ratio: 0.15±0.006
Na/Si Ratio: 0.29±0.002

Weathered 28 Days
Ca/Si Ratio: 0.16±0.018
Na/Si Ratio: 0.41±0.003

Weathered 28 Days
Ca/Si Ratio: 0.68±0.007
Na/Si Ratio: 0.43±0.002

Figure 4.24. SEM images of a pristine OI-B fiber (left) and fibers weathered 28 days in 80%RH/50°C air (center and right), along with atom ratios obtained by EDS for the areas outlined in each image.

The Raman spectrum from the pristine OI-B fiber surface is shown in Figure 4.26A, and is similar to spectra collected from soda-lime silicate glass, reported by Brawer and White [132]. The 945 cm^{-1} and 1095 cm^{-1} bands are associated with Si-O-Si asymmetric stretching modes, and the 535 cm^{-1} and 775 cm^{-1} bands have been assigned to the Si-O-Si bending modes and the Si-O-Si symmetric stretching modes, respectively[133]. A Raman spectrum collected from a surface feature on a fiber after 45 days of weathering in 80%RH/50°C air is shown in Figure 4.25B. New peaks at 1045cm^{-1} and 1280cm^{-1} indicate the presence of sodium bicarbonate[134] There is also a shift in the Si-O-Si symmetric stretching peak, from 775 cm^{-1} peak in the spectrum from the pristine glass to 790 cm^{-1} in the weathered glass. Scanning electron microscopic images of the surfaces of the OI-B fibers weathered in 10%RH/50°C air for up to 28 days are shown in Figure 4.28, and compared with the surface of a fiber weathered in 80%RH/50°C air for one day (Figure 4.28B). The surface of the latter fiber is covered with micron-scale corrosion spots, whereas those fibers weathered in 10%RH/50°C air show little evidence for corrosion, at least on the scale of the fiber weathered for a day in 80%RH/50°C. Higher magnification images, however, of the OI-A (Figure 4.28) and OI-B (Figure 4.29) fibers reveal the presence of sub-micron sized features that appear to inconsistently change size, shape, and distribution with weathering time. Rinsing the fibers in water the surface removes these surface features (Figure 4.30).

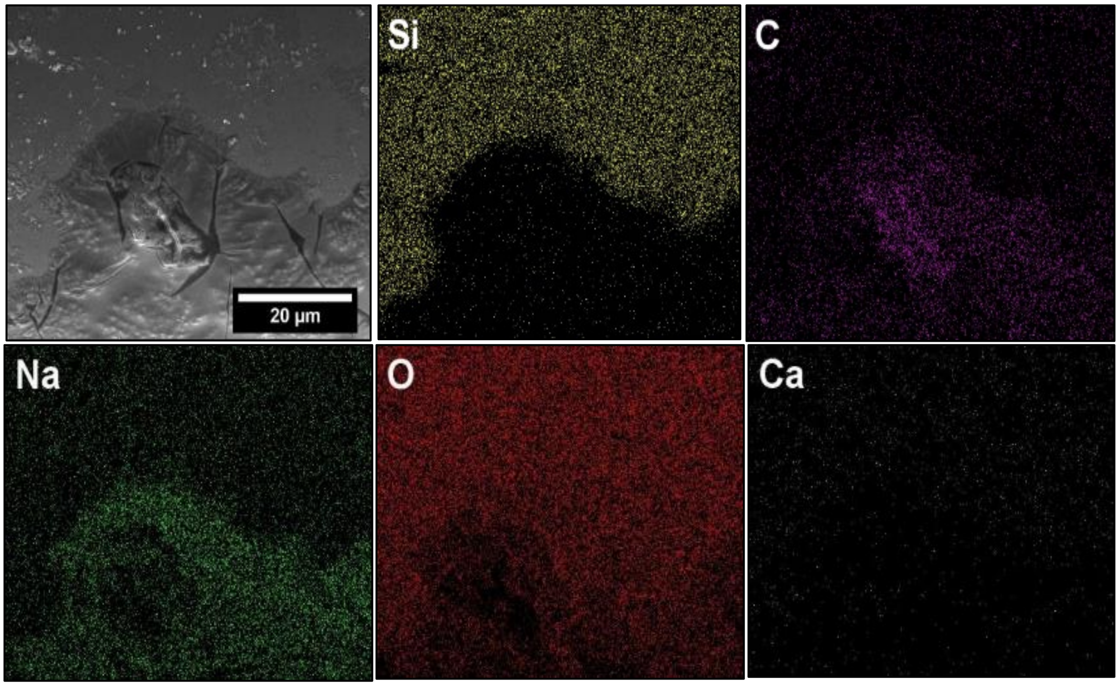

Figure 4.25. EDS x-ray scans of a surface feature on an OI-A fiber after 100 days in 80%RH/50°C air.

Examining the surfaces of the fibers weathered in ambient conditions in Figure 4.39 shows dark micron sized circles appearing after just 8 hours of exposure to ~40%RH/25°C air. Similar dark areas can be seen in Figure 4.28 and Figure 4.29 surrounding the features on several of the images. After 5 and 20 days of weathering in ~40%RH/25°C air, features are similar to those seen in appear in Figure 4.28 and Figure

4.29. After 60 days of weathering, features are ~1 micron and clustered in groups ~5 microns larger, and there are distinct dark areas located in between the clusters of features. Unlike Figure 4.28 and Figure 4.29, the features in Figure 4.30 appear to grow consistently over the weathering period.

For glasses with different residual water contents, microscopic examination of the surfaces of fibers weathered in 80%RH/50°C air shows that surface features across all glasses grow from ~5µm to ~20µm over the 30 days weathering period (Figures 4.33-4.36). The development of surface features over the first 7 days does not appear to be dependent on the residual water content of the glass. At 14 days, the 270ppm glass has distinct 15-20 micron sized features compared to the 140ppm or 180ppm glasses. At 30 days, all fibers have distinct surface features ~20 microns in size.

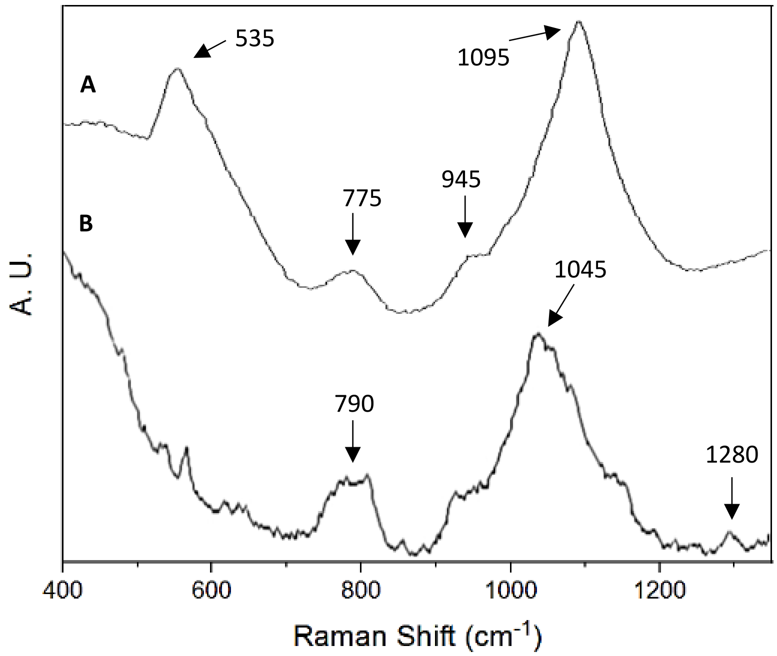

Figure 4.26. Raman spectrum from a pristine OI-B pristine glass fiber surface (A) and an OI-B glass fiber surface after weathering for 45 days in 80%RH/50°C air.

SEM images of the fiber surfaces weathered in 10%RH/50°C air are shown in Figure 4.36-Figure 4.39. The 180ppm and 270ppm surfaces appear to age similarly to the previous fibers examined (Figure 4.28 and Figure 4.29). However, there are grey spots on the surfaces of the140ppm fibers after 28 days that closely resemble the grey areas identified on the ambient weathered fibers (Figure 4.31).

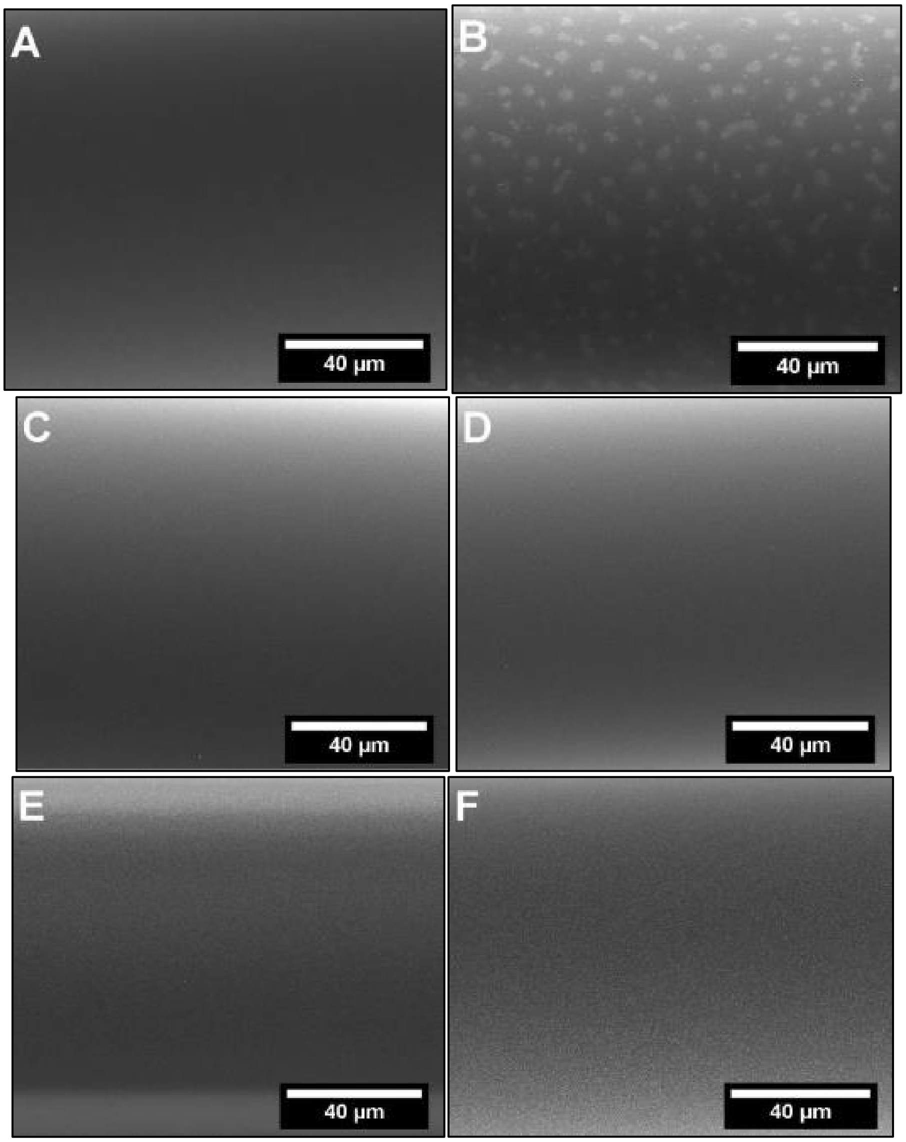

Figure 4.27. SEM images of OI-B fibers A)Pristine, b) weathered 1 day in 80%RH/50°C air, and weathered in 10%RH/50°C air for (c) 1 day, (d) 7 days, (e) 14 days, and (f) 28 days.

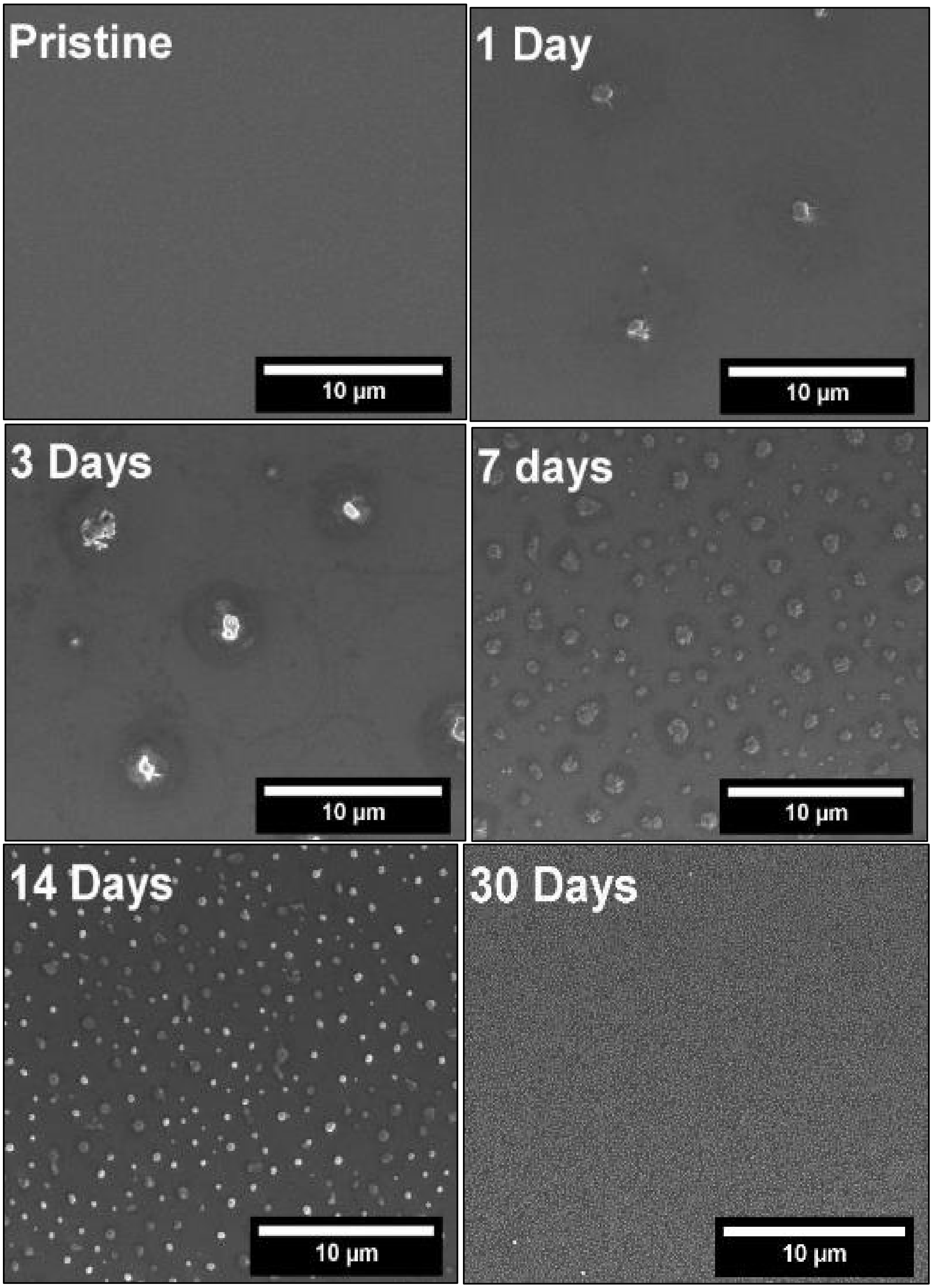

Figure 4.28. Higher magnification SEM images of OI-A fiber weathered for up to 30 days in 10%RH/50°C air.

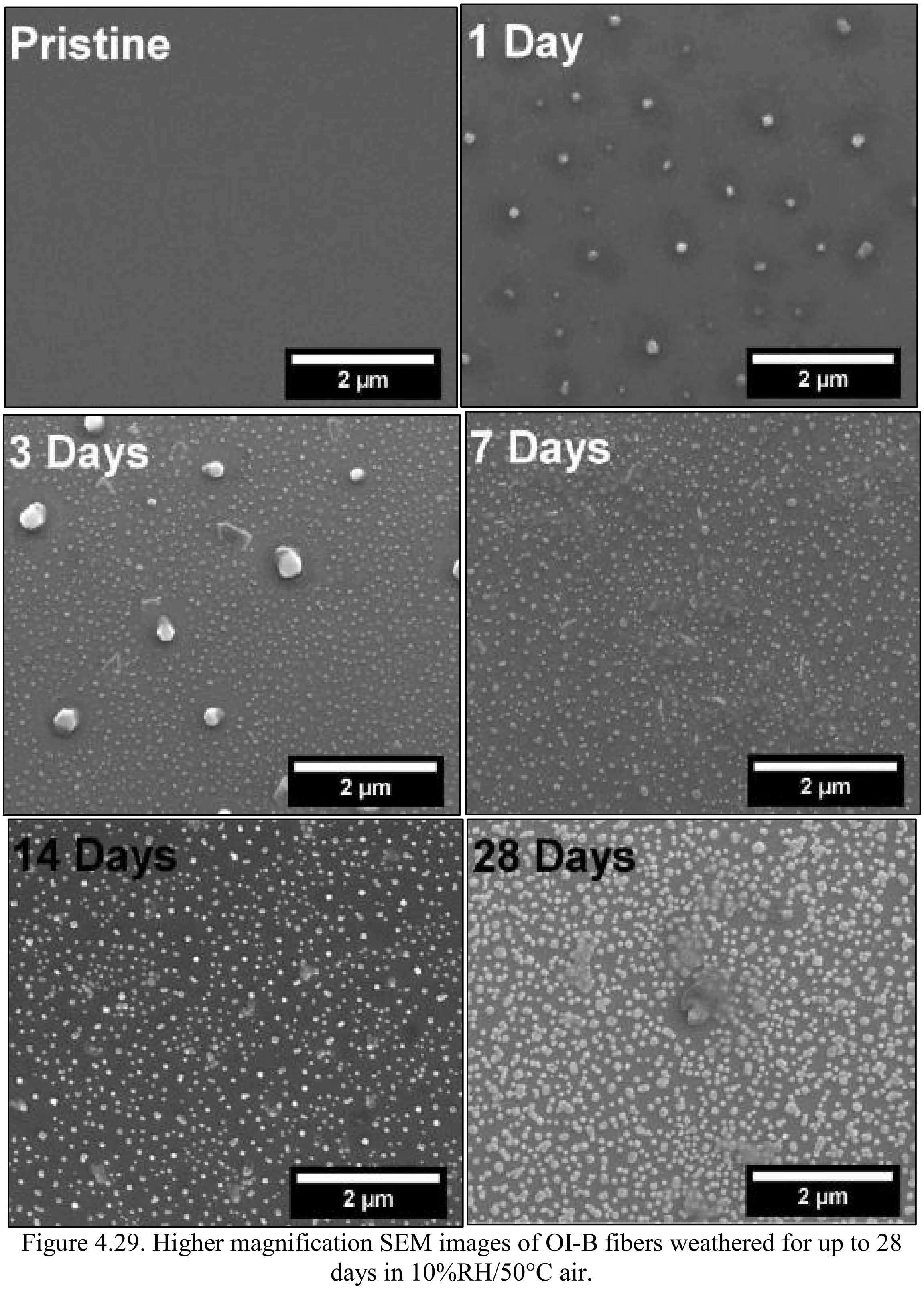

Figure 4.29. Higher magnification SEM images of OI-B fibers weathered for up to 28 days in 10%RH/50°C air.

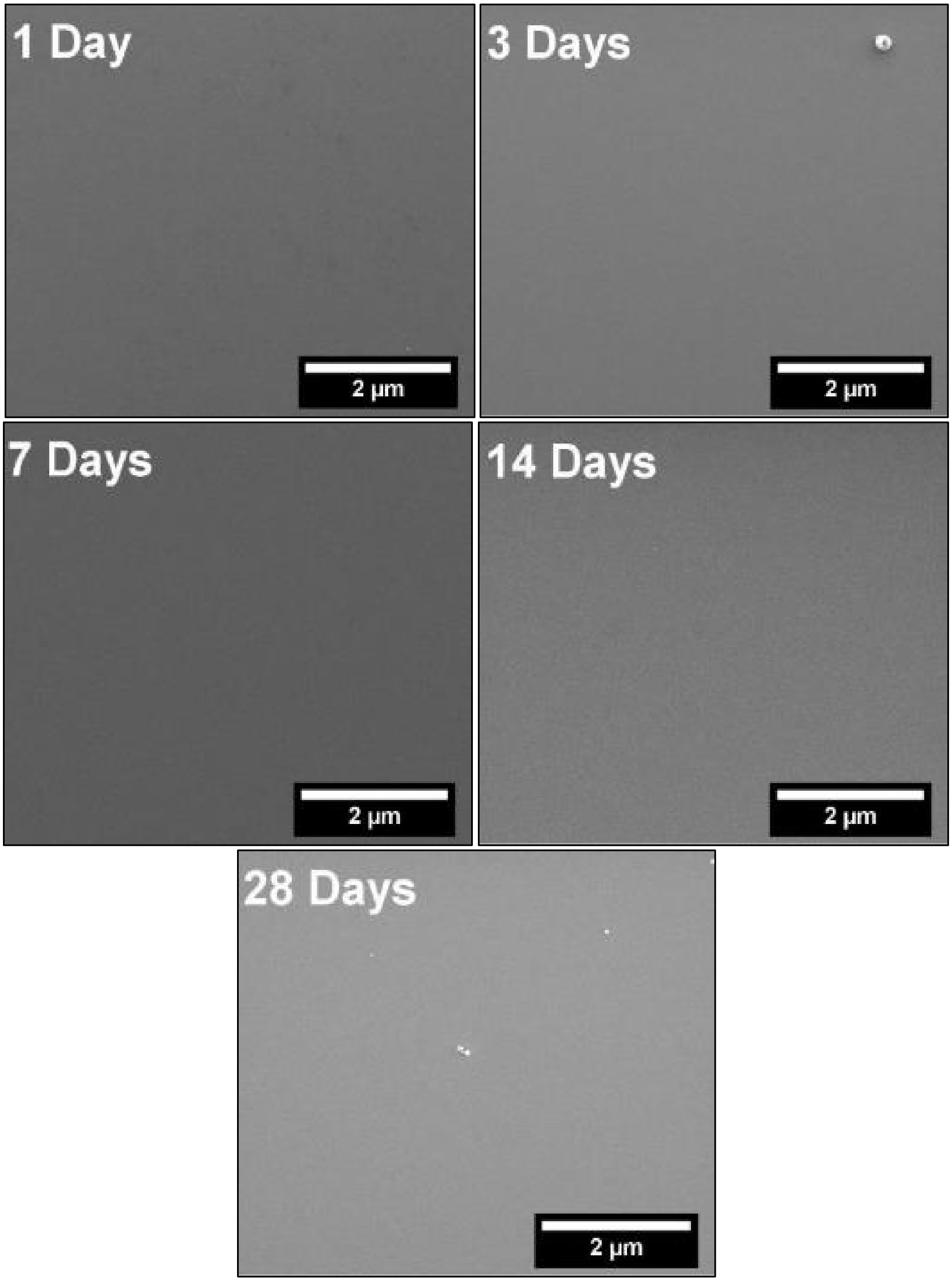

Figure 4.30. SEM images of OI-B fibers weathered for up to 28 days in a 10%RH/50°C air, then rinsed in distilled water.

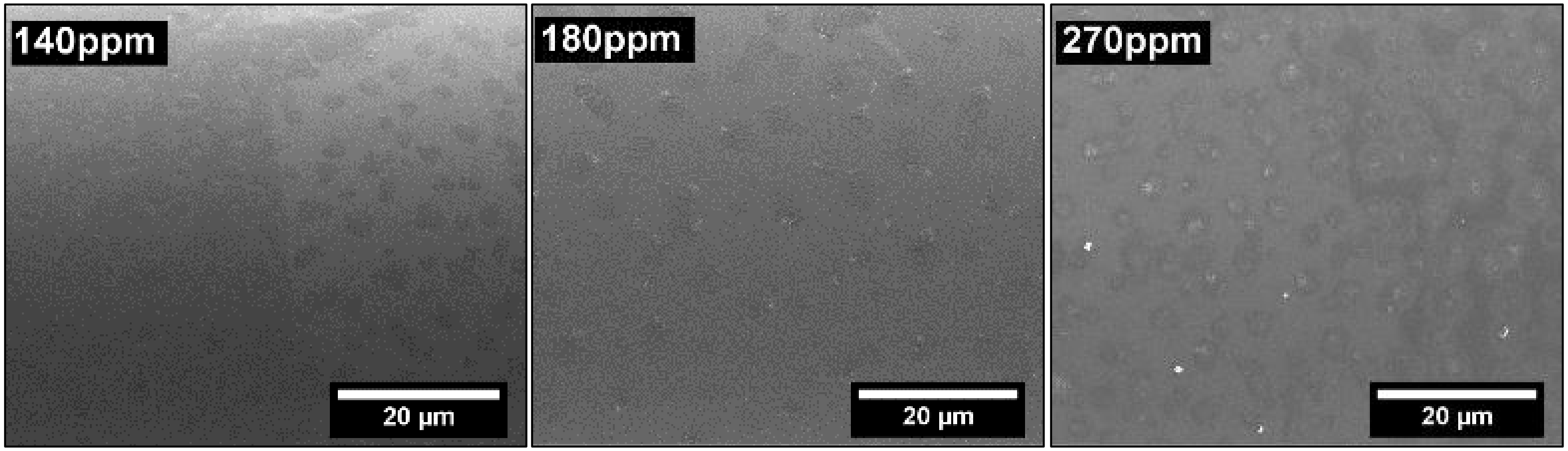

Figure 4.31 SEM images of fiber surfaces after weathering in 80%RH/50°C air for 1 day.

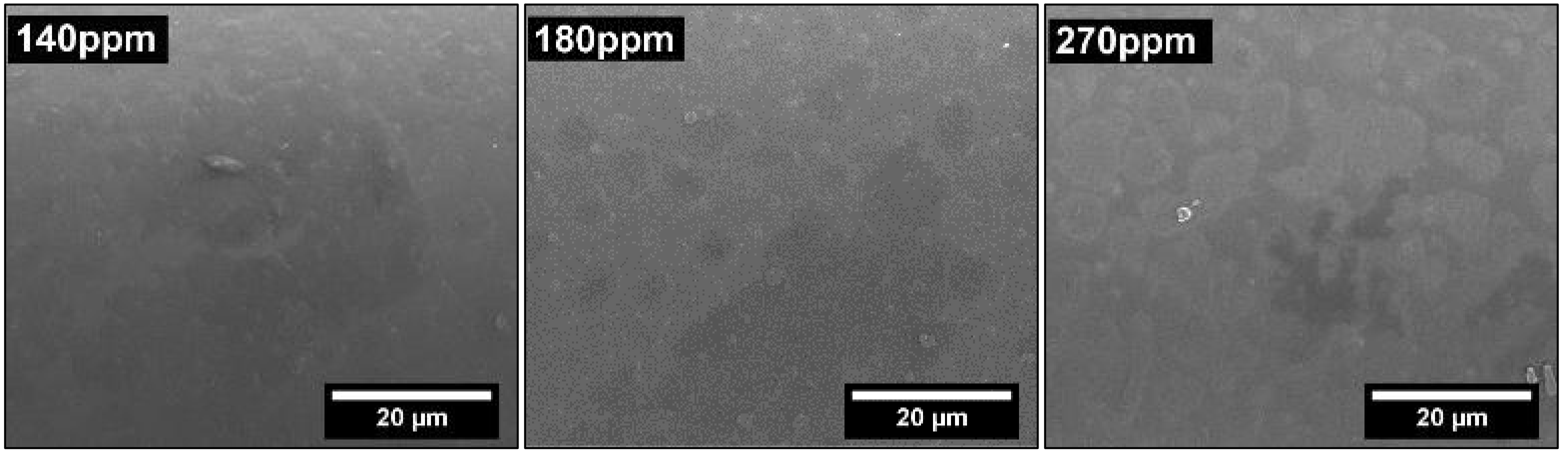

Figure 4.32. SEM images of fiber surfaces after weathering in 80%RH/50°C air for 7 days.

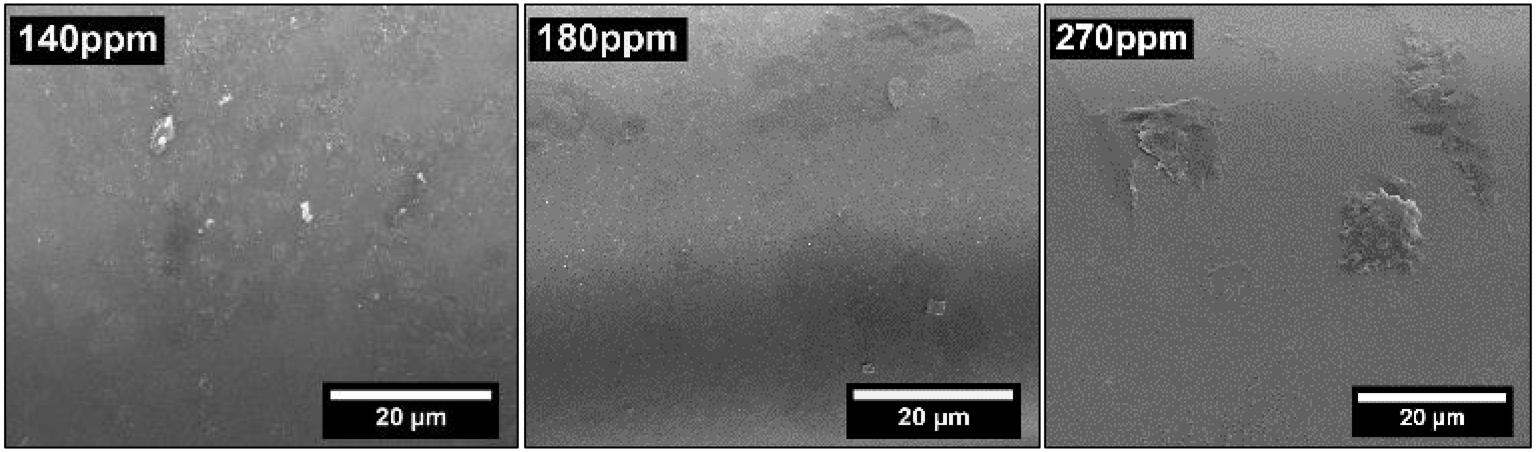

Figure 4.33. SEM images of fiber surfaces after weathering in 80%RH/50°C air for 14 days.

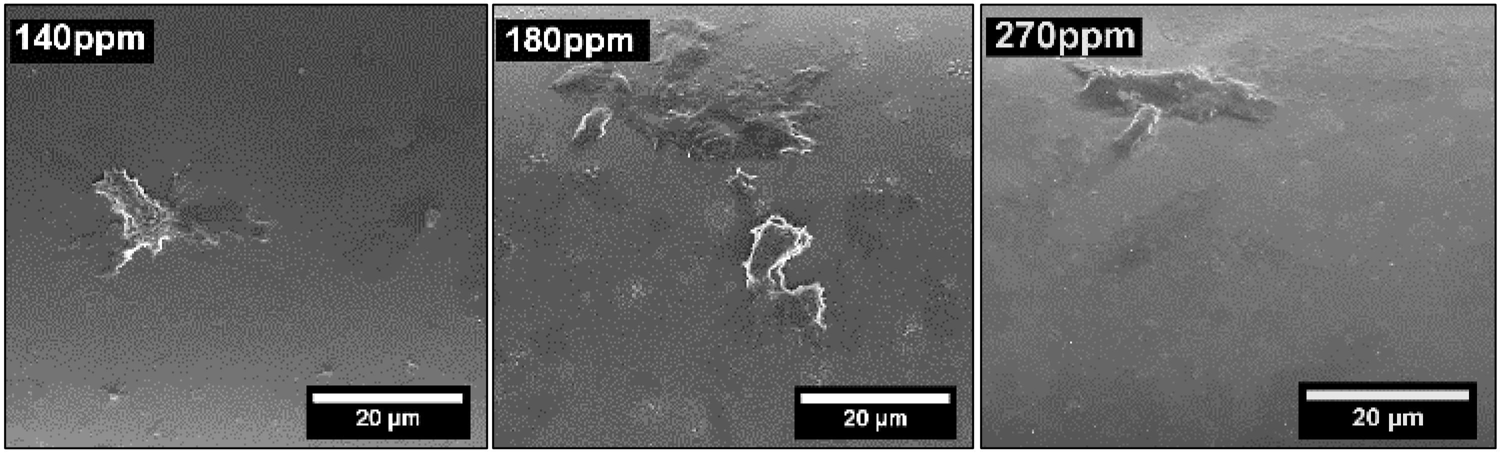

Figure 4.34. SEM images of fiber surfaces after weathering in 80%RH/50°C air for 28 days.

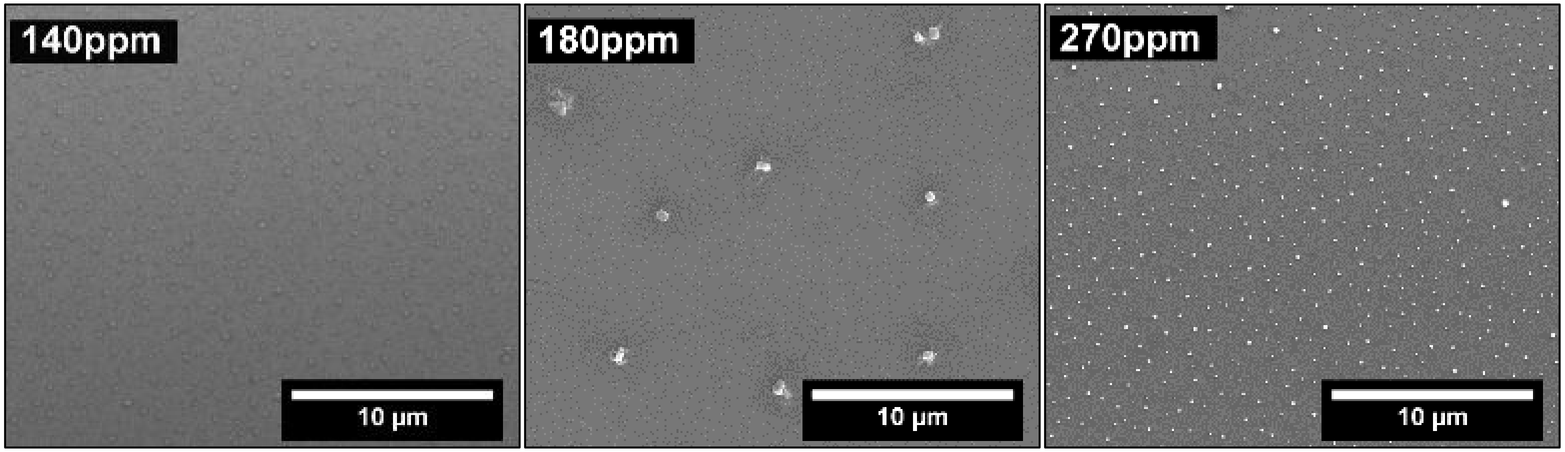

Figure 4.35. SEM images of fiber surfaces after weathering in 10%RH/50°C air for 1 day.

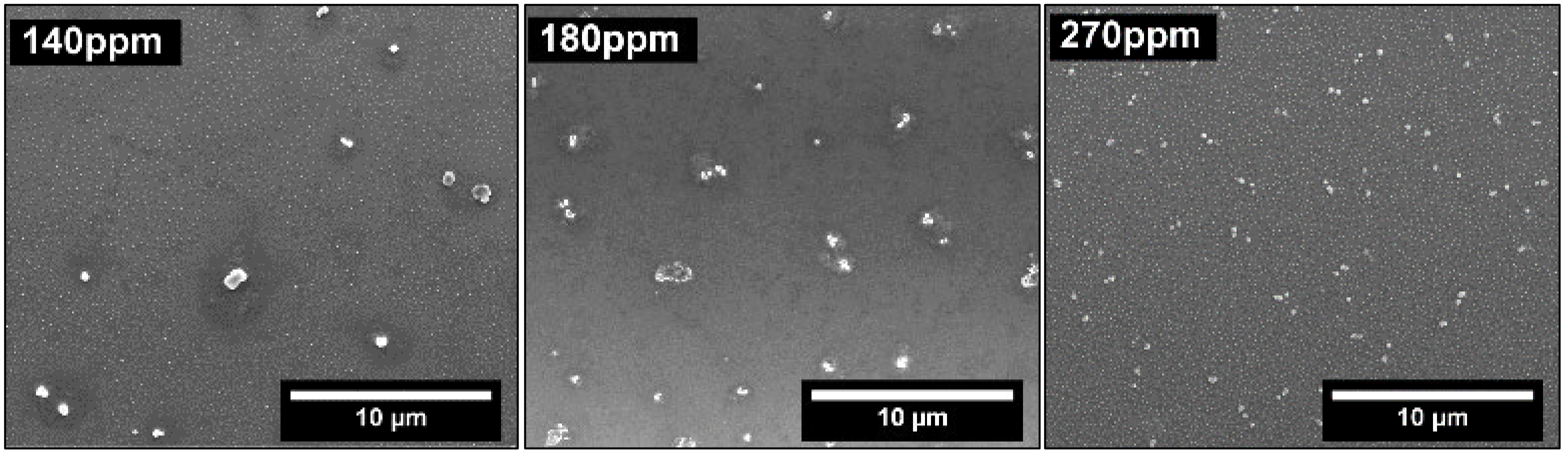

Figure 4.36. SEM images of fiber surfaces after weathering in 10%RH/50°C air for 7 days.

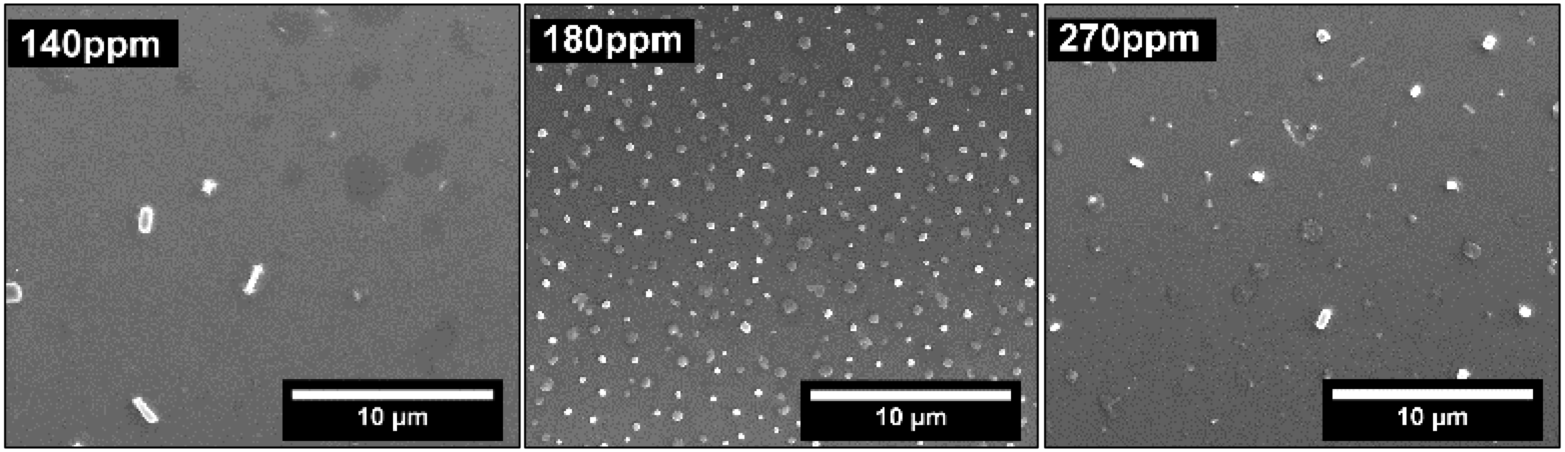

Figure 4.37. SEM images of fiber surfaces after weathering in 10%RH/50°C air for 14 days.

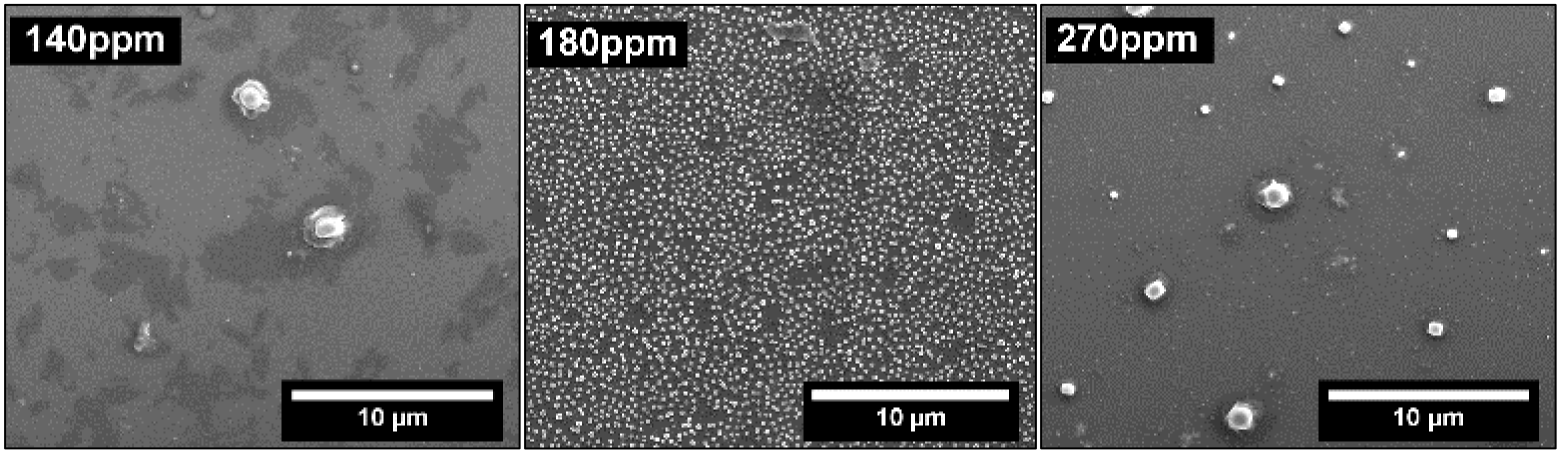

Figure 4.38. SEM images of fiber surfaces after weathering in 10%RH/50°C air for 28 days.

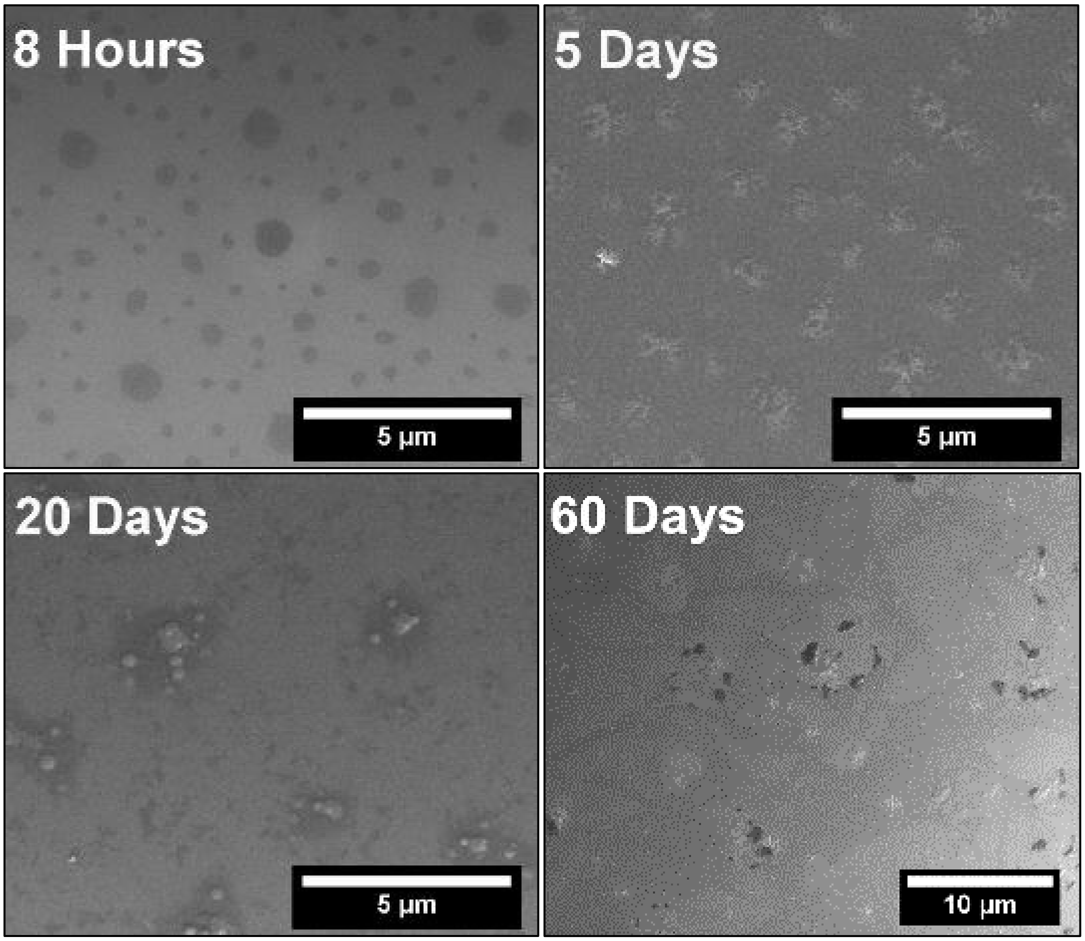

Figure 4.39. SEM images of OI-A fiber weathered for up to 60 days in ~40%RH/25°C air.

4.3. DISCUSSION

4.3.1. Processing Effects on Weathering of Glass Fibers. The changes in the breadths of the failure distributions for the OI-A fibers through 95 days of weathering in 50°C/80%RH air, shown in Figure 4.1 and Figure 4.3, contrasts with the relatively consistent failure distributions for the OI-B fibers, shown in Figure 4.2 and Figure 4.4. Defects created by processing or handling can limit glass strength[4], [135], but both sets of pristine fibers have similar, narrow failure distributions, so there seems not to be significant differences in the respective pristine samples, making it more likely that there are differences in the development of the strength-limiting weathering products on the respective glass surfaces. This would indicate preferential corrosion on the glass surface where some weathering defect sites grow faster than others or the distribution of these weathering flaws is broader and/or non-uniform in size. Because critical flaws could not be observed due to their nanoscopic size, it was not possible to determine whether the failure strain distributions were controlled by non-uniform flaw growth or broader starting distributions. The narrowing of failure strains for the OI-A fibers after about three weeks of weathering (Figure 4.1and Figure 4.3) indicates that the critical flaw distributions are becoming more uniform.

The OI-A glass fibers were produced principally by adjusting the drawing speed to maintain consistent fiber diameters. It was not uncommon in these experiments to produce large numbers of fibers with diameters that fell out of the acceptable range. In later experiments using OI-B glass, the drawing process was modified to use a constant drawing speed, while adjusting the height of the copper cooling and furnace temperature to maintain constant fiber diameters. Drawing stresses are known to affect the properties of glass fibers. Increasing the axial stress during the drawing of E-glass fibers has been shown to increase both the anisotropy of the structure and the orientation of defects to produce residual stresses[136]. Carnali et. al. found that the increased stretching forces on pristine blown glass surfaces increased the number of surface heterogeneities[137], and these heterogeneities were found to etch preferentially when exposed to water. It is possible that there were differences in the drawing stresses used to produce the OI-A and OI-B fibers and these different conditions created heterogeneities in surface composition that reacted with water in different ways to produce broader distributions of strength limiting flaws when the OI-A fibers were exposed to humid conditions.

4.3.2. Decrease in Failure Strains from Weathering. OI-A and OI-B fiber failure strains decrease with increasing weathering time in humid air (Figure 4.5 and Figure 4.6) and in water (Figure 4.7). The decrease in failure strain after weathering in humid environments has been observed for other silicate glasses [95], [110], [111], [138]. For both OI-A and OI-B, the average inert failure strain decreases rapidly over the first 21 days of weathering in 80%RH/50°C air. Fibers decrease at a rate of ~5% per day when tested in inert conditions. After 14 days, the failure strains decrease at a much slower rate of ~0.006% per day for the remainder of the experiment (Figure 4.5). SLS fibers weathered in 50°C water undergo a similar rapid initial decrease in average failure strain, although the rate of decrease appears to level out after 7 days instead of 14 days (Figure 4.7). This initial rapid decrease in average failure strain with weathering has been seen for E-glass samples as well[110], [111], [139]. E-glass fibers weathered and tested under identical conditions undergo a ~1.5% decrease per day in failure strains in the first seven days[111], which is considerably slower than the degradation of failure strain in the present SLS glass fibers.

The ratio of the failure strain measured in air and in liquid nitrogen for pristine fibers are shown in Table 4.1. There is no noticeable different between OI-A trial 1 and OI-B trials 1-3. Figure 4.40 shows the ratio of failure strains measured in room temperature air (40% RH) (Figure 4.5) to those measured under liquid nitrogen (Figure 4.6) for the weathered OI-A and OI-B glasses. The failure strain ratio for pristine fibers range from 0.34-0.40 and increases to 0.45-0.56 after 30 days of weathering independent of water content or source glass. The failure strain values measured in air depend both on the fatigue effects of atmospheric water as well as any physical damage that weathering does to the fiber surfaces, whereas the failure strain values in liquid nitrogen depend principally on surface damage since water activity is minimized. The increase in the failure strain ratios with weathering indicate that the relative influence of fatigue is less for the weathered fibers, in agreement with the increase in the fatigue parameters measured for both sets of SLS fibers with increasing weathering time (Figure 4.15).

Table 4.1. Ratio of the failure strain measured in air and in liquid nitrogen for pristine fibers.

Trial	**Failure Strain Ratio**
OI-A Trial 1	0.34 ± 0.02
OI-B Trial 1	0.39 ± 0.01
OI-B Trial 2	0.36 ± 0.01
OI-B Trial 3	0.37 ± 0.01

Since the effects of water are minimized when testing is done under liquid nitrogen, the decreasing failure strains, and implied decreasing fiber strength, with weathering time is attributed to the development of larger critical flaws created by the weathering reactions. The relationship between failure strength (σ_f) and an estimated critical flaw depth (c*) can be estimated using the Griffith equation[11]:

$$\sigma_f = \left(\frac{2E\gamma}{\pi c^*}\right)^{1/2} \tag{4.1}$$

where E is the elastic modulus and γ is the fracture surface energy. If non-linear elastic modulus effects are ignored, then failure strain will be directly proportional to failure strength and will have a similar dependence on the nature of the critical flaw, c*. Therefore, the decrease of average inert failure strain with weathering time should be inversely correlated with the increase in critical flaw size. Using the estimation for the fourth order elastic modulus derived by Gupta and Kurkjian, described in Section 3.3.1, the failure strength (σ) can be determined from failure strain (ε) and the inert failure strain (ε^*) using equation 4.2:

$$\sigma = E_0\varepsilon + \frac{1}{2}E_1 - \left(\frac{\varepsilon^3}{3}\right)\left(\frac{E_0+E_1\varepsilon^*}{(\varepsilon^*)^2}\right) \tag{4.2}$$

where E_0 and E_1 are the second and third order elastic moduli, respectively. Since $\varepsilon = \varepsilon^*$ in inert conditions, this equation can be simplified to:

$$\sigma_f^* = \frac{2}{3}E_0\varepsilon_f^* + \frac{1}{6}E_1{\varepsilon_f^*}^2 \tag{4.3}$$

Griffith's equation (Equation 4.1) can be used to estimate the critical flaw depth from the inert failure strengths derived from Equation 4.3. Using values for the second and third order moduli, 72 GPa, and 121 GPa, respectively, determined by Cavaill using Brillouin scattering[121], the critical flaw sizes were estimated and are shown in Figure 4.41.

For pristine fiber surfaces, AFM characterization revealed topological features that were submicron wide and 1-2nm deep (Figure 4.18). Interestingly, the depths of the features correlate well with the predicted critical flaw size using the Griffith equation derived from the failure strains of the pristine fibers broken in liquid nitrogen (Figure 4.41). These surface "flaws" could be the critical stress concentrators that cause failure on the pristine fiber surfaces. They also could serve as nucleation sites for the dendritic crystals observed with AFM after one day of weathering in 80%RH/50°C air (Figure 4.18).

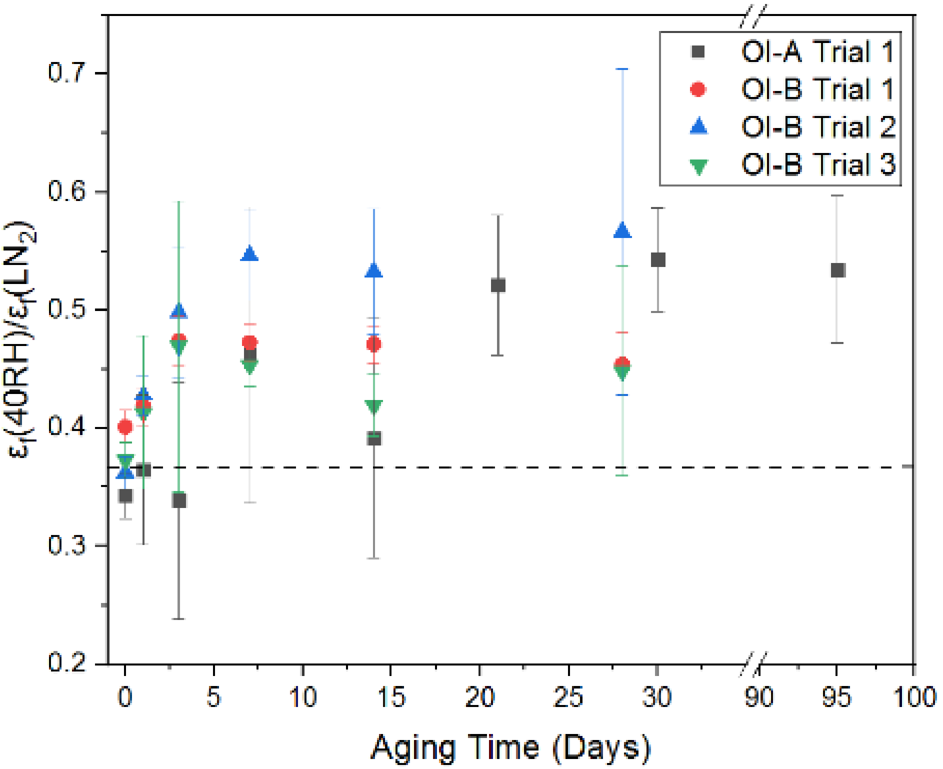

Figure 4.40. Ratio of the average failure strain measured in room temperature air at 40%RH to those measured in liquid nitrogen for OI-A and OI-B glasses weathered in 50°C/80%RH air.

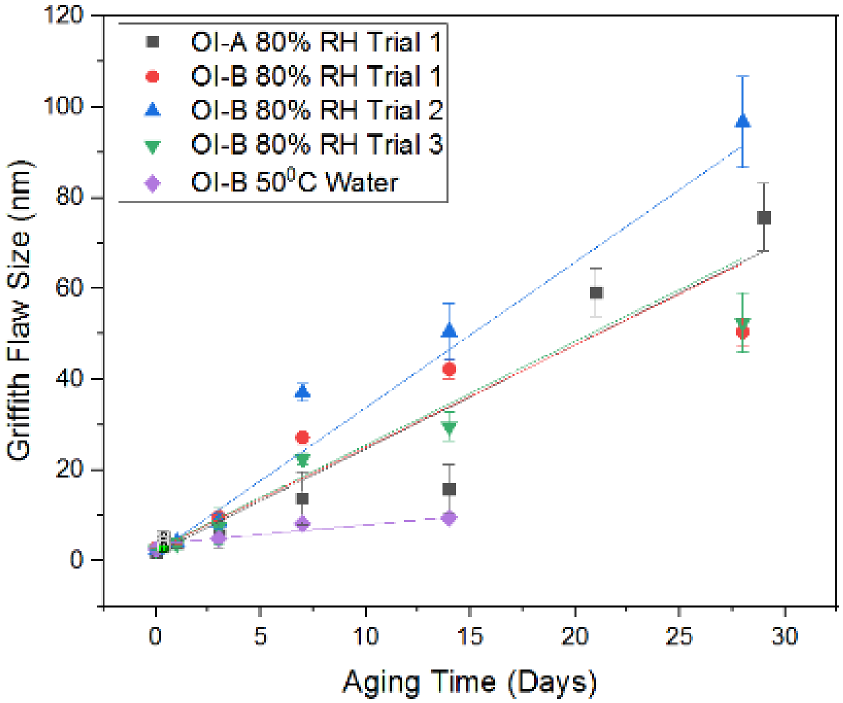

Figure 4.41. Estimated critical flaw sizes derived from the average failure strains measured under liquid nitrogen for SLS fibers weathered in 80%RH/50°C air and in 50°C water. Lines are linear fits to the estimated flaw sizes.

After three days, the surface roughness from AFM is >50nm, which is larger than the predicted flaw sizes after 3 days of weathering in 80%RH/50°C in Figure 4.41. It is important to note that the Griffith equation assumes that all flaws are scratch-like and atomically sharp [140], which is a reasonable assumption for a pristine fiber surface. For aged and weathered surfaces, the shape and uniformity of the critical flaws is likely to be changing with time, and therefore, the estimated flaw size would change as well. Alternatively, the size and shape of the developing surface features observed with AFM may not be predictive of the critical flaw size.

Beyond three days, the dendritic features appear to coalesce and form features too large to be observed by AFM. The coalescence of dendritic surface features into larger features on SLS surfaces over a seven days weathering period in 100%RH/25°C air has been previously observed [142]. The SEM images in Figure 4.19 and Figure 4.20 show continuous growth of these surface features over the 30-day weathering period in 80%RH/50°C air. Surface features with dimensions of ~2-5μm appear after one day of weathering, and these features grow and consolidate to form larger features (20-40μm) after 30 days of weathering. The features after 14 days of weathering in 80%RH/50°C air appear to be needle-like or hexagonal in nature (Figure 4.21), which is consistent with the morphologies of crystals grown on the inside of weathered container glass bottles stored in ambient conditions for a year[70] (Figure 4.42).

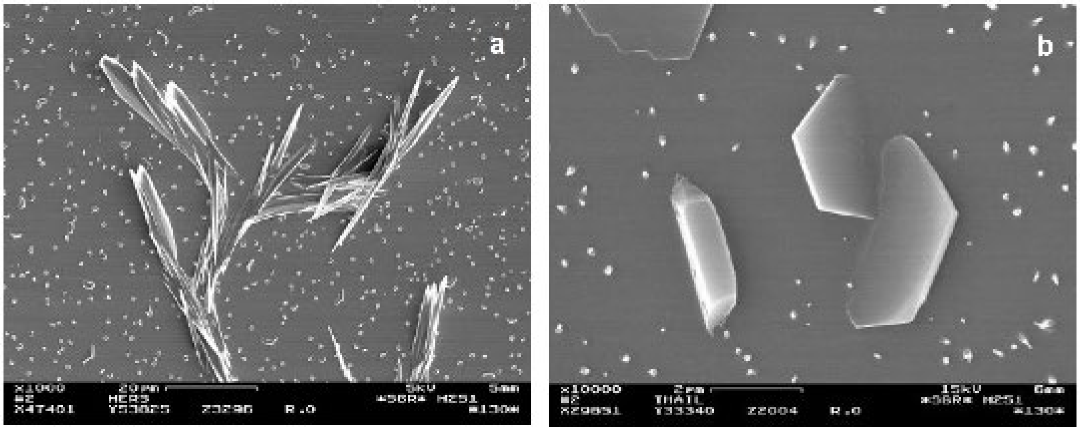

Figure 4.42. SEM images of a glass bottle surface stored outside and with direct exposure to the environment for 1 year[70].

The relationship between these large surface features and the decrease in failure strains due to the growth of critical flaws is not easily determined. Verita et. al. washed the interior of SLS bottles after weathering and observed the presence of hexagonal pits[71]. The washing method was not disclosed, but the hexagonal pits closely matched the hexagonal growths on the unwashed surface (Figure 4.43).

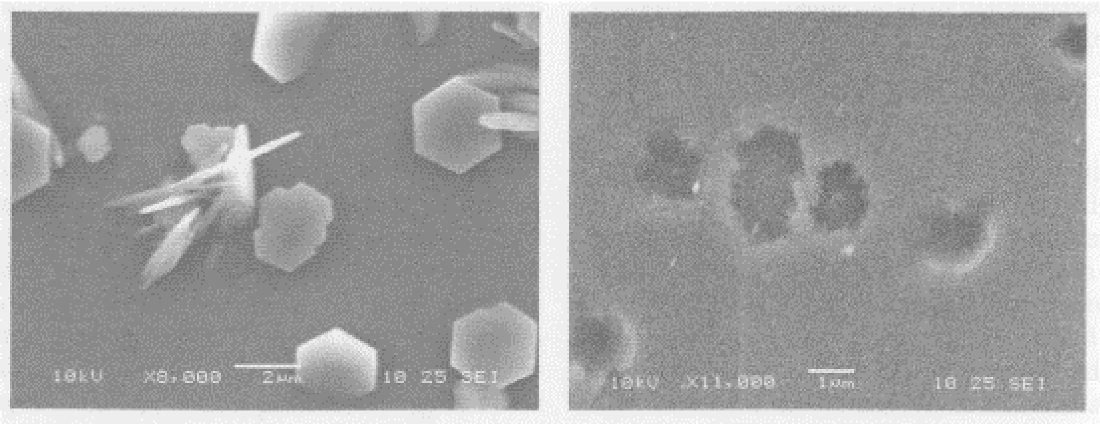

Figure 4.43. SEM images of glass bottle surface features stored for 1 year outside with direct exposure to the environment before (left) and after (right) cleaning [71].

Rinsing OI-B fibers in distilled water revealed no obvious surface pits after the first 30 days of weathering (Figure 4.21). Corrosion products remained attached to the surfaces and so it is possible that the cleaning method was insufficient to reveal damage. Samples that were weathered for 100 days in 80%RH/50°C air created much more extensive surface bloom features that were associated with obvious etch pits that were revealed after rinsing these fibers in water (Figure 4.23). These pits, which were widely distributed over the fiber surface, are evidence for the local dissolution of the glass. If such pits are the critical flaws that limit the strengths of severely weathered glass, then the tight distributions of failure strains for these fibers (e.g., Figure 4.3), indicate that they must have similar dimensions and distributions.

Characterization by EDS of the surface features that form after 28 days of weathering show that they are enriched in calcium and sodium with respect to silicon concentration, Figure 4.24, as well as carbon, Figure 4.25. These analyses are consistent with the formation of sodium carbonate and calcium carbonate, as has been seen in previous studies of weathered SLS glass [68], [70], [71], [134], [143].

Fibers immersed in water do not show the formation of any surface precipitation products (Figure 4.22). This is likely because the leached ions are able to diffuse into the surrounding water away from the fiber surface. Additionally, the Weibull moduli for fibers aged in 50°C water and fibers weathered in 80%RH/50°C conditions are similar, which indicates the distributions of flaws are similar between the two conditions.

The surface features and critical flaw development is related to the macroscopic weathering reactions on SLS surfaces. In humid weathering conditions, water droplets first condense on the fresh glass surfaces, where an ion-exchange reaction occurs between the alkali ions in the glass and protonated water, to produce a hydrated, alkali depleted layer on the glass and an alkaline water layer on the glass surface [67]. Equations 4.4 and 4.5 describe the possible ion exchange reactions:

$$-\ \underset{|}{\overset{|}{Si}}\ - O^-Na^+ + H_2O \longrightarrow -\ \underset{|}{\overset{|}{Si}}\ - OH + Na^+ + OH^- \tag{4.4}$$

$$-\ \underset{|}{\overset{|}{Si}}\ - O^-Na^+ + H_3O^+ \longrightarrow -\ \underset{|}{\overset{|}{Si}}\ - OH(H_2O) + Na^+ \tag{4.5}$$

When the pH of the water layer exceeds about 9 [67], the siloxane bonds in the silicate network can be hydrolyzed to release silicic acid, as represented by Equation 4.6:

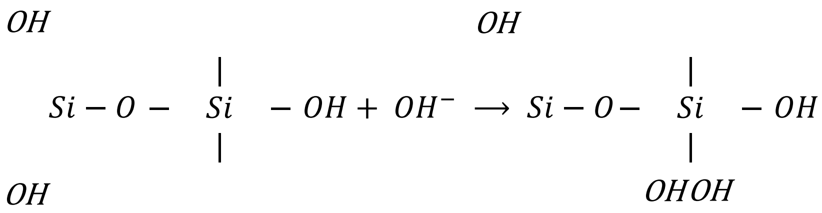

$$Si - O - \underset{OH}{\overset{OH}{\underset{|}{\overset{|}{Si}}}} - OH + OH^- \longrightarrow Si - O - \underset{OHOH}{\overset{OH}{\underset{|}{\overset{|}{Si}}}} - OH$$

$$\longrightarrow Si - O^- + Si(OH)_4 \qquad (4.6)$$

Another reaction on the glass surface is hydration [67], the process by which water molecules diffuse into the glass structure via voids in the glass or surface film structure. The rate of diffusion is dependent on the void size. Hydration can occur simultaneously with ion-exchange and hydrolysis reactions. As the hydrolysis reactions break down the silicate network, larger voids and open pathways created in the structure allow for further penetration of water molecules, which in turn promote further ion-exchange and hydrolysis reactions.

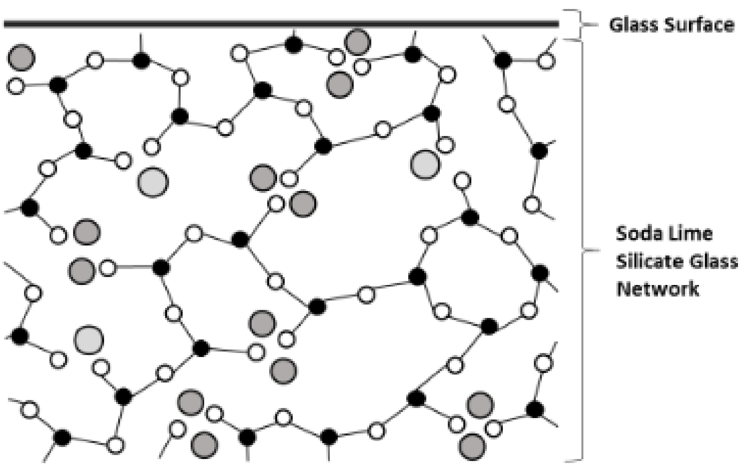

Figure 4.44. Pristine glass surface.

The effect of these weathering processes is summarized in the series of diagrams in Figure 4.44 - Figure 4.48. At first, the ion exchange reactions (Equation 4.4 and Equation 4.5) result in the accumulation of OH^- and Na^+ ions and increase the pH that would promote rapid hydrolysis reactions (Figure 4.45)[71]. However, the increase in pH is inhibited by the dissolution of acidic gases in the atmosphere, such as SO_2, CO_2, and NO_x, which dissolve into the surface water droplets or layers (Figure 4.46).

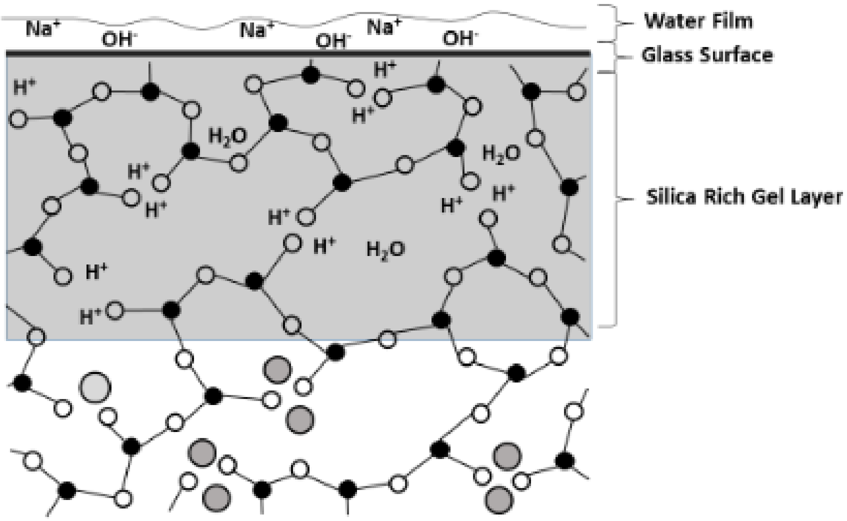

Figure 4.45. Formation of a water film after exposure to humid conditions. Ion-exchange of alkali and alkaline ions with water creates a silica-rich gel layer. Hydration of the gel layer occurs by the diffusion of water molecules.

The decrease in the surface pH slows the hydrolysis reactions and dissolution of the silicate network. Eventually, the leached alkali and alkaline earth ions react with the acidic gases to form alkali and alkaline carbonates, sulfates, etc. At some point, the solubility limit of these products in the surface water layer is reached, and crystalline deposits precipitate on glass surface [68], [70] (Figure 4.47). Despite the decrease in surface pH due to acidic gases, the presence of pits (Figure 4.23) indicate that the pH is still high enough that hydrolysis is occurring to some extent (Figure 4.48).

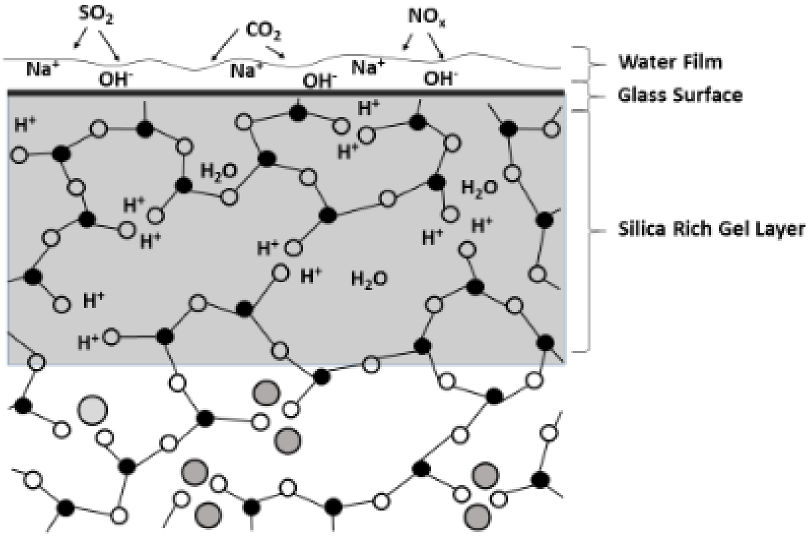

Figure 4.46. Dissolution of acidic gases from the atmosphere into the alkaline surface water film.

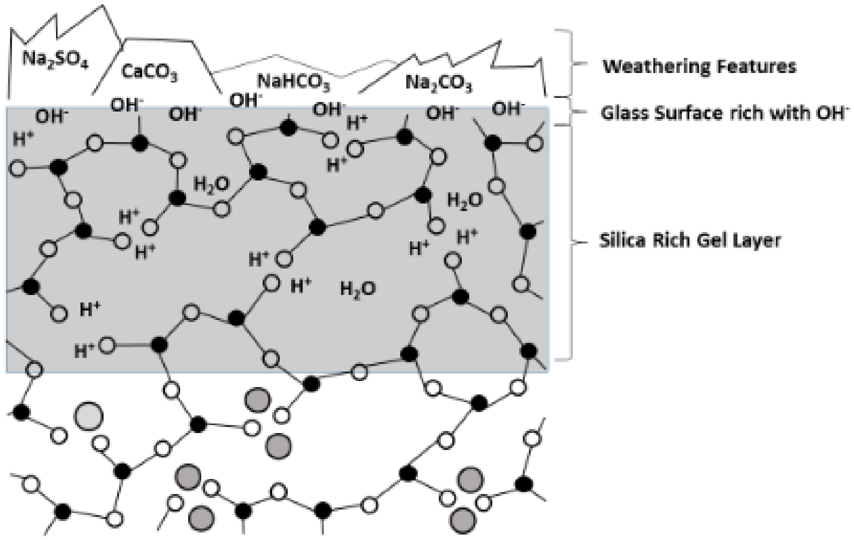

Figure 4.47. Development of weathering products from reactions of alkali and alkaline ions with acidic gases.

The corrosion processes (Figure 4.49 - Figure 4.51) in water are similar to those in humid air, however the OH^- and Na^+ ions that are produced can diffuse away from the glass surface through the water (Figure 4.49). This prevents the local pH from rapidly increasing and therefore, slowing or limiting the attack on the silicate structure. Additionally, it is possible that the absence of precipitated crystallites (Figure 4.22) may influence the shape and uniformity of critical flaws. The higher failure strains for fibers aged in 50°C water for 14 days compared to fibers weathered in 80%RH/50°C conditions (Figure 4.7) could be attributed solely to flaw shape rather than the kinetics of the surface reactions. Figure 4.50 shows the development of flaws on aged fiber surface that are similar to the flaws hypothesized to develop on a weathered fiber surface (Figure 4.36). Figure 4.51 shows the development of alternative flaw shape. Further work is needed to determine the underlying topography in order to better understand the nature and true size of the critical flaws on weathered and aged surfaces.

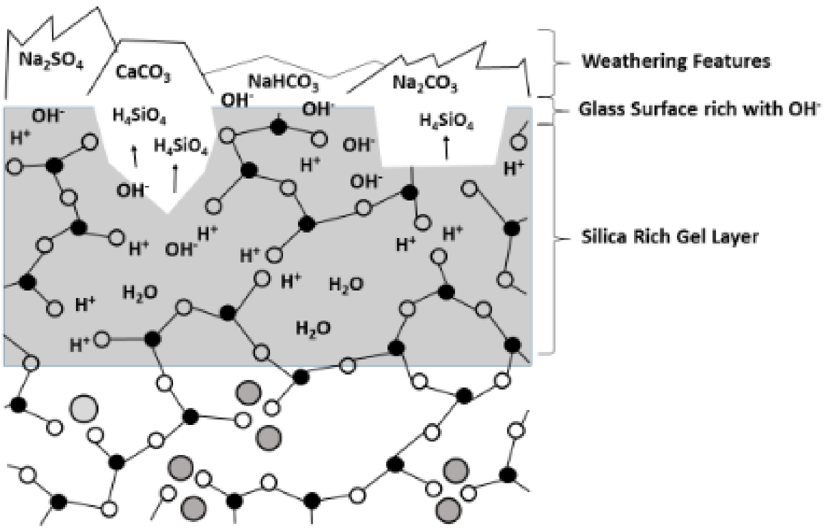

Figure 4.48. Acceleration of hydrolysis reactions that break down the silicate network.

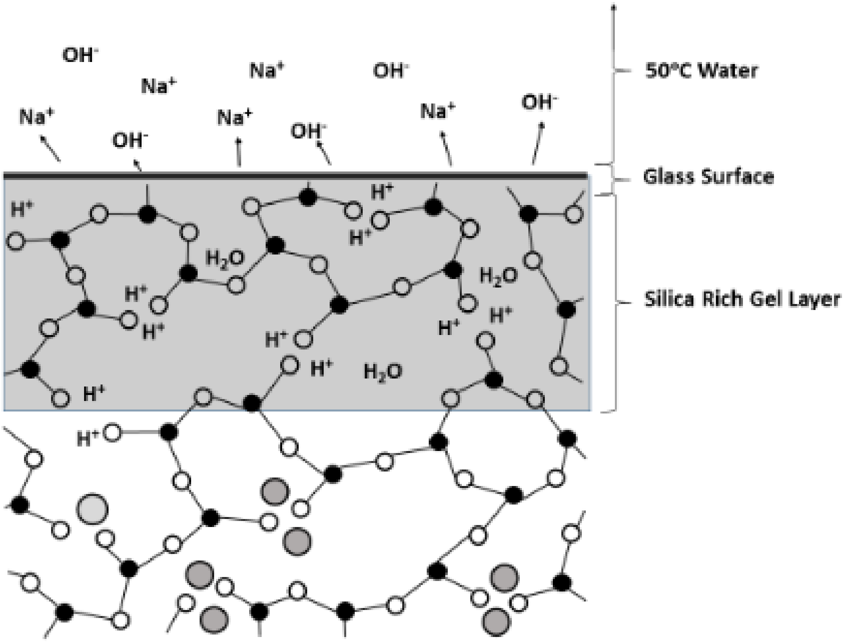

Figure 4.49. SLS glass in water: Ion-exchange of alkali and alkaline ions with water creating a silica rich gel layer. After ion exchange, ions diffuse away from glass surface. Hydration of gel layer from diffusion of water molecules.

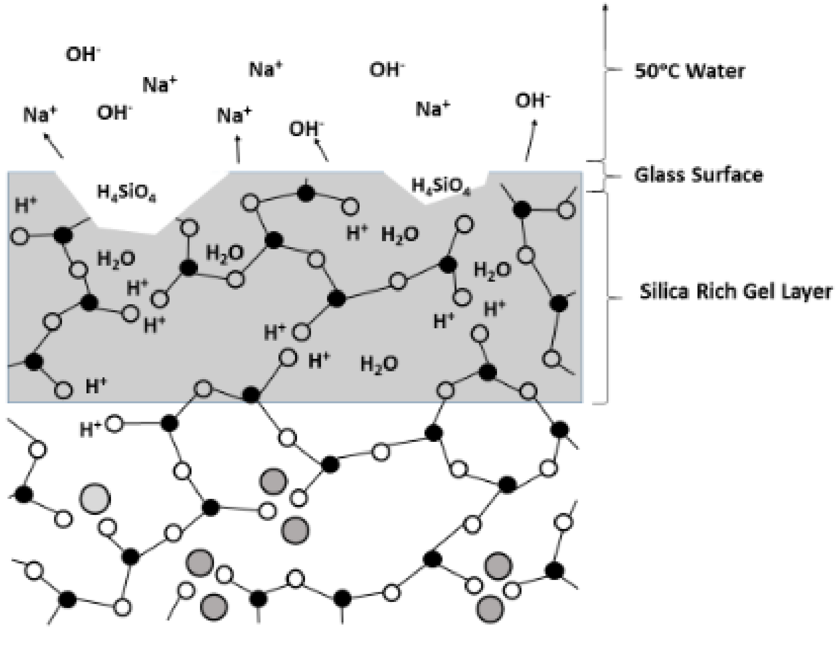

Figure 4.50. Hydrolysis reactions create critical flaws on the glass surface after aging in 50°C water.

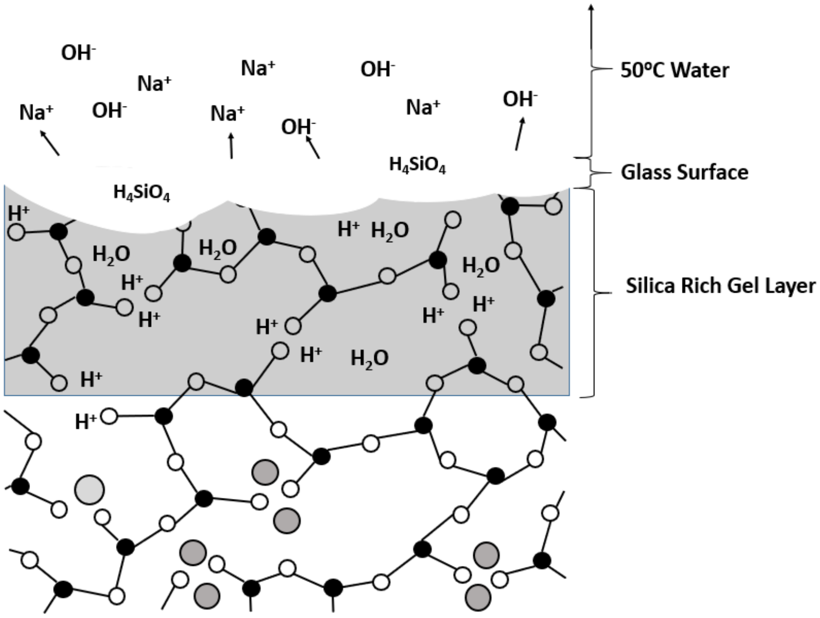

Figure 4.51. Hydrolysis reactions create critical flaws on the glass surface after aging in 50°C.

4.3.3. Increase in Failure Strains of Fibers Weathered in Low Humidity Air.

The SEM images of the surfaces of the OI-A and OI-B fibers weathered in 10%RH/50°C air reveal significantly less degradation compared to fibers weathered in 80%RH/50°C air (e.g., Figure 4.27), although images of the surfaces collected at a higher magnification show surface deposits that are round and submicron in size (Figure 4.28 and Figure 4.29). Dark spots appear have formed after just 8 hours in ambient conditions (Figure 4.31). Similar dark areas surround several of the larger features that form after weathering in both 10%RH/50°C and ~40%RH/50°C air (Figure 4.28, Figure 4.29, and Figure 4.31). These images all show varying sizes and numbers of droplet and particle-like features. Comparable features have been observed on the surfaces of other glasses weathered in similar conditions[111], [141], [144]. Features observed on E-glass fibers weathered in 10%RH/50°C air were believed to be organic particles that were either electrostatically attracted to the surface or organic pollutants diffused into water droplets condensed on the surface [111], [141]. Similar features on soda-lime-silicate glass have been described as “wax-like”[145]. It has been suggested that features start developing within 10 minutes on a freshly formed surface[144]. The features were too small to chemically analyze in the present study. However, other studies have tracked the feature growth and indicate that feature remains “wax-like” after three months in ambient conditions before developing primarily into sodium sulfate and sodium carbonate crystallites after one year[141], [144]. The removal of the crystallites after one year revealed pits associated with their location[71]. The inconsistent growth of these surface features implies that their growth is either influenced by an external uncontrolled factor, such as the deposition of atmospheric particles, or that the individual fibers develop the features differently due to variations in processing conditions. Because the frames with fibers were stacked on racks during the weathering experiments, it is not unreasonable to assume that organic particles could have settled unevenly on the fiber surfaces. The fibers used in the SEM analyses were randomly selected from the storage racks. Alternatively, as is discussed in section 4.3.1, heterogeneities from processing may affect the development of flaws and the flaw distributions. The preferential formation of these weathering products may reveal the relative homogeneity of an individual fiber surface. However, the Weibull moduli for the failure strains remain consistent for OI-B fibers weathered in 80%RH/50°C (Figure 4.2 and Figure 4.4) implying that these heterogeneities do not affect the distribution of failure strains over the weathering period in this study. This is supported by the lack of observable damage on the fiber surface after rinsing with water (Figure 4.30). Figure 4.52 shows the ratio of failure strains measured in ambient conditions to those measured under liquid nitrogen for the fibers weathered in the 10%RH/50°C, 40%RH/50°C, and in ambient environments. The ratios do not change significantly for any of these three sets of samples, remaining consistently between 0.30 and 0.39; this is in sharp contrast to the large increase in this ratio, to 0.45-0.56, for fibers weathered in 80%RH/50°C air (Figure 4.40). The constant ratio indicates that neither flaws nor fatigue become more consequential during the aging period.

The initial short-term (three day) weathering of OI-A and OI-B fibers at 10%RH/50°C, 40%RH/50°C, and ~40%RH/25°C (ambient) environments increases the failure strain measured both in air (Figure 4.11) and in liquid nitrogen (Figure 4.12). In fact, the ratio of the inert failure strain to ambient failure strain does not change with weathering time (Figure 4.51). Additionally, unlike glasses weathered in 80%RH/50°C air, fibers weathered in 10%RH/50°C air did not show a measurable increase in the fatigue parameter over the 30-day weathering period (Figure 4.16), and so it is unlikely that the fatigue mechanism or rate is affected by weathering at these lower levels of humidity. Therefore, it appears that structural changes on the glass surface from exposure to these low humidity conditions are initially impeding crack initiation or propagation. This effect has not been seen for pristine silica or E-glass fibers weathered in similar low humidity conditions [111], [146].

A possible explanation for the increase in failure strains is that surface hydroxylation increases the energy required for crack initiation on the glass surface. Molecular dynamic simulations have shown that water preferentially adsorbs on a silicate glass surface at high energy defects, such as three-coordinated Si and non-bridging oxygen [82]. After adsorption, the defect sites restructure into lower energy sites, thereby decreasing the concentration of defects[82], [147]. Molecular dynamic studies have shown that these reactions occur on soda silicate glass surfaces within the first pico-second after fracture (Figure 4.53). The effect of the surface hydroxylation at longer times has not been studied with molecular dynamics so it is not clear that the defect concentration on the surface continues to decrease after the initial reactions. Additionally, silica has also been shown to undergo similar surface hydroxylation restructuring (Figure 4.53), but it does not exhibit an increase in failure strain [146]. Therefore, the hydroxylation is likely not the primary mechanism for the increase in failure strains.

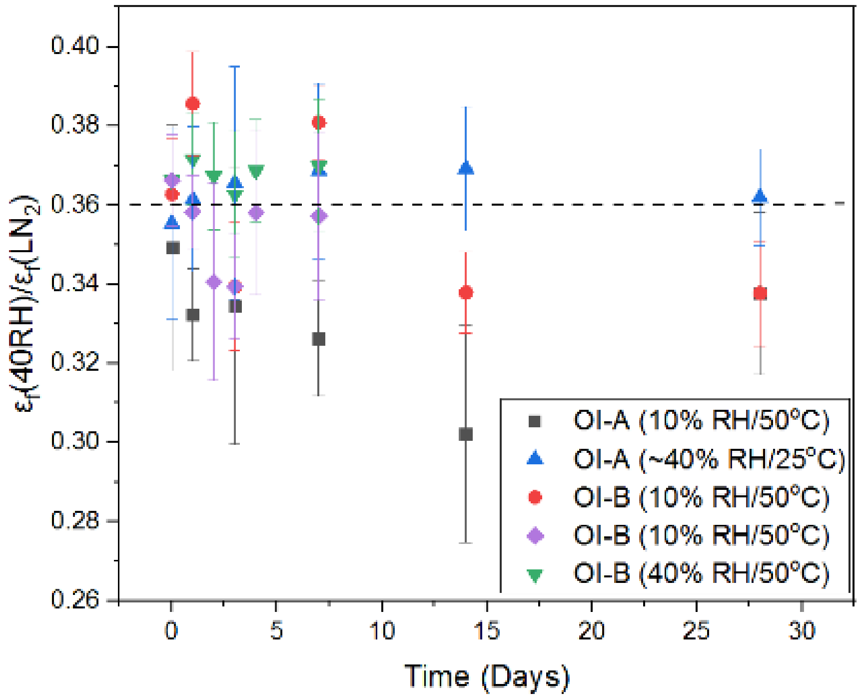

Figure 4.52. Ratio of the average failure strain measured in ambient air (room temperature, 40%RH) to that measured under liquid nitrogen for OI-A and OI-B glasses weathered under the conditions indicated. Line is a guide for the eye.

Another possible explanation for the increase in failure strains after exposure to low humidity air involves the relative kinetics of the ion-exchange and hydrolysis reactions at the SLS surfaces. At lower humidity, hydrolysis and ion-exchange reactions are significantly slowed due to the lower activity of water. Since ion-exchange reactions typically precede hydrolysis reactions during weathering, the leaching of sodium ions is the driving weathering mechanism for a longer period of time whereas in high humidity conditions, the period of time prior to significant network hydrolysis would be much shorter. It is likely that hydration is also occurring during this period. Several studies have shown that the ratio of Na^+ to H^+ during ion-exchange is one to three for soda lime silicate glasses reacted in room temperature water[69], [148]. This indicates that the surface is hydrated simultaneously during the ion-exchange reactions (Equation 4.5). The rate of hydration will increase with ongoing ion-exchange reactions, and thick hydrated silica-rich surface layer with accumulated sodium ions on the surface will eventually form[67]. The surface features on the glass cannot be discounted as inert entities during this initial weathering process. The features are likely the product of dissolved SO_2 and CO_2 in the condensed water reacting with the sodium rich glass surface.

As proposed, the formation of the hydrated, silica-rich layer occurs faster than the hydrolysis reactions. Because the silicate network remains intact during the ion-exchange and hydration, the resulting surface is likely homogenous and uniform and therefore, devoid of structural flaws that can act as stress concentrators. When the silicate network begins to dissolve via hydrolysis reactions, the resulting corrosion front has been shown in this study and in the literature to proceed non-uniformly, creating pitting on the surfaces (Figure 4.46) [71], [144]. These etch pits act as stress concentrators and decrease the failure strains. This explanation would suggest that it is the rate of hydrolysis reactions that drives the growth of flaws and the resulting decrease in SLS glass strength during weathering.

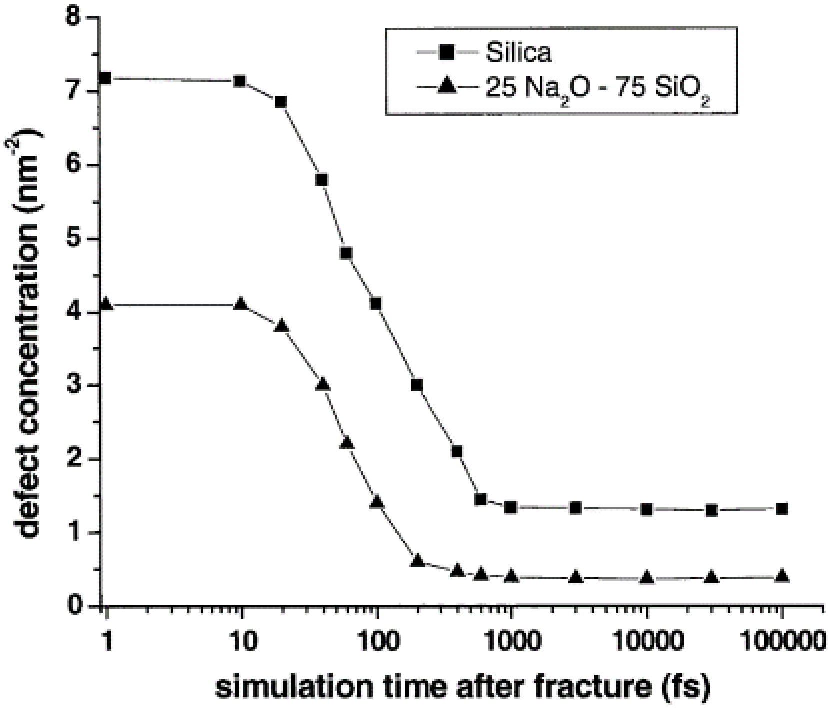

Figure 4.53. Surface defect concentration as a function of simulation time after the instant of fracture[82].

Recent studies of the mechanical properties of SLS glass surface have shown that SLS glasses are surprisingly more resistant to mechanochemical wear in the presence of water compared to most silicate glasses [149].This increased resistance has not been observed in alkali aluminosilicate, silica, borosilicates, or E-glass[150]. Luo et. al. demonstrated that surface sodium ions and subsurface hydrous species both play important roles in tangential shear resistance from mechomechanical wear on a soda lime silicate glass surfaces in humid environments [151]. However, they concluded that further modeling and experimentation is required to understand the roles of these species in the increased shear resistance. To better understand this phenomenon, Luo et.al. hydrothermally treated SLS surfaces in a pressurized, humid conditions to create a highly hydrated sodium depleted surface layer[152]. This hydrated layer was found to have a lower hardness and, a decreased wear resistance; the fracture toughness of the glass surface also increased. Enhanced fracture toughness was also recently observed for a hydrated cesium aluminoborate glass[153]. In this study, the glass was exposed to ambient conditions for 7 days. After 7 days, the fracture toughness of the glass increased from 30N to 490N. Removing the hydrated layer by polishing decreased the fracture toughness back to 30N. The mechanism behind the increased fracture toughness and wear resistance is also not well understood. One theory speculates that the surface is similar to a hydrated silica surface, inferred from the higher fracture toughness and alkali depletion, and therefore, suppresses crack initiation and propagation[152]. Alternatively, a prominent theory is that the topological constraints in the hydrated, alkali-depleted layer decrease due to the increase in OH- groups [152], [154]. This could contribute to the enhancement of glass network “flexibility”[153]. To relate these studies to the increasing failure strain effect observed in the present work requires further experimentation to (1) quantify and verify the surface and subsurface species of SLS glass exposed to 10%RH/50°C air, and (2) understand how the change in mechanical properties of a surface layer several nanometers thick can prevent crack initiation and propagation in tension.

4.3.4. Fatigue Susceptibility of Weathered Surfaces. As noted above, the ratio of failure strains for weathered fibers tested in ambient conditions (40%RH, room temperature air) compared with those tested under liquid nitrogen initially increase with weathering time, before leveling off after several weeks (Figure 4.40). This indicates that the influence of water in the ambient conditions on the failure mechanism is becoming relatively less important than the damage that has been accumulating during weathering. There are corresponding increases in the fatigue parameter for the weathered fibers (Figure 4.15) that are consistent with less influence of atmospheric water on the failure process.

Coated silica fibers have also shown an increase in the fatigue parameter after weathering in 85%RH/85°C conditions for 30 days and ambient conditions for 2 years [95]. The decrease in susceptibility to fatigue in the silica fibers was attributed to either the coating becoming more resistant to OH ion penetration or to the saturation of the silica glass surface with OH ions resisting further corrosion during testing. Similarly, the decrease in fatigue susceptibility (increase in fatigue parameter) of SLS could indicate that the alkali-deficient gel layer or weathering crust is interfering with atmospheric water reaching the critical flaw tips, reducing the fatigue susceptibility. Fibers weathered in water do not form an alkaline weathering crust because corrosion products are transported away from the surface, but they do form a silica-rich reaction layer similar to what forms on fibers weathered in humid conditions[155]. Figure 4.16 shows that the fatigue parameter for 50°C water-aged fibers also increases, indicating a decrease in the susceptibility to fatigue, with increasing weathering time at a similar rate to that measured for fibers weathered in 80%RH/50°C air. This supports the hypothesis that the decrease in fatigue susceptibility is primarily driven by the formation of the silica-rich gel layer on the glass surface and not the formation of the alkaline weathering products. Figure 4.54. shows a diagram of a critical flaw encased in the alkali deficient silica rich 'gel' layer on a weathered soda lime silicate glass surface. The critical flaw acts as the stress concentrator that decreases the failure strain. However, the silica 'gel' interferes with atmospheric water interactions with the glass, reducing the fatigue susceptibility.

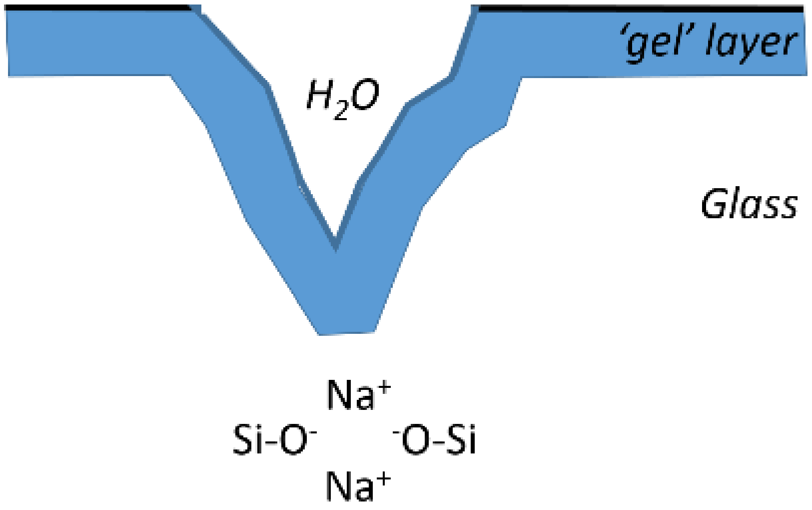

Figure 4.54. Diagram of a critical flaw encased in the alkali deficient silica rich 'gel' on a weathered soda lime silicate glass surface.

The average fatigue parameter of SLS fibers weathered for 30 days in 80%RH/50°C air is similar to the fatigue parameter of silica and E-glass, reported to be in the range 20-30[44], when measured in ambient conditions. Differences between SLS, silica, and E-glass surfaces include silica and E-glass surfaces being less reactive with water [43] and that the primary fatigue mechanism is hydrolysis not ion-exchange[44]. If the SLS glass surface is becoming less reactive to water, it could be due to the alkali-deficient gel layer being fully water “saturated” resulting in additional water in the atmosphere having less influence on the crack growth. However, if water saturation was the only cause of the decrease in fatigue susceptibility, the fatigue parameter should remain independent of testing humidity. Figure 4.16 shows that SLS fibers weathered in 80%RH/50°C air for seven days are more sensitive to the relative humidity of the testing environment. As previously discussed by Tang et. al.[42], the fatigue parameter for pristine SLS glass is independent of humidity above 1%RH, and that finding was confirmed here (Figure 3.11). However, the fatigue susceptibility of both E-glass and silica are dependent on humidity because for these glasses, the fatigue is driven by the slower Si-O hydrolysis reactions[42]. Therefore, it is also possible that the decrease in fatigue susceptibility of SLS could indicate that the alkali-deficient gel layer is resisting further ion-exchange reactions.

$$-\underset{|}{\overset{|}{Si}} \quad -ONa^{+} + H_3O^{+} \rightarrow -\underset{|}{\overset{|}{Si}} \quad -OH(H_2O) + Na^{+} \tag{4.7}$$

$$-\underset{|}{\overset{|}{Si}} \quad -ONa^{+} + H_2O \rightarrow -\underset{|}{\overset{|}{Si}} \quad -OH + Na^{+} + OH^{-} \tag{4.8}$$

$$- \quad \underset{|}{\overset{|}{Si}} \; - \quad O \quad -\underset{|}{\overset{|}{Si}} \quad - + H_2O \rightarrow 2\left[- \quad \underset{|}{\overset{|}{Si}} - OH\right] \tag{4.9}$$

Secondary ion mass spectroscopy and nuclear magnetic resonance studies of the leached layers that form on SLS glasses indicate that the surfaces become increasingly similar to fused silica with reaction times[48]. A shift in the dependence of fatigue from ion exchange reactions to the hydrolysis of Si-O bonds in the silica-like layer may be occurring. This fatigue mechanism shift would result in an increase in the fatigue parameter because the Si-O hydrolysis reactions are slower than the ion-exchange reactions[67]. This supports the hypothesis that the formation of "silica-like" surfaces on weathered SLS fibers determine their fatigue behavior.

Another way to describe the change in fatigue mechanism is to take into account the reaction order. The order of a reaction describes the dependence of reaction rate on the reactant concentration. A reaction order of 1 indicates that the reaction is dependent on the concentration of a singular species. Higher reaction orders indicate that the reaction is dependent on more than one species or the square of the concentration of a single species. Duncan et. al. defined the empirical dependence of failure strains obtained in the two-point test on the relative humidity[64]:

$$\varepsilon_f \propto (RH)^a \tag{4.10}$$

The reaction order, m, could then be determined from the fatigue parameter by[64]:

$$m = a \times (1 - n) \tag{4.11}$$

where a is derived from the dependence of failure strains on the humidity and the fatigue parameter ‘n’ is considered to be a constant derived from the average value over the humidity range. Figure 4.55 shows the humidity dependence of failure strain for glass fibers weathered in 50°C water for up to seven days and measured in room temperature air at the indicated RH value. ‘a’ can be determined from the linear slope of the data in Figure 4.55. At lower humidity, Wiederhorn observed that the reaction order for soda-lime-silicate decreases from 1 to 0.5. He attributed this to the presence of more than one fatigue reaction occurring at low humidity[54]. Table 4.2 shows that the reaction order, calculated from Equation 4.11 and the ‘a’ values determined from Figure 4.55, increased from 1.3±0.1 to 2.3±0.4 over the weathering period. The reaction order of the pristine glass is comparable to values reported for SLS[42], [54]. The reaction order is near 1 for pristine SLS glasses because at low values of humidity, only one water molecule is available to break a bond [42]. However, at higher humidity:

$$-\underset{|}{\overset{|}{Si}}\ -ONa^+ + 2H_2O \rightarrow -\underset{|}{\overset{|}{Si}}\ -OH\ (H_2O) + Na^+ + OH^- \tag{4.12}$$

In this scenario, two water molecules are available to break bonds. For hydrolysis reactions, Armstrong et. al. surmised that if the reaction with water in Equation 4.9 is second order, then the first order is with OH^- [55]. Tang et. al. attributed the lower reaction order of SLS glasses in humid conditions to the acceleration of corrosion from the local increase in pH from the production of OH^- in the ion exchange reactions[42]. As the glass ages, the production of OH^- decreases because of the sodium depleted layer slowing the fatigue reaction on the weathered surface.

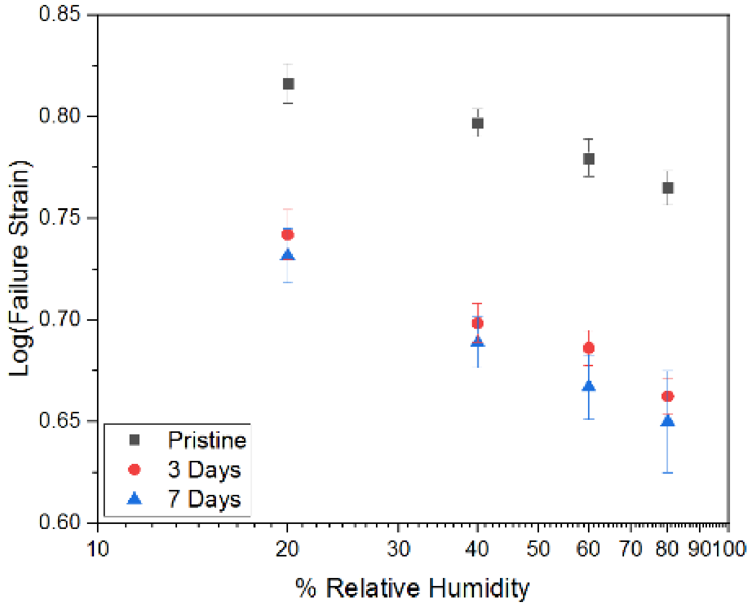

Figure 4.55. Humidity dependence of failure strains for OI-B glass fibers aged in 50°C water for up to seven days and measured in room temperature air at the indicated RH value.

Table 4.2 Reaction order values for fibers OI-B glass aged in 50°C water for up to 7 days, from the data in Figure 4.55.

	m
Pristine	1.3 ± 0.1
Aged 3 Days	2.1 ± 0.3
Aged 7 Days	2.3 ± 0.4

4.3.5. Dependence on Residual Water Content in Soda Lime Silicate Glass. It has been well documented that the concentration of water between 100-500ppm can have significant effects the properties of the glass[118], [130], [131], [156]. Therefore, the effect of water content on the fatigue and weathering characteristics is of interest. Section 4.3.2 to section 4.3.4 discuss the role of water in surface reactions during weathering and stress corrosion. Figure 4.10 and Figure 4.14 show the effect of residual water content on the inert failure strain of glass fibers weathered in 80%RH/50°C air and 10%RH/50°C air, respectively. Glasses with higher and lower water contents see the same rapid decrease in ambient and inert failure strains after exposure to 80%RH/50°C air for 28 days (Figure 4.9 and Figure 4.10). In inert conditions, the water content does not appear to have any effect on the failure strains despite the 270ppm glass having lower pristine failure strengths (Figure 3.13) compared to the 140ppm and 180ppm glass. This indicates that the rate of flaw growth via weathering reactions is independent of residual water concentration below 300ppm.

The fibers weathered in 10%RH/50°C air do not show a difference or a trend in failure strains measured in ambient conditions. However, the failure strains of the fibers measured in ambient conditions after weathering in 80%RH/50°C air show that the 270ppm fibers have a 5% greater decrease in failure strains compared to the 140ppm and 180ppm fibers. Figure 4.56 shows the ratios of the ambient and inert failure strains. There are similar increases among all three glasses over the 28-day weathering period in 80%RH/50°C air and 10%RH/50°C air. All three glasses have a similar ratio after 28 days of weathering, which means that the effect of fatigue and flaws is independent of water concentration.

The fatigue parameter is possibly greater for the 270ppm glass that the 140ppm and 180ppm, which mean the susceptibility to fatigue is lower for the 270ppm glass

(Figure 4.17). If this trend is real, this is in direct contradiction with other studies that found that susceptibility to fatigue increases with increasing residual water content in sodium silicate glasses[129], [130]. Ultimately, the bulk water content of the glass in the 100-300ppm range likely does not affect the weathering and fatigue characteristics of SLS in a meaningful way.

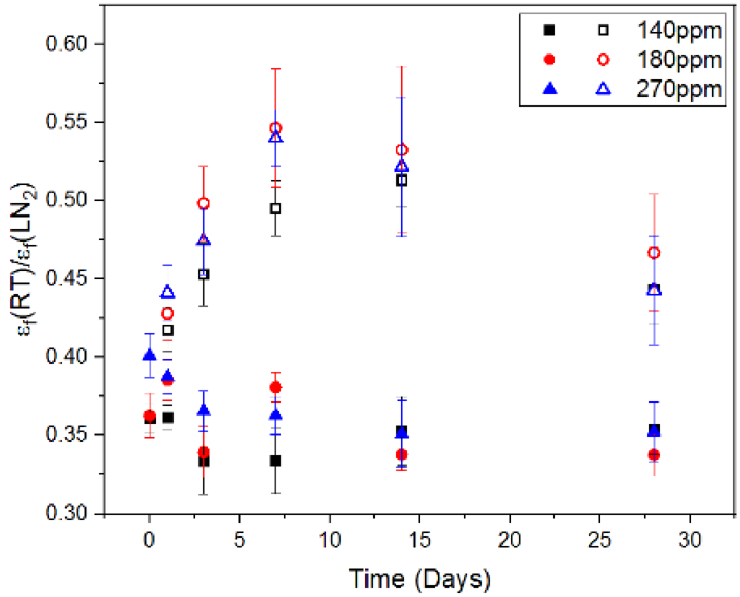

Figure 4.56. Ratio of the average failure strain measured in room temperature air at 40%RH to those measured in liquid nitrogen for OI-B glasses with different water contents weathered in 80%RH/50°C air. Open symbols represent fibers weathered in 80%RH/50°C conditions and closed symbols represent fiber weathered in 10%RH/50°C conditions.

5. SUMMARY AND AFTERWORDS

Understanding the mechanistic sources of failure in pristine and weathered soda lime silicate glass has been of great interest to the commercial glass industry. This section summarizes the insights to the failure of pristine and weathered soda lime silicate glasses from this work, and suggestions for future work are included.

The two-point bend method has been shown to provide reproducible failure strains that are consistent with values reported in the literature. This method was able to distinguish subtle differences in failure behavior between commercial soda lime silicate glasses with the same nominal composition, but that were processed in the same facility years apart. The sensitivity of the TPB method was also able to show that the fatigue and failure characteristics did not meaningfully change for pristine and weathered soda lime silicate glasses with water contents between 140ppm and 270ppm.

The effect of processing on the development of critical flaws during weathering was also observed. When fibers were drawn with different techniques, although the pristine failure strains had similar narrow distributions, the weathered fibers were shown to have either narrow or broad failure strains depending on fiber drawing technique. The broad failure strains were attributed to preferential or increased flaw growth at structural inhomogeneities caused by the processing technique. This is an interesting insight that although pristine properties of glass are similar, weathering may reveal processing effects that would have otherwise gone unnoticed. It may be possible to evaluate the homogeneity of a glass at a higher resolution by weathering the glass first.

This study produced several insights into the fatigue and failure behavior of SLS weathered in 80%RH/50°C condition. AFM characterization of pristine fiber surfaces revealed topological features that were the same size as the predicted critical flaw size derived from the failure strains. After weathering the samples in 80%RH/50°C air, surface analysis of reaction products and weathering damage indicated that expected weathering reactions were occurring. It was also determined that fibers weathered in 80%RH/50^{o}C have very different failure and surface characteristics after weathering compared to fibers aged in 50^{o}C water. This was attributed to differences in the critical flaw development and topological differences between the two conditions. It would be interesting in future experiments to control the reaction layer depth by aging fibers in a controlled pH solution before TPB testing. This would eliminate the uncertainty in the reaction layer thickness and, therefore, make a more reliable comparison to the predicted flaw sizes. Etching the aged fiber surfaces and evaluating the etched surface roughness with AFM may help reveal underlying topography of the damage layer in order to better understand the nature and true size of the critical flaws relative to the reaction layer thickness.

The fatigue susceptibility of soda lime silicate glass was shown to increase over the weathering period in 80%RH/50°C. This increase was attributed to the formation of a silica rich ‘gel’ layer on the surface of the glass. The ‘gel’ layer could act as a water saturated barrier decreasing the effect of fatigue during testing. Alternatively, the alkali depletion in the silica rich ‘gel’ layer results in a change in fatigue reaction. The increased dependence of the fatigue parameter on testing humidity indicated that the latter is more likely.

Probably the most intriguing observation in this study is that failure strains of fibers aged in ambient and 10%RH/50°C conditions increase over the first 3 days of aging. This revelation adds insight to the ongoing discussions in the literature about the unique chemomechanical behavior of soda lime silicate glass in humid conditions. It was surmised that the hydrated, alkali-deficient layer that forms on the fiber surface either has a greater fracture toughness that suppresses crack initiation and propagation or that the OH- groups in the hydrated layer decrease the topological constraints on the surface of the glass resulting in an increased “flexibility” of the glass structure. This work did not attempt to quantify the mechanical properties of this reaction layer. Therefore, it would be worthwhile to gather information on the hardness and elastic modulus of the reaction layer using nanoindentation. Additionally, it would be important to study the increasing failure strain effect over a wider range of temperatures and humidities. Fibers aged in 80%RH/50°C do not show any increase in failure strain while preliminary data (Appendix D) shows an astounding 25-30% increase in inert failure strain for fibers aged in 18%RH/50°C, which indicates that the magnitude of the increasing failure strain effect is sensitive to the weathering humidity. In conjunction to experiments, molecular dynamic (MD) studies on the kinetics of the interaction of water with sodium-leached sites and the subsequent distortion of the hydrated, alkali depleted silicate network would be of interest. Additionally, MD studies of an alkali-depleted, hydrated layer could give insight into energy dissipation mechanism under tension of this layer compared to pristine surfaces.

APPENDIX A.

FAILURE AND FATIGUE OF EMERALD AND FLINT SODA LIME SILICATE GLASS

OVERVIEW

Flint and Emerald soda-lime silicate glass bottles were provided by Owen-Illinois, Inc. The bottles were re-melted in a platinum crucible at 1450°C in air for four hours to produce a well-conditioned, bubble-free melts. The well-conditioned, bubble-free emerald and flint melts were transferred into the box furnace and left for four hours at 1220°C and 1175°C, respectively, the 1000 P isokom temperature reported by Tang[44]. The melts were then cooled to the fiber-pulling temperature of 1135°C. Fibers were produced using the method described in section 2.2. The failure strains and fatigue parameters were then determined using the two-point bend method according to the method in section 2.4.

RESULTS

Figure A.1.-A.3. shows the distributions of failure strains recorded for pristine flint and emerald glass fibers measured in room temperature air at different values of relative humidity and faceplate velocities. The emerald glass fibers have consistently greater failure strains than the pristine flint fibers. Figure A.4. shows the fatigue parameter for the emerald and flint glasses at different values of humidity. These values are summarized in Table A.1.

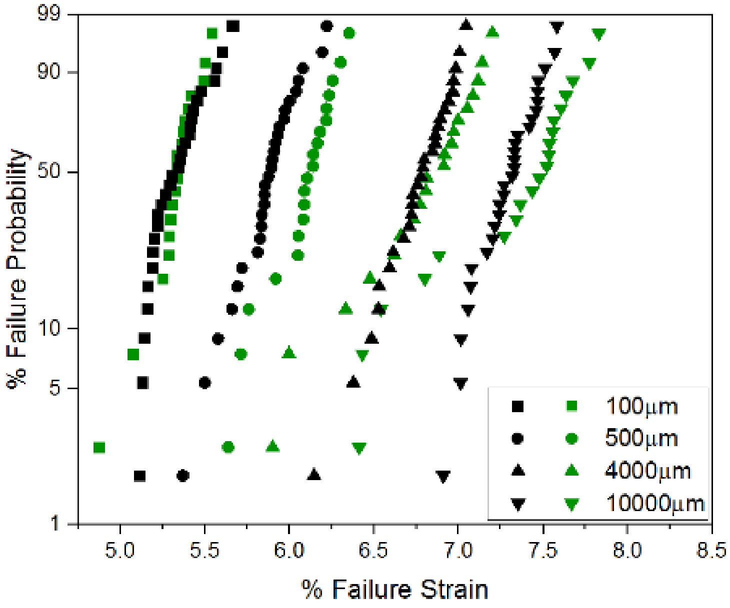

Figure A.1. Failure strain distributions of flint (black symbols) and emerald (green symbols) tested in 20%RH at faceplate velocities between 100-10,000μm/s.

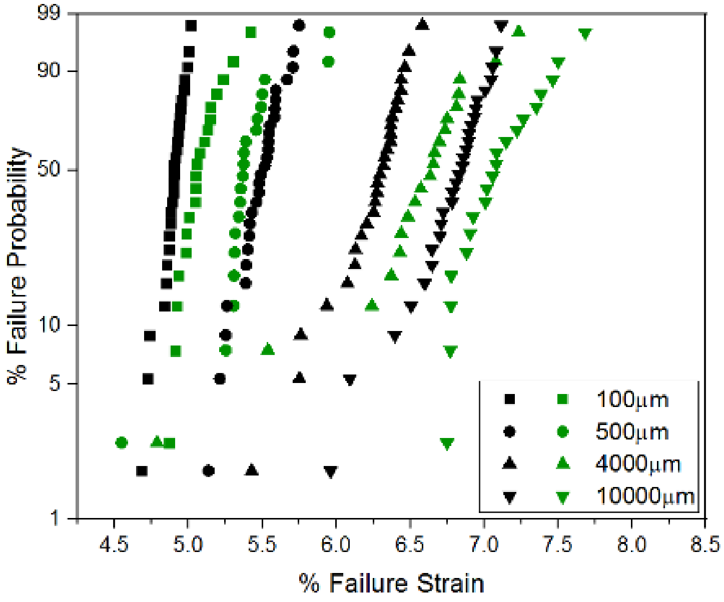

Figure A.2. Failure strain distributions of flint (black symbols) and emerald (green symbols) tested in 40%RH at faceplate velocities between 100-10,000μm/s.

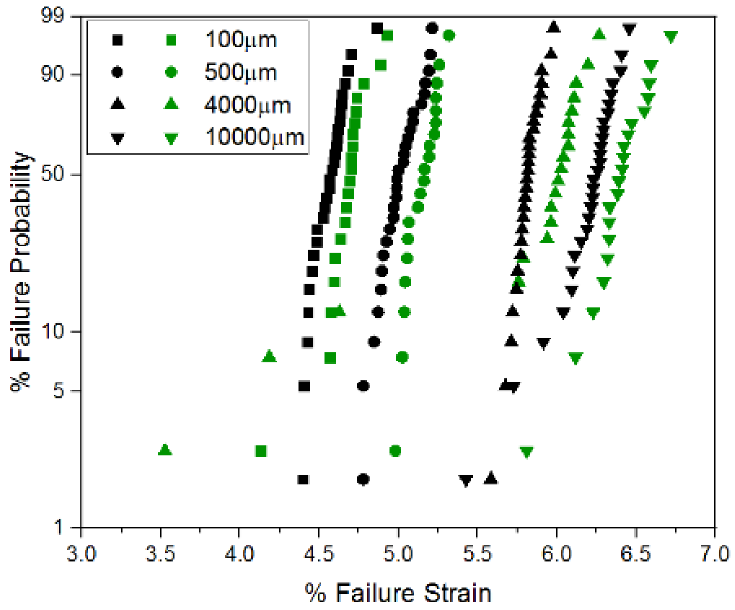

Figure A.3. Failure strain distributions of flint (black symbols) and emerald (green symbols) tested in 60%RH at faceplate velocities between 100-10,000μm/s.

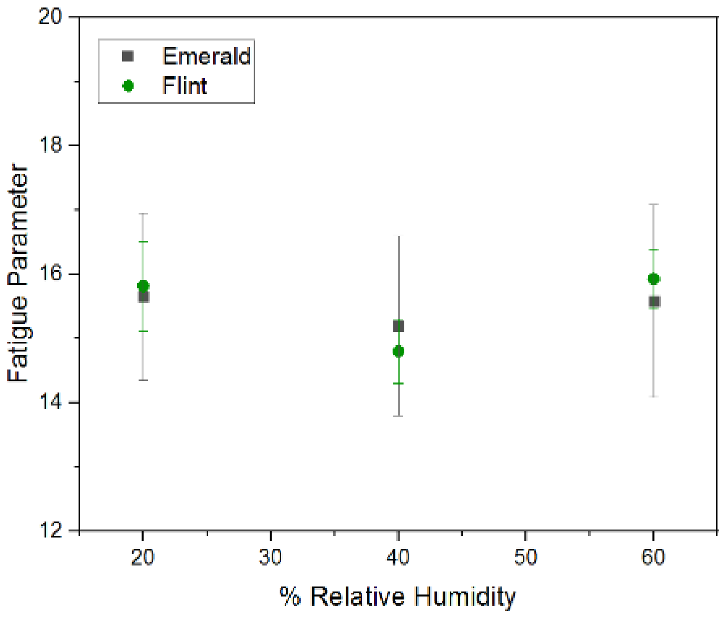

Figure A.4. Fatigue parameter for emerald and flint glass fibers tested in room temperature air with different levels of relative humidity.

Table A.1. Failure strain (ε_f) measured at different faceplate velocities (v_{fp}) in air at 25°C and the corresponding fatigue parameter (*n*) for emerald and flint soda lime silicate glass.

	ε_f (%) in 25°C humid air				*n*
v_{fp} (µm/s) =	100	500	4000	10000	
Flint (RH 20%)	5.33±0.15	5.87±0.15	6.75±0.21	7.29±0.18	15.7±1.3
Flint (RH 40%)	4.9±0.09	5.49±0.15	6.24±0.25	6.78±0.27	15.2±1.4
Flint (RH 60%)	4.56±0.11	5.01±0.12	5.81±0.08	6.19±0.21	15.6±1.5
Emerald (RH 20%)	5.33±0.15	6.09±0.19	6.78±0.35	7.31±0.44	15.8±0.7
Emerald (RH 40%)	5.01±0.13	5.40±0.27	6.52±0.53	7.10±0.27	14.8±0.5
Emerald (RH 60%)	4.67±16	5.15±0.10	5.74±0.73	6.39±0.30	15.9±0.5

Table A.2. Weibull moduli for failure distributions of emerald and flint glass fibers measured at different faceplate velocities (v_{fp}) in air at 25°C.

	Weibull Modulus in 25°C humid air			
v_{fp} (µm/s) =	100	500	4000	10000
Flint (RH 20%)	40.3	38.0	39.9	49.8
Flint (RH 40%)	75.6	45.0	28.8	29.4
Flint (RH 60%)	50.1	49.4	85.3	33.2
Emerald (RH 20%)	42.1	37.7	22.2	18.9
Emerald (RH 40%)	43.3	20.6	12.8	30.4
Emerald (RH 60%)	32.7	64.0	7.1	38.9

APPENDIX B.

EFFECT OF CYCLIC WEATHERING CONDITIONS ON FATIGUE AND FAILURE OF SODA LIME SILICATE GLASS

OVERVIEW

Soda-lime silicate OI-A glass bottles provide by Owen-Illinois, Inc. were used in this study. The fibers were produced from the glass bottle according to the method section 2.2.

Pristine fibers were exposed to either static weathering conditions at 80%RH/50°C or cyclic weathering conditions were fibers were rotated between 80%RH/50°C and 10%RH/50°C conditions every 12 hours. Fibers were weathered for 60 days. Failure strains were determined with the two-point bend mechanism periodically over the 60 days weathering period. Scanning electron microscopy was used to examine the surfaces over the weathering period using the method described in section 2.6.

RESULTS

Previous results from weathering of OI-A SLS fibers in 80%RH/50°C are shown in Figure 4.1 and Figure 4.3 in section 4.2.1. Figure B.1. and Figure B.2. show the average failure strains after weathering in cyclic and static conditions over 60 days. There is a similar rapid decrease in failure strain over the first 14 days for both cyclic and static weathering conditions compared to Figure 4.1 and Figure 4.3. However, the failure strains in Figure B.1. and Figure B.2. after 30 days are much greater than those shown in Figure 4.1 and Figure 4.3. This data was completely anomalous to every other weathering experiment in 80%RH/50°C air. Unfortunately, the source of this variation in degradation is not known but may be due to a faulty relative humidity sensor. Since the rate of degradation of the statically weathered fibers falls somewhere between the 40%/25°C and

80%RH/50°C trends, it is assumed that high humidity chamber was at or above ambient humidity (40%RH) for the experiment.

Figure B.1 and Figure B.2. show average failure strains of fibers weathered statically and cyclically and tested in in 40%RH room temperature air and in liquid nitrogen, respectively. The x-axis in these figures is adjusted to cumulative exposure time to 80%RH/50°C since it has been shown in section 4 that exposure to 10%RH/50°C has a negligible effect on the failure strain compared to exposure at 80%RH. For both cyclic and static conditions, the fiber failures strains decrease with increasing weathering time. For the first 30days, the cyclic and static weathered fibers agree very well with each other. However, at day 60 the fibers appear to diverge considerable. Figure B.3. shows the failure distributions for both conditions at Day 60. Figure B.4. shows that the fatigue parameter increases for both cyclically and statically weathered fibers.

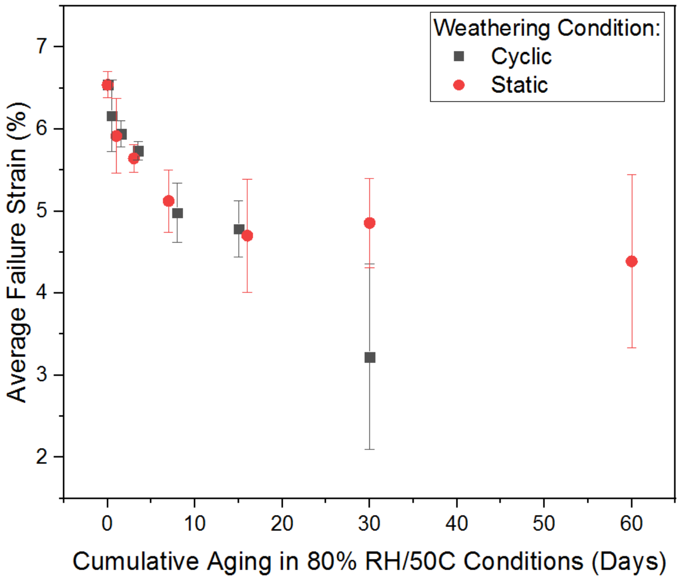

Figure B.1. Average failure strains of cyclically and statically weathered fibers tested in 40%RH room temperature air with a faceplate velocity of 4000μm/s.

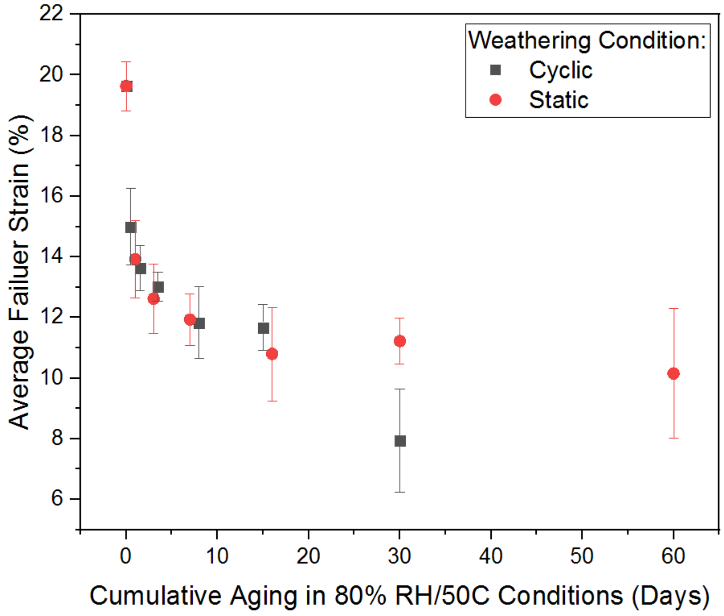

Figure B.2. Average failure strain distribution of cyclically and statically weathered fibers tested in liquid nitrogen with a faceplate velocity of 4000μm/s.

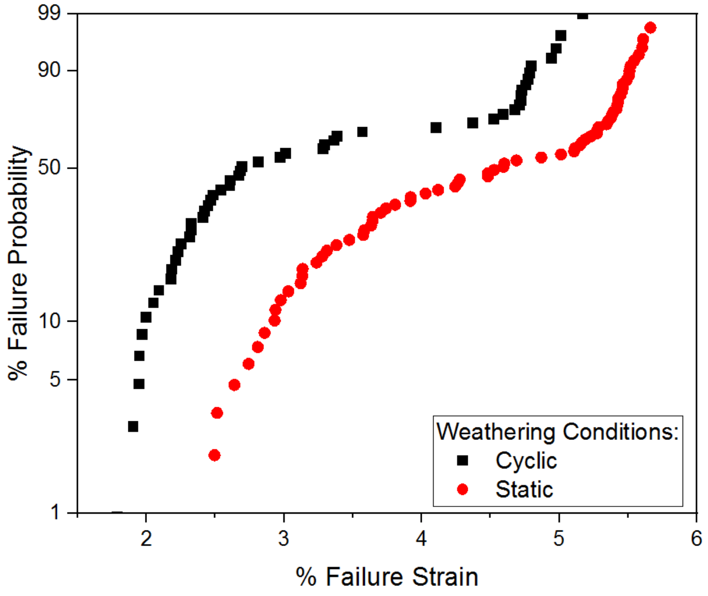

Figure B.3. Failure strain distributions of statically and cyclically weathered fibers after 60 days of weathering, tested in 40%RH room temperature air with a faceplate velocity of 4000μm/s.

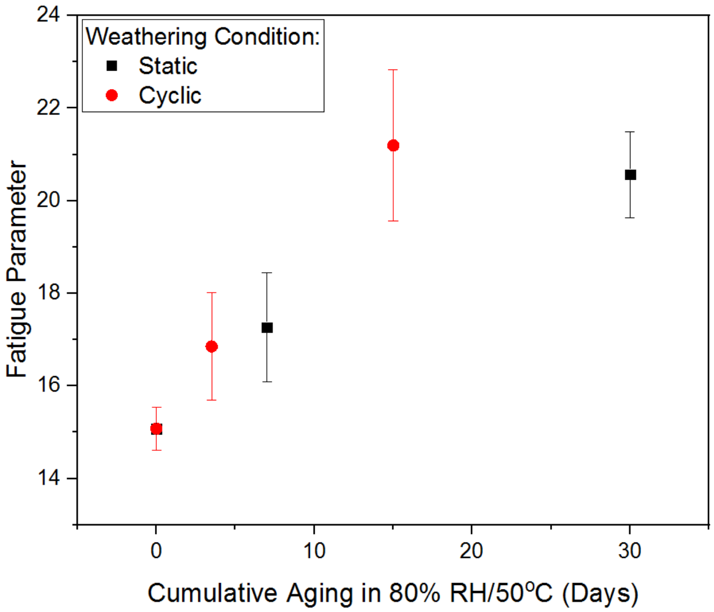

Figure B.4. Fatigue parameters measured at 40%RH/25°C with a faceplate velocity of 4000µm/s of fibers weathered in cyclic and static conditions for up to 30 days.

Electron micrographs of the surfaces of these statically and cyclically weathered fibers over the first 30 days of weathering are shown in Figure B.5. Initially, the surfaces appear similar, but the appearances diverge around day16 when visually the surface features for cyclically weathered samples appear to be smaller and more evenly dispersed than those on the statically weathered surfaces. This is confirmed by looking at the average distribution of features and the average longest width of features show in Figure B.6. and Figure B.7., respectively. Features on the cyclically weathered surfaces are on average 11.6±4.2µm in size and 36.1±12.4 features per 10,000µm^2, whereas the statically weathered features are 34.5±7.6µm and 3.8±2.6 features per 10,000µm^2 after 30 days of weathering.

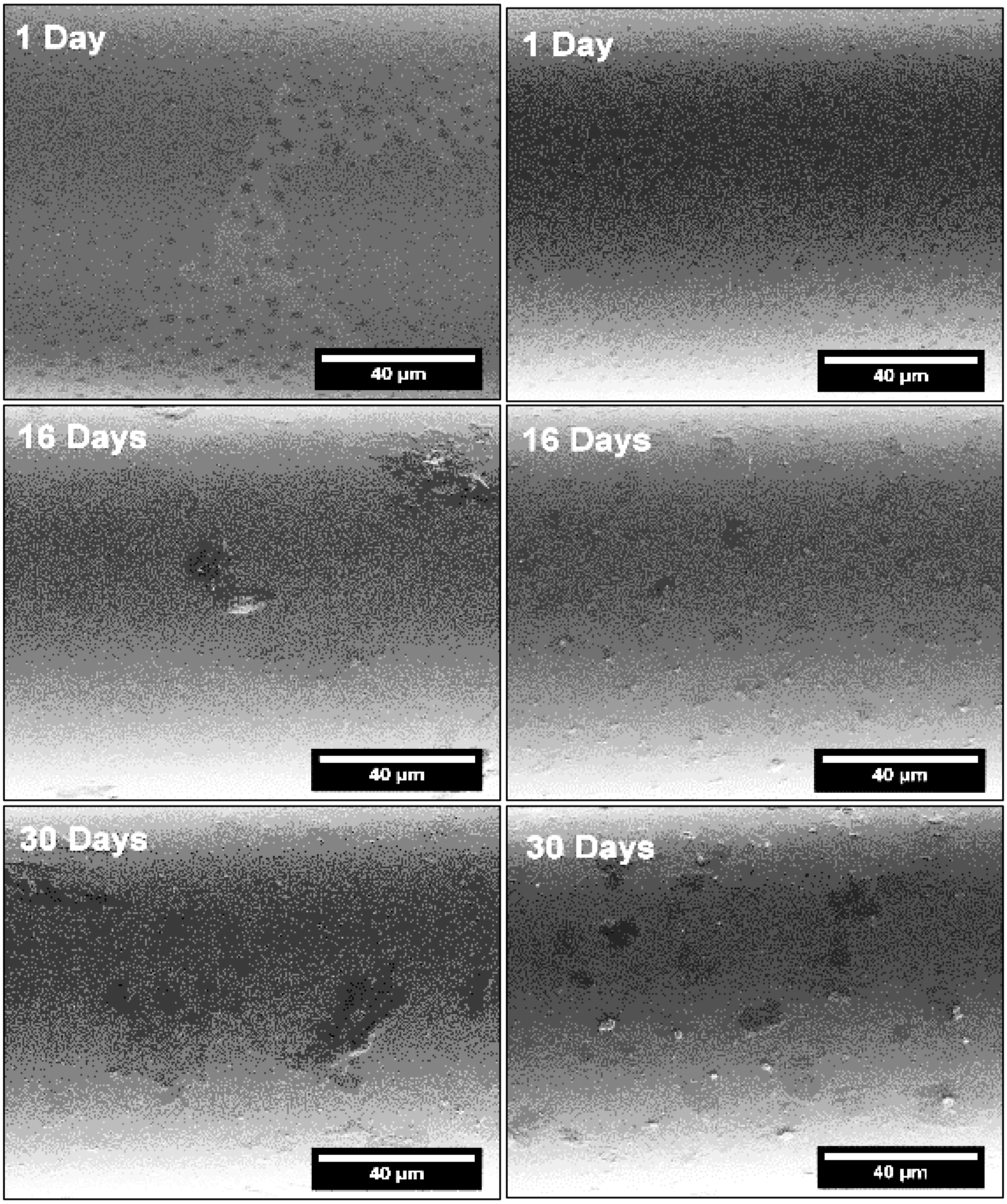

Figure B.5. SEM image comparison of statically (left) and cyclically (right) weathered fibers.

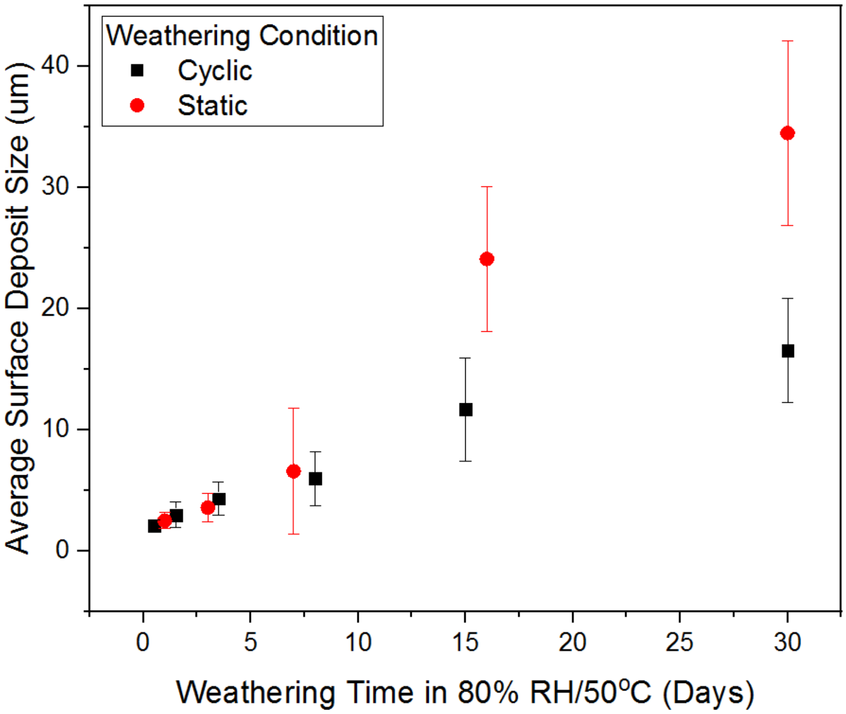

Figure B.6. Average surface deposit size of statically and cyclically weathered fibers.

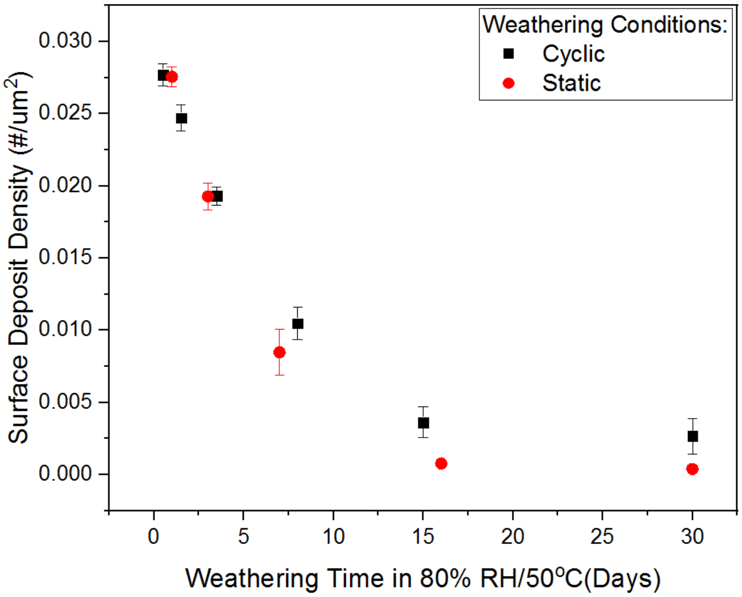

Figure B.7. Surface deposit density of cyclically and statically weathered fibers.

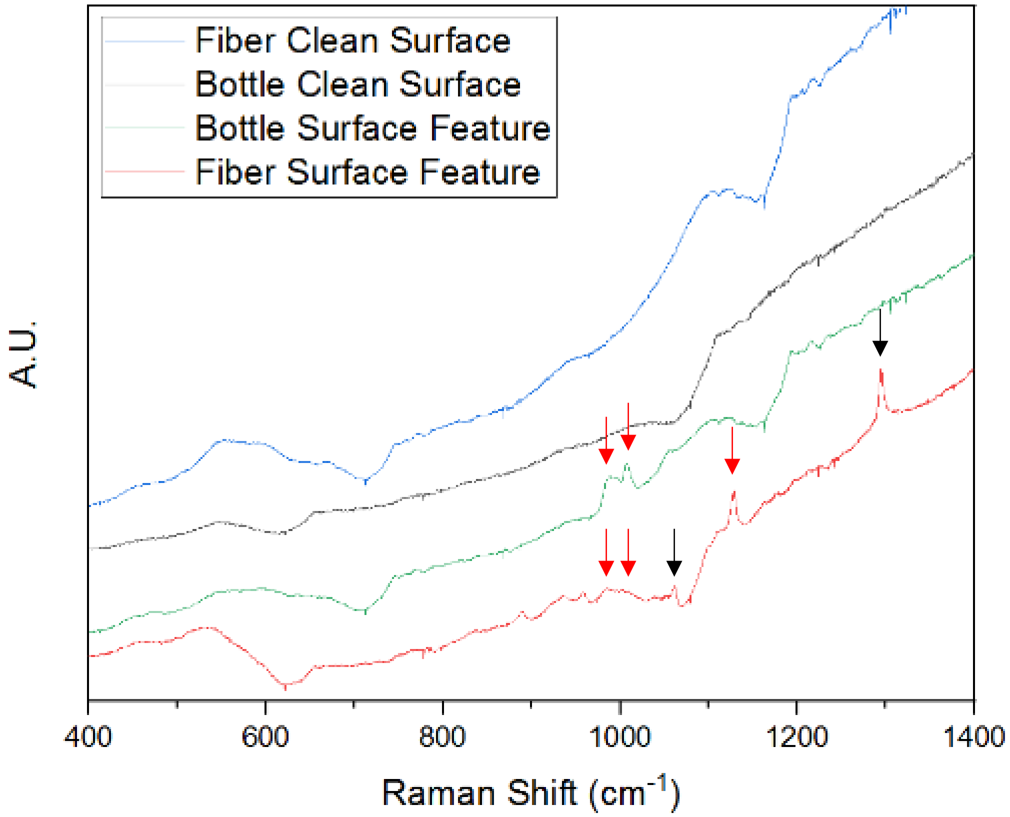

Figure B.8. Raman spectra of OI-A glass fiber surface features after weathering for 100 days in an 80%RH/50C environment. Red and black arrows indicated bands associated with sodium sulfate and sodium sesquicarbonate, respectively.

APPENDIX C.

OPTICAL MICROSCOPY IMAGES OF WEATHERED EMERALD AND FLINT SODA LIME SILICATE GLASS

OVERVIEW

Flint and Emerald soda-lime silicate glass bottles were provided by Owen-Illinois, Inc. It is unknown when the bottles were manufactured. The bottles were carefully scored and broken to avoid creating glass fragments or disturbing the inner surfaces of the bottles. The final pieces were approximately 2 cm x 2cm. These pieces were placed in a humidity chamber at 80%RH/50^{o}C with the inner surface facing up. The pieces were weathered for up to 60 days and periodically examined with an optical microscope (Hirox KH-8700 Digital Microscope) over the weathering period.

Additionally, some pieces of the flint bottle were re-melted in a platinum crucible at 1450°C in air for four hours to produce a well-conditioned, bubble-free melt. Fibers were drawn from the melt according to the method in section 2.2. The pristine fibers were placed in a humidity chamber at 80%RH/50^{o}C and periodically examined with an optical microscope over a period of 300 days.

RESULTS

Figure C.1. and Figure C.2. show the inner surfaces of the emerald and flint glass pieces, respectively, after weathering in 80%RH/50^{o}C conditions for 60 days. The as received surface of the flint bottle has more surface features than the inner surface of the as received emerald bottle. The flint surface has larger circular features roughly 10 microns in size surrounded by submicron black dots. The emerald surface also has submicron black dots, but instead of circular features, there are needle shaped features approximately 1 micron in size. Features on both the emerald and flint bottle surfaces grow over the weathering period. However, the emerald glass features are less than 20 micron long needle shaped after 60 days while the flint glass features are larger (>20 microns) and irregular shaped instead of circular.

Figure C.3. and Figure C.4. show the flint fiber surfaces throughout the 300 days weathering period in 80%RH/50°C air. Features grow over the weathering period and are >90 microns in length after 29 days. The shape of the features is circular after one day but become irregular shaped after 8 days. At 35, 100, and 300 days, the features progressively evolve into needle like features that are similar to those observed on the emerald inner bottle surface after weathering for 60 days in the same conditions.

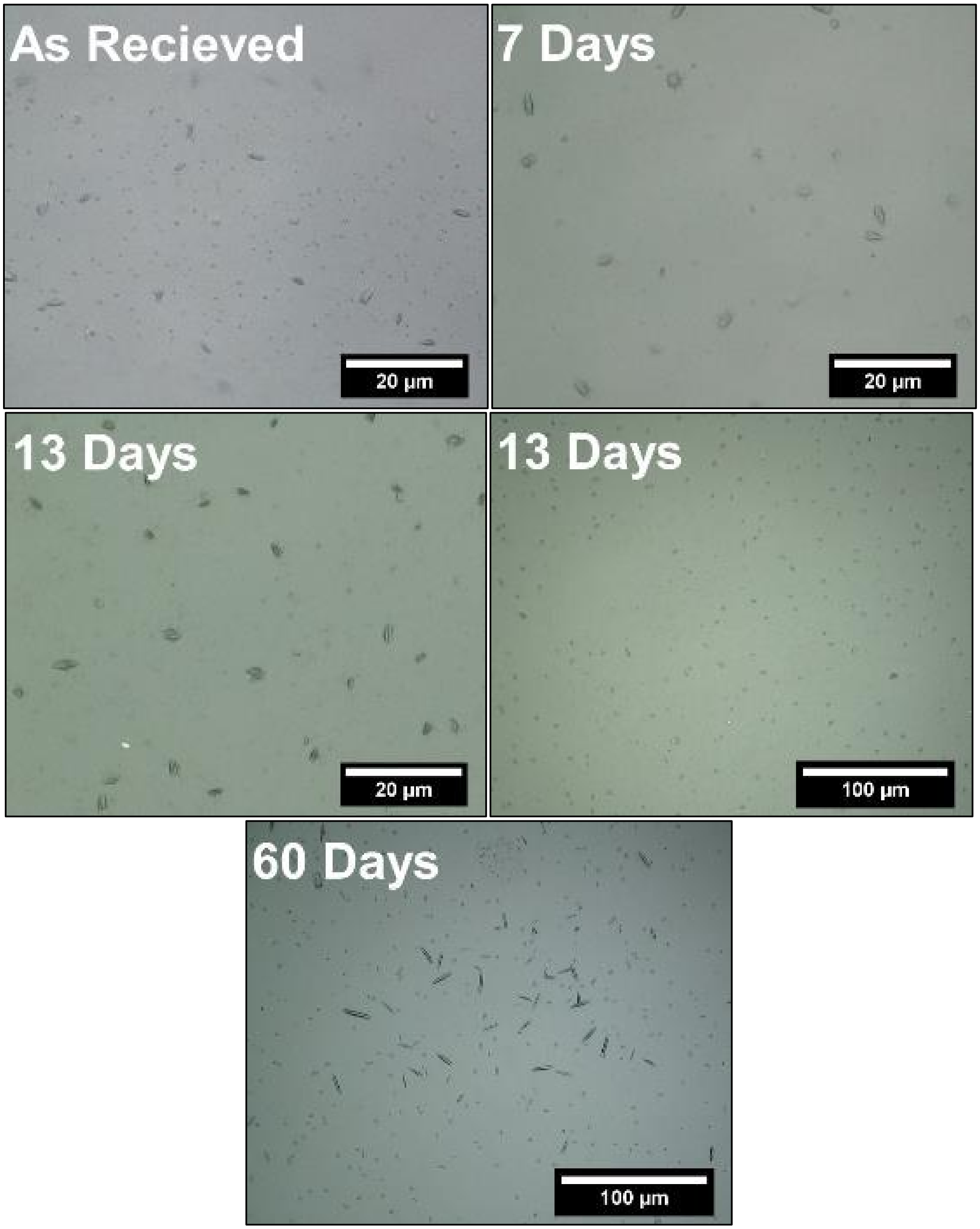

Figure C.1. Inner surfaces of emerald glass bottle as received and after weathering in 80%RH/50°C air for 60 days.

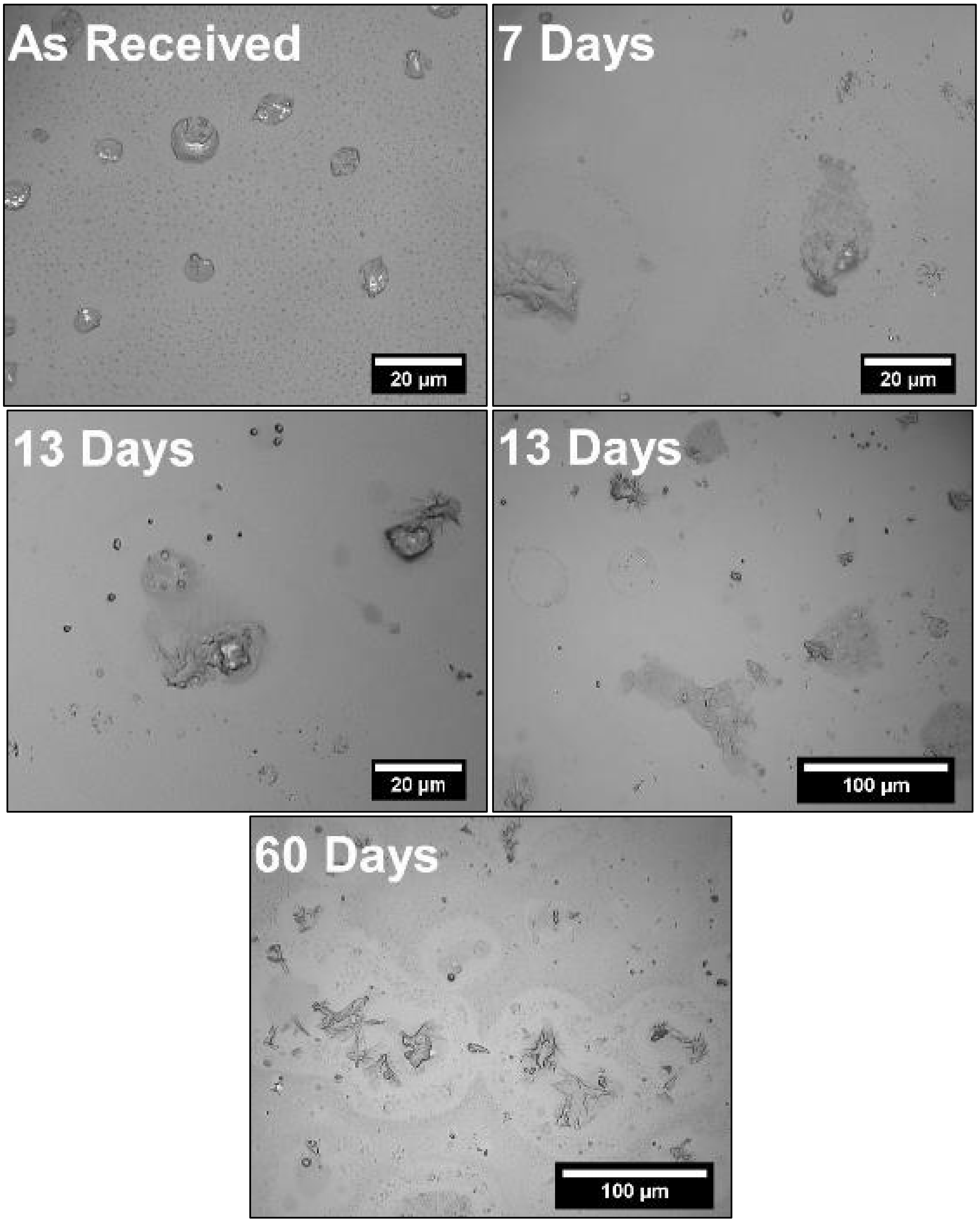

Figure C.1. Inner surfaces of flint glass bottle as received and after weathering in 80%RH/50°C air for 60 days.

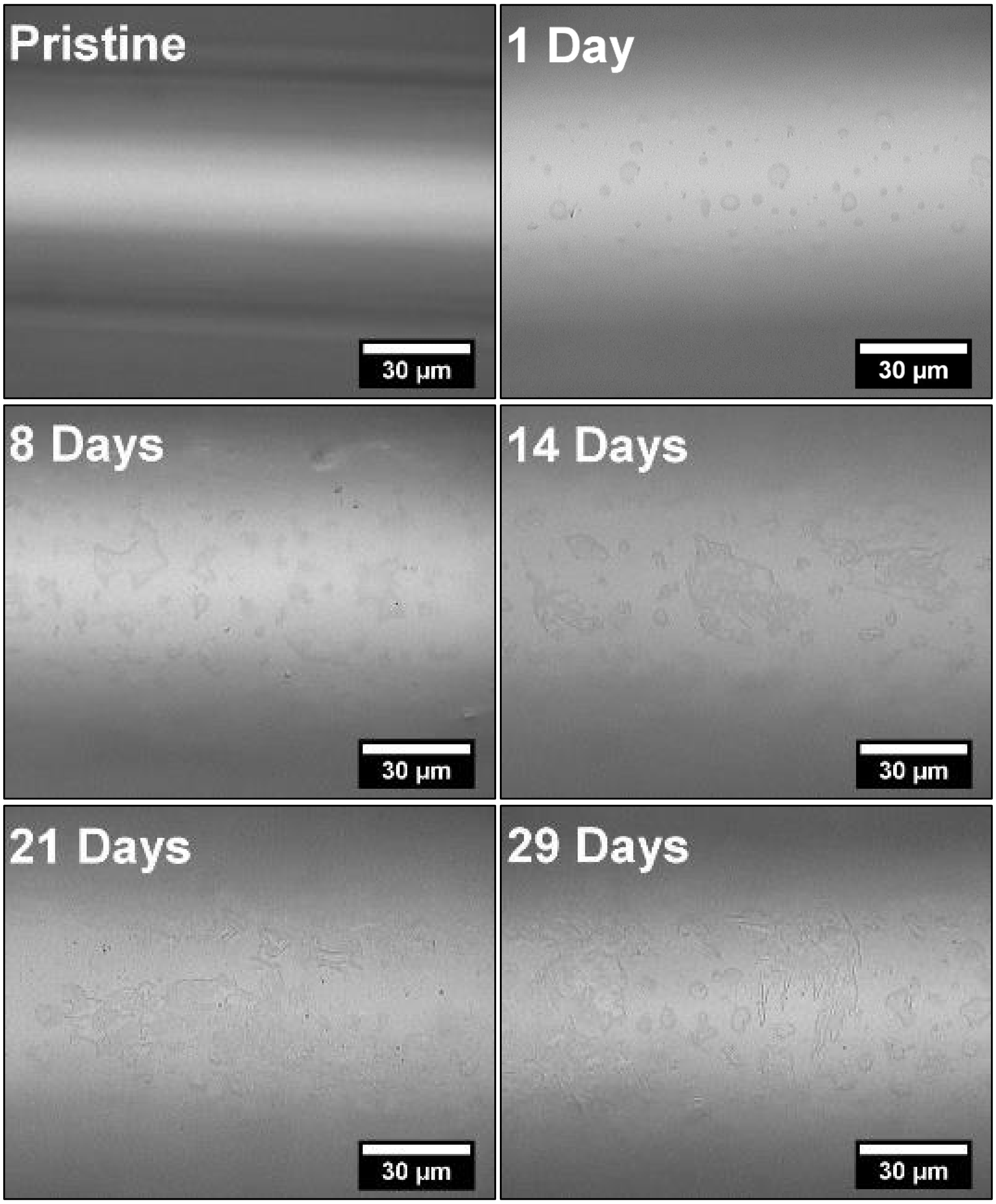

Figure C.3. Flint glass fibers after weathering in 80%RH/50°C air for 29 days.

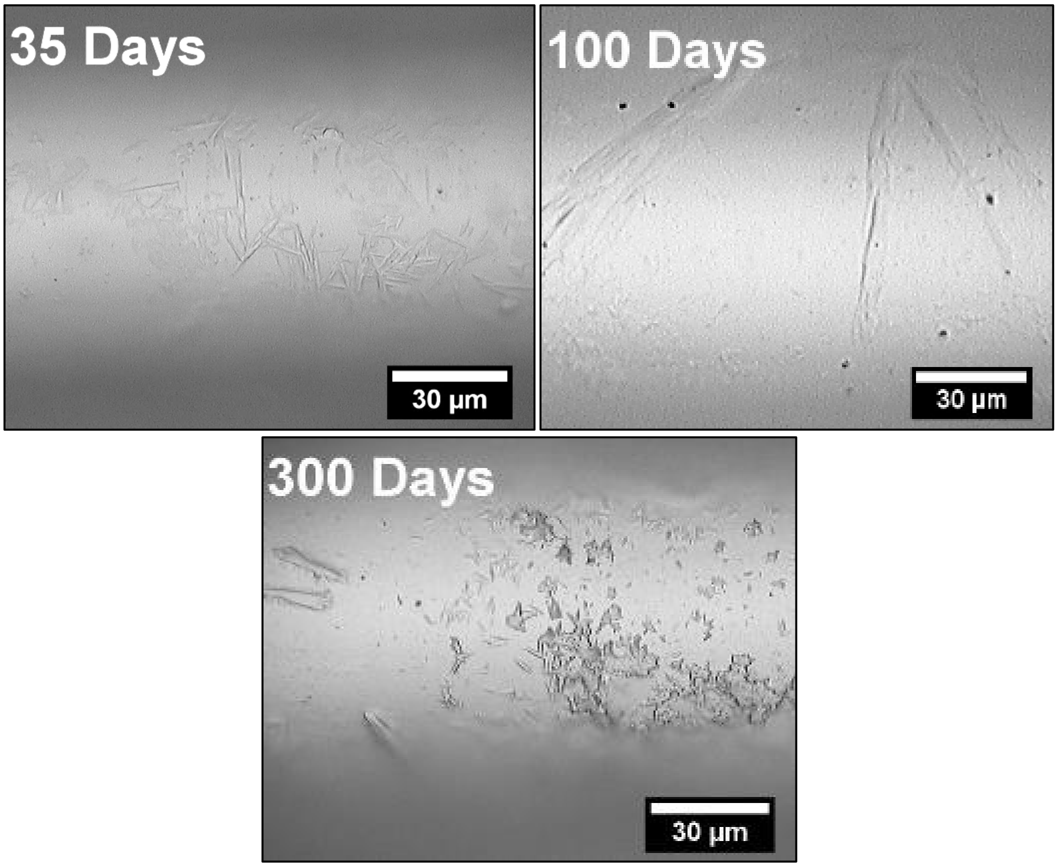

Figure C.4. Flint glass fibers after weathering in 80%RH/50°C air for 300 days.

APPENDIX D.

WEATHERING OF GLASS FIBERS IN VARIED HUMIDITIES

OVERVIEW

Soda-lime silicate OI-A glass bottles provide by Owen-Illinois, Inc. The bottles were re-melted in a platinum crucible at 1450°C in air for four hours to produce a well-conditioned, bubble-free melt. The well-conditioned, bubble free glass melt was transferred into the box furnace and left for four hours at 1220°C, the 1000 P isokom temperature reported by Tang[44]. The melt was then cooled to the fiber-pulling temperature of 1135°C. A silica glass rod is used to draw the initial fiber from the melt onto a rotating cage. The cage is designed to separate individual fibers and ensure a pristine glass surface.

To examine the effect of humidity on failure strains at lower values of relative humidity, a set of fibers was pulled and separated into four groups and weathered at 50°C in a vacuum chamber (~700 Torr, Lab-Line Squaroid Duo-Vac Oven) and in air with a relative humidity of 10%, 18%, and 41%. For weathering in 10%RH, a Lindberg Blue furnace was used. To obtain relative humidities of 18% and 41% at 50°C, saturated salt solutions were made by using Lithium Chloride and Potassium Carbonate, respectively[157], and placed in heated ovens (Boekel Industries) set at 50°C. Relative humidity and temperature for the 10%, 18%, and 41% humidity experiments were measured once a day using the Extech RH305 psychrometer.

Fibers were tested using two-point bend (TPB) technique and were typically 100-150 microns in diameter. In a TPB test, fibers bent in the a ‘U’ shape and placed in between two parallel faceplates. The parallel faceplates then compress the bent fiber at constant rate until the fiber breaks. The distance at break can be used to calculate the failure strain of the fibers. The failure strain (ε_f) was determined from the break distance (D) and fiber diameter (d) using [91]:

$$\varepsilon_f = \frac{1.198 \times d}{(D - d)}$$

A faceplate of 4000μm/s was used. Failure strains were determined as a function of weathering time for both ambient conditions (room temperature air at 40%RH (Figure D.1.)) and under liquid nitrogen (Figure D.2.). The surface of the fibers was examined with scanning electron microscopy periodically throughout the weathering period.

RESULTS

Every set of fibers exhibited an initial increase in failure strain, reaching a maximum after two days. Figure D.3. summarizes the humidity dependence of the increase in the two-day failure strain values, relative to the respective pristine values, and show that fibers weathered in 18%RH air had the largest overall increase in failure strain with an increase in failure strains of 20% in ambient testing and 27% in inert testing. In addition, the relative increases in failure strains for the two-day weathered fibers measured in liquid nitrogen were consistently greater than those measured in ambient air (room temperature, 40%RH).

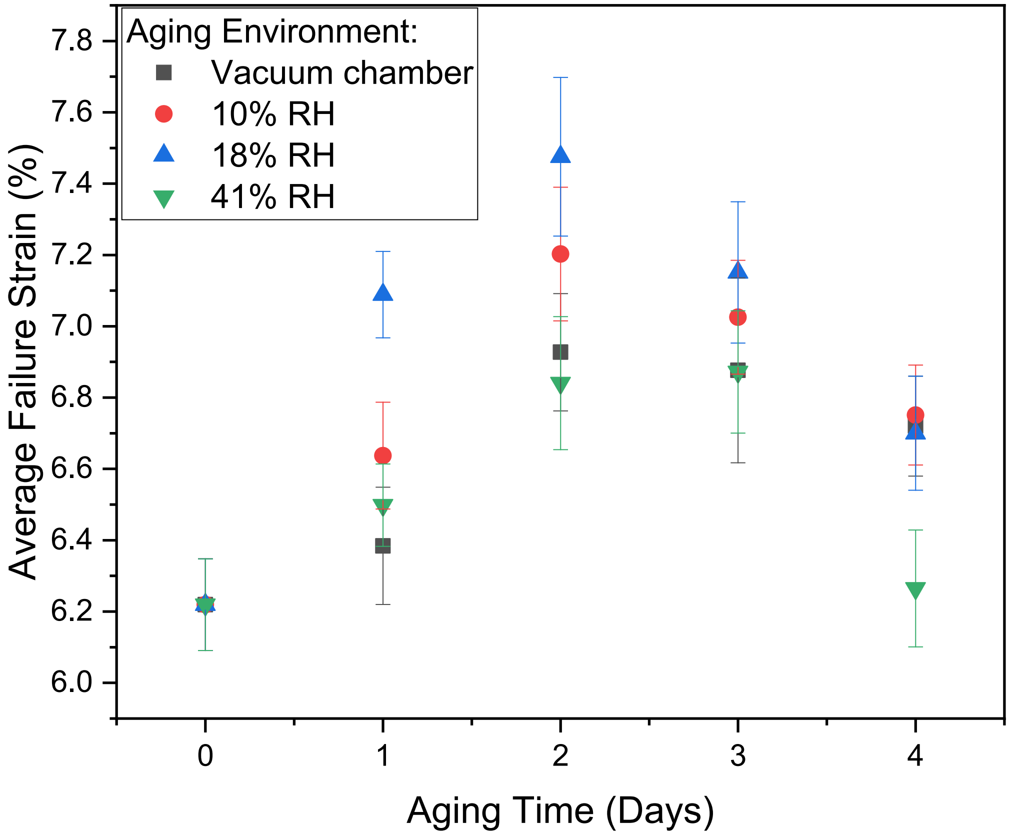

Figure D. 1. Average failure strains of OI-B fibers weathered in 50°C air with different levels of humidity, tested in room temperature 40%RH air at 4000μm/sec.

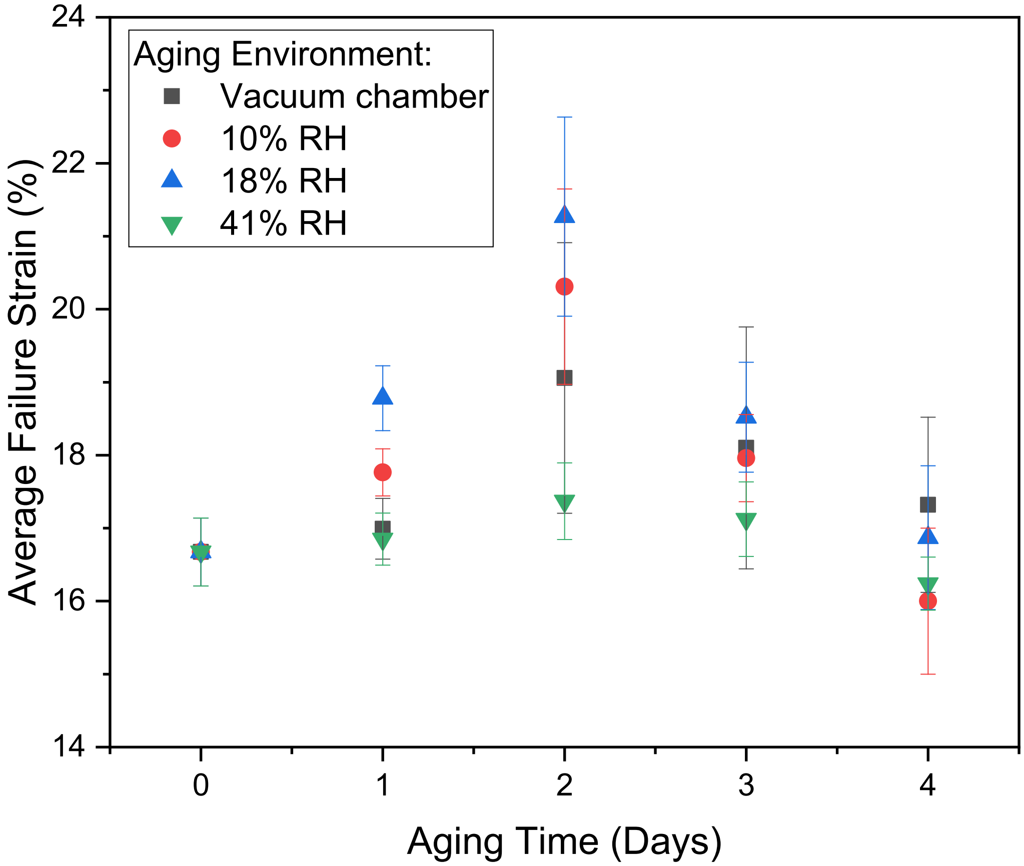

Figure D.2. Average failure strains of OI-B fibers weathered in 50°C air with different levels of humidity and tested in liquid nitrogen at 4000µm/sec.

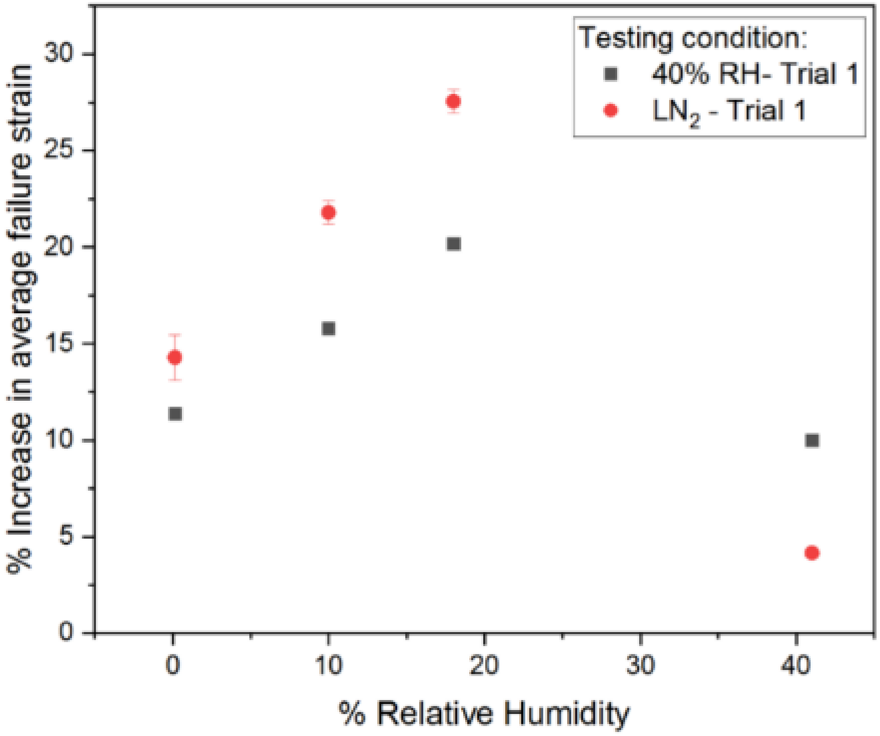

Figure D.3. Percent increase in average failure strains for OI-B fibers weathered for 2 days in air with different levels of humidity and measured in ambient air or liquid nitrogen. It was assumed that the humidity of the vacuum chamber was below 10%RH.

Figure D.4 shows scanning electron microscopic images of fiber surfaces after 3 days of weathering. The surfaces of fibers weathered in vacuum and 10%RH air appear to have sub-micron deposits on their surfaces, similar to the deposits shown in Figure 4.28. The fibers weathered in 41%RH appear to have largest particles at ~0.5 microns. EDS analyses (not shown) indicate no significant compositional differences for the surfaces of fibers weathered in vacuum, 10%RH, and 41%RH environments. On the other hand, the fibers weathered in 18%RH show ~5 micron sized deposits in addition to the sub-micron deposits, and EDS found evidence for chlorine on the surfaces of fibers weathered for 4 days (Table D.1.).

The presence of features on the vacuum-weathered fiber surfaces indicate that they were deposited on the sample surfaces and are not necessarily the result of surface corrosion. The vacuum chamber was not flushed with dry air and was opened twice prior SEM analysis on day three. Therefore, it can be assumed that there was exposure to humidity for brief periods over the weathering period resulting in the growth of features observed in Figure D.4. It is likely given the larger feature size of samples weathered in higher humidities that water assists in coalescence and growth of the droplet features over time.

Table D.1. EDS analysis of surface feature on fibers weathered for 3 days in 18%RH/50^{o}C conditions compared to a pristine fiber surface.

Element (wt%)	18%RH	Pristine
O	29.26±0.3	44.12±0.25
Na	16.19±0.22	10.18±0.13
Mg	0.72±0.09	1.18±0.09
Al	0.50±0.1	0.62±0.09
Si	23.70±0.31	36.40±0.23
Ca	4.53±0.88	7.51±0.28
Cl	25.1±0.42	-

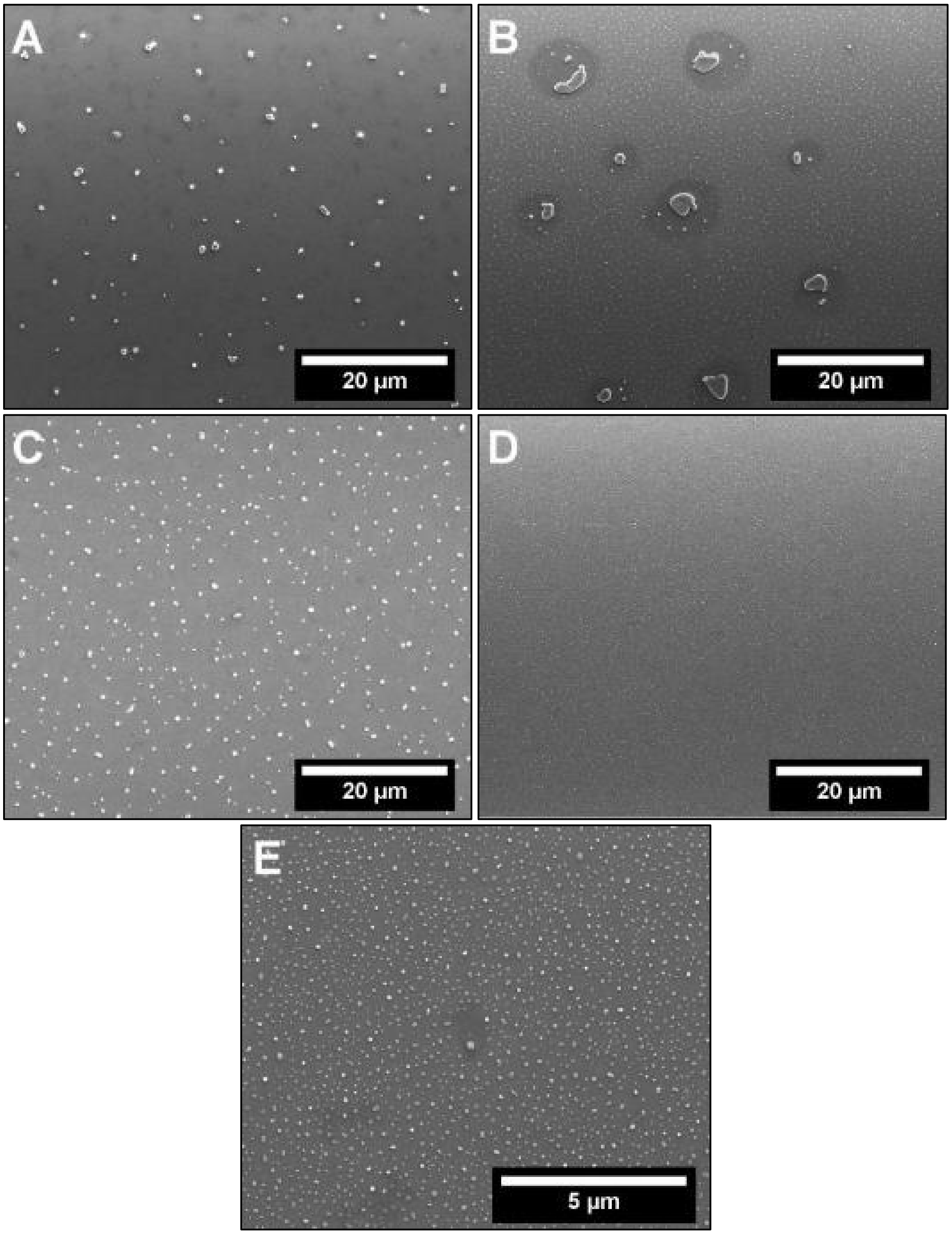

Figure D.4. SEM images of OI-B fibers weathered 3 days at 50^{o}C in (A) 10%RH (B) 18%RH (C) 40% RH (D & E) Vacuum at ~700torr.

BIBLIOGRAPHY

[1] A. K. Varshneya, *Fundamentals of inorganic glasses*. Elsevier, 2013.

[2] J. C. Mauro, "Grand challenges in glass science," *Front. Mater.*, vol. 1, p. 20, 2014.

[3] J. C. Mauro, C. S. Philip, D. J. Vaughn, and M. S. Pambianchi, "Glass science in the United States: Current status and future directions," *Int. J. Appl. Glas. Sci.*, vol. 5, pp. 2–15, 2014.

[4] C. R. Kurkjian, P. K. Gupta, and R. K. Brow, "The Strength of Silicate Glasses: What Do We Know, What Do We Need to Know?," *Int. J. Appl. Glas. Sci.*, vol. 1, pp. 27–37, 2010.

[5] C. R. Kurkjian, P. K. Gupta, R. K. Brow, and N. Lower, "The intrinsic strength and fatigue of oxide glasses," *J. Non. Cryst. Solids*, vol. 316, no. 1, pp. 114–124, 2003.

[6] B. Lawn, *Fracture of brittle solids*. Cambridge university press, 1993.

[7] E. Condon, "A theory of intensity distribution in band systems," *Phys. Rev.*, vol. 28, no. 6, p. 1182, 1926.

[8] E. Orowan, "No Title," *Zeitschrift für Krist.*, vol. 89, p. 327, 1934.

[9] E. Orowan, "Fracture and strength of solids," *Reports Prog. Phys.*, vol. 12, no. 1, p. 185, 1949.

[10] C. E. Inglis, "Stresses in a plate due to the presence of cracks and sharp corners," *Trans Inst Nav. Arch.*, vol. 55, pp. 219–241, 1913.

[11] A. A. Griffith, "VI. The phenomena of rupture and flow in solids," *Philos. Trans. R. Soc. london. Ser. A, Contain. Pap. a Math. or Phys. character*, vol. 221, no. 582–593, pp. 163–198, 1921.

[12] Irwin, "No Title," *Weld. J.*, vol. 32, p. 450, 1952.

[13] F. Barras, D. S. Kammer, P. H. Geubelle, and J.-F. Molinari, "A study of frictional contact in dynamic fracture along bimaterial interfaces," *Int. J. Fract.*, vol. 189, no. 2, pp. 149–162, Oct. 2014.

[14] S. M. Cox, "Glass strength and ion mobility," *Phys. Chem. Glas.*, vol. 10, no. 6, p. 226, 1969.

[15] N. J. Petch, "The fracture of metals," *Prog. Met. Phys.*, vol. 5, pp. 1–52, Jan. 1954.

[16] E. F. Poncelet, "Fracturing of Metals," *Am. Soc. Met.*, p. 201, 1948.

[17] E. D. Zanotto and F. A. B. Coutinho, "How many non-crystalline solids can be made from all the elements of the periodic table?," *J. Non. Cryst. Solids*, vol. 347, no. 1–3, pp. 285–288, 2004.

[18] J. C. Mauro, P. K. Gupta, and R. J. Loucks, "Continuously broken ergodicity," *J. Chem. Phys.*, vol. 126, no. 18, p. 184511, 2007.

[19] F. Faupel *et al.*, "Diffusion in metallic glasses and supercooled melts," *Rev. Mod. Phys.*, vol. 75, no. 1, pp. 237–280, Feb. 2003.

[20] S. Amma, J. Luo, S. H. Kim, and C. G. Pantano, "Effects of fictive temperature on the leaching of soda lime silica glass surfaces," *J. Am. Ceram. Soc.*, vol. 100, no. 4, pp. 1424–1431, Apr. 2017.

[21] A. Koike and M. Tomozawa, "Fictive temperature dependence of subcritical crack growth rate of normal glass and anomalous glass," *J. Non. Cryst. Solids*, vol. 352, no. 52–54, pp. 5522–5530, Dec. 2006.

[22] B. Varughese, Y.-K. Lee, and M. Tomozawa, "Effect of fictive temperature on mechanical strength of soda-lime glasses," *J. Non. Cryst. Solids*, vol. 241, no. 2–3, pp. 134–139, Nov. 1998.

[23] H. Li, A. Agarwal, and M. Tomozawa, "Effect of Fictive Temperature on Dynamic Fatigue Behavior of Silica and Soda-Lime Glasses," *J. Am. Ceram. Soc.*, vol. 78, no. 5, pp. 1393–1396, May 1995.

[24] R. K. Brow, N. P. Lower, C. R. Kurkjian, and H. Li, "The effects of melt history on the failure characteristics of pristine glass fibres," *Phys. Chem. Glas. Eur. J. Glas. Sci. Technol. Part B*, vol. 50, no. 1, pp. 31–33, 2009.

[25] A. Kucuk, A. G. Clare, and L. E. Jones, "Differences between surface and bulk properties of glass melts I," *J. Non. Cryst. Solids*, vol. 261, pp. 28–38, 2000.

[26] J. F. SPROULL and G. E. RINDONE, "Effect of Melting History on the Mechanical Properties of Glass: I, Role of Melting Time and Atmosphere," *J. Am. Ceram. Soc.*, vol. 57, no. 4, pp. 160–164, Apr. 1974.

[27] M. Cameron, "- Relation Between Melt Treatment and Glass Fiber Strenght," *J. Am. Ceram. Soc.*, vol. 49, no. 3, pp. 144–148, 1965.

[28] J. F. SPROULL and G. U. Y. E. RINDONE, "Effect of Melting History on the Mechanical Properties of Glass: II, Effects of Raw Materials and Bubbling Gases Through the Melt," *J. Am. Ceram. Soc.*, vol. 58, no. 1-2, pp. 35–37, 1975.

[29] W. F. Thomas, “An Investigation of the Factors Likely to Affect the Strength and Properties of Glass Fibers,” *Phys. Chem. Glas.*, vol. 1, pp. 14–18, 1960.

[30] N. P. Lower, “Failure Studies of Glass Fibers,” pp. 308–311, 2004.

[31] R. K. Brow, N. P. Lower, C. R. Kurkjian, and H. Li, “The effects of melt history on the failure characteristics of pristine glass fibres,” 2009.

[32] G. E. Rindone, “Effects of Melting History on Properties of Glass,” *Glas. Ind.*, vol. 50, no. 3, pp. 138–143, 1969.

[33] J. F. SPROULL and G. U. Y. E. RINDONE, “Effect of melting history on the mechanical properties of glass: I, role of melting time and atmosphere,” *J. Am. Ceram. Soc.*, vol. 57, no. 4, pp. 160–164, 1974.

[34] S. M. Wiederhorn, T. Fett, J.-P. Guin, and M. Ciccotti, “Griffith Cracks at the Nanoscale,” 2013.

[35] J. E. Ritter Jr, “Dynamic Fatigue of Soda-Lime-Silica Glass,” *J. Appl. Phys.*, vol. 40, no. 1, pp. 340–344, 1969.

[36] M. Kolli, M. Hamidouche, N. Bouaouadja, and G. Fantozzi, “HF etching effect on sandblasted soda-lime glass properties,” *J. Eur. Ceram. Soc.*, vol. 29, no. 13, pp. 2697–2704, Oct. 2009.

[37] N. E. Sipe and N. Ida, “Process of strengthening glass bottles and the like.” Google Patents, 02-Aug-1977.

[38] C. R. Kennedy *et al.*, “Static fatigue of glass. I,” *J. Appl. Phys.*, vol. 29, no. 11, pp. 392–400, 1958.

[39] N. P. Lower, R. K. Brow, and C. R. Kurkjian, “Inert failure strain studies of sodium silicate glass fibers,” *J. Non. Cryst. Solids*, vol. 349, pp. 168–172, 2004.

[40] N. P. Lower, R. K. Brow, and C. R. Kurkjian, “Inert failure strains of sodium aluminosilicate glass fibers,” *J. Non. Cryst. Solids*, vol. 344, no. 1–2, pp. 17–21, 2004.

[41] Z. Tang, N. P. Lower, P. K. Gupta, C. R. Kurkjian, and R. K. Brow, “Using the two-point bend technique to determine failure stress of pristine glass fibers,” *J. Non. Cryst. Solids*, vol. 428, pp. 98–104, Nov. 2015.

[42] Z. Tang and R. K. Brow, “Environmental Fatigue of Silicate Glasses in Humid Conditions,” *Int. J. Appl. Glas. Sci.*, vol. 5, no. 3, pp. 287–296, Sep. 2014.

[43] N. P. Lower, “Failure Studies of Glass Fibers,” University of Missouri-Rolla, 2004.

[44] Z. Tang, “Two-point Bend Studies of Glass Fibers,” Missouri University of Science and Technology, 2011.

[45] M. D. Lund and Y. Yue, “Impact of drawing stress on the tensile strength of oxide glass fibers,” *J. Am. Ceram. Soc.*, vol. 93, pp. 3236–3243, 2010.

[46] M. E. Lynch, D. C. Folz, and D. E. Clark, “Use of FTIR reflectance spectroscopy to monitor corrosion mechanisms on glass surfaces,” *J. Non. Cryst. Solids*, vol. 353, no. 27, pp. 2667–2674, 2007.

[47] M. H. Krohn, J. R. Hellmann, D. L. Shelleman, C. G. Pantano, G. E. Sakoske, and F. Corporation, “Biaxial Flexure Strength and Dynamic Fatigue of Soda – Lime – Silica Float Glass,” *J. Am. Ceram. Soc.*, vol. 85, pp. 1777–1782, 2002.

[48] H. G. M. Edwards *et al.*, “SIMS Analysis of Aqueous Corrosion Profiles in Soda-Lime-Silica Glass,” *J. Non. Cryst. Solids*, vol. 28, no. 23, pp. 601–604, 2005.

[49] L. Grenet, “Mechanical Strength of Glass,” *Bull. SOC. Ayer. Sci*, vol. 4, no. 5, pp. 838–48, 1899.

[50] R. J. Charles, “Static Fatigue of Glass. II,” *J. Appl. Phys.*, vol. 29, no. 11, pp. 1554–1560, Nov. 1958.

[51] R. J. Charles, “Dynamic fatigue of glass,” *J. Appl. Phys.*, vol. 29, pp. 1657–1662, 1958.

[52] R. J. Charles, “A review of glass strength,” *Prog. Ceram. Sci.*, vol. 1, pp. 1–38, 1961.

[53] R. J. Charles, “Static fatigue of glass. I,” *J. Appl. Phys.*, vol. 29, no. 11, pp. 1549–1553, 1958.

[54] S. M. Wiederhorn, “Influence of Water Vapor on Crack Propagation in Soda-Lime Glass,” *J. Am. Ceram. Soc.*, vol. 50, no. 8, pp. 407–414, 1967.

[55] J. L. Armstrong, M. J. Matthewson, and C. R. Kurkjian, “Humidity Dependence of the Fatigue of High-Strength Fused Silica Optical Fibers,” *J. Am. Ceram. Soc.*, vol. 83, no. 12, pp. 3100–3109, 2000.

[56] T. Fett, J. P. Guin, and S. M. Wiederhorn, “Stresses in ion-exchange layers of soda-lime-silicate glass,” *Fatigue Fract. Eng. Mater. Struct.*, vol. 28, no. 6, pp. 507–514, 2005.

[57] T. A. Michalske and S. W. Freiman, “A Molecular Mechanism for Stress Corrosion in Vitreous Silica.”

[58] A. G. Evans, “Slow crack growth in brittle materials under dynamic loading conditions,” *Int. J. Fract.*, vol. 10, no. 2, pp. 251–259, 1974.

[59] Y. S. Shiue and M. J. Matthewson, “Stress dependent activation entropy for dynamic fatigue of pristine silica optical fibers,” *J. Appl. Phys.*, vol. 89, no. 9, pp. 4787–4793, May 2001.

[60] B. R. Lawn, “An atomistic model of kinetic crack growth in brittle solids,” *J. Mater. Sci.*, vol. 10, no. 3, pp. 469–480, 1975.

[61] J. C. Pollet and S. J. Burns, “Thermally activated crack propagation—theory,” *Int. J. Fract.*, vol. 13, no. 5, pp. 667–679, 1977.

[62] R. J. Charles, “Diffusion controlled stress rupture of polycrystalline materials,” *Metall. Trans. A*, vol. 7, no. 8, pp. 1081–1089, 1976.

[63] W. A. Smith and T. M. Michalske, “DOE contract# DE-AC04-0DPOO789,(1990),” *There is no Corresp. Rec. this Ref. Sch.*

[64] W. J. Duncan, P. W. France, and S. P. Craig, “The effect of environment on the strength of optical fiber,” *Strength Inorg. Glas.*, pp. 309–328, 1983.

[65] V. A. Bogatyrjov, M. M. Bubnov, E. M. Dianov, A. M. Prokhorov, S. D. Rumyantsev, and S. L. Semenov, “High strength hermetically sealed optical fibers,” *Soy. Tech. Phys. Lett*, vol. 14, no. 5, p. 343, 1988.

[66] C. R. Kurkjian and P. K. Gupta, “Intrinsic Strength and the Structure of Glass,” *Proc. XIX Int. Congr. Glas.*, vol. 1, p. 11, 2001.

[67] B. C. Bunker, “Molecular mechanisms for corrosion of silica and silicate glasses,” *J. Non. Cryst. Solids*, vol. 179, pp. 300–308, Nov. 1994.

[68] N. Papadopoulos and C. A. Drosou, “INFLUENCE OF WEATHER CONDITIONS ON GLASS PROPERTIES.,” *J. Univ. Chem. Technol. Metall.*, vol. 47, no. 4, 2012.

[69] W. a. Lanford, K. Davis, P. Lamarche, T. Laursen, R. Groleau, and R. H. Doremus, “Hydration of soda-lime glass,” *J. Non. Cryst. Solids*, vol. 33, pp. 249–266, 1979.

[70] M. H. Chopinet *et al.*, “Soda-lime-silica glass containers: chemical durability and weathering products,” in *Advanced Materials Research*, 2008, vol. 39, pp. 303–308.

[71] M. Verità, R. Falcone, G. Sommariva, M.-H. Chopinet, and P. Lehuédé, “Weathering of the inner surface of soda–lime–silica glass containers exposed to the atmosphere,” *Glas. Technol. J. Glas. Sci. Technol. Part A*, vol. 50, no. 1, pp. 65–70, 2009.

[72] M. M. Smedskjaer, Q. Zheng, J. C. Mauro, M. Potuzak, S. Mørup, and Y. Yue, "Sodium diffusion in boroaluminosilicate glasses," *J. Non. Cryst. Solids*, vol. 357, no. 22–23, pp. 3744–3750, Nov. 2011.

[73] M. M. Smedskjaer, J. C. Mauro, and Y. Yue, "Prediction of Glass Hardness Using Temperature-Dependent Constraint Theory," *Phys. Rev. Lett.*, vol. 105, no. 11, p. 115503, Sep. 2010.

[74] M. M. Smedskjaer, J. C. Mauro, S. Sen, and Y. Yue, "Quantitative Design of Glassy Materials Using Temperature-Dependent Constraint Theory," *Chem. Mater.*, vol. 22, no. 18, pp. 5358–5365, Sep. 2010.

[75] F. Célarié *et al.*, "Glass Breaks like Metal, but at the Nanometer Scale," *Phys. Rev. Lett.*, vol. 90, no. 7, p. 075504, Feb. 2003.

[76] A. Kelly, W. R. Tyson, and A. H. Cottrell, "Ductile and brittle crystals," *Philos. Mag. A J. Theor. Exp. Appl. Phys.*, vol. 15, no. 135, pp. 567–586, 1967.

[77] J. R. Rice and R. Thomson, "Ductile versus brittle behaviour of crystals," *Philos. Mag. A J. Theor. Exp. Appl. Phys.*, vol. 29, no. 1, pp. 73–97, Jan. 1974.

[78] T. Taniguchi, "Deformation of soda–lime–silica glass under pressure and stress by molecular dynamics simulation," *Phys. Chem. Glas.*, vol. 45, no. 3, pp. 183–191, 2004.

[79] T. Taniguchi and S. Ito, "Deformation and fracture of soda-lime-silica glass under tension by molecular dynamics simulation," *J. Ceram. Soc. Japan*, vol. 116, no. 1356, pp. 885–889, 2008.

[80] T. Taniguchi and S. Ito, "Structure and mechanical property of water-containing soda–alumina–silica glass by molecular dynamics simulation," *J. Non. Cryst. Solids*, vol. 432, pp. 177–182, Jan. 2016.

[81] S. H. Garofalini, "Molecular dynamics computer simulations of silica surface structure and adsorption of water molecules," *J. Non. Cryst. Solids*, vol. 120, no. 1–3, pp. 1–12, Apr. 1990.

[82] E. A. Leed and C. G. Pantano, "Computer modeling of water adsorption on silica and silicate glass fracture surfaces," *J. Non. Cryst. Solids*, vol. 325, no. 1–3, pp. 48–60, Sep. 2003.

[83] A. Tilocca and A. N. Cormack, "The initial stages of bioglass dissolution: a Car-Parrinello molecular-dynamics study of the glass-water interface," *Proc. R. Soc. A Math. Phys. Eng. Sci.*, vol. 467, no. 2131, pp. 2102–2111, Jul. 2011.

[84] A. Tilocca and A. N. Cormack, “Exploring the Surface of Bioactive Glasses: Water Adsorption and Reactivity,” *J. Phys. Chem. C*, vol. 112, no. 31, pp. 11936–11945, Aug. 2008.

[85] J. Du and A. N. Cormack, “Molecular Dynamics Simulation of the Structure and Hydroxylation of Silica Glass Surfaces,” *J. Am. Ceram. Soc.*, vol. 88, no. 9, pp. 2532–2539, Sep. 2005.

[86] V. P. Pukh, L. G. Baikova, M. F. Kireenko, L. V Tikhonova, T. P. Kazannikova, and A. B. Sinani, “Atomic structure and strength of inorganic glasses,” *Phys. Solid State*, vol. 47, no. 5, pp. 876–881, 2005.

[87] C. R. Kennedy, R. C. Bradt, and G. E. Rindone, “Strength of binary alkali silicate glasses,” *Phys. Chem. Glas.*, vol. 21, pp. 99–105, 1980.

[88] L. G. Baikova, K. Ullner, and V. P. Pukh, “Determination of the fatigue parameters of soda-lime-silicate glass in measurement of strength by different methods,” *Sov. J. Glas. Phys. Chem. Transl.*, vol. 17, no. 5, pp. 418–424, 1991.

[89] P. K. Gupta, “No Title,” in *Proceedings of the Euroconference of High Performance Fibers*, 2000, pp. 19–24.

[90] R. K. Brow, N. P. Lower, and C. R. Kurkjian, “TPB test provides new insight to fiber strength, quality,” *Am. Ceram. Soc. Bull.*, vol. 84, no. October, pp. 50–54, 2005.

[91] M. J. Matthewson, C. R. Kurkjian, and S. T. Gulati, “Strength measurement of opticaal fibers by bending,” *J. Am. Ceram. Sosiety*, vol. 69, pp. 815–21, 1986.

[92] C. R. Kurkjian and U. C. Paek, “Single-valued strength of ‘“perfect”’silica fibers,” *Appl. Phys. Lett.*, vol. 42, no. 3, pp. 251–253, 1983.

[93] C. R. Kurkjian, “From griffith flaws to perfect fibers a history of glass research,” *J. Non. Cryst. Solids*, vol. 73, no. 1–3, pp. 265–271, 1985.

[94] M. J. Matthewson and C. R. Kurkjian, “Static fatigue of optical fibers in bending,” *J. Am. Ceram. Soc.*, vol. 70, no. 9, pp. 662–668, 1987.

[95] R. J. Castilone and T. A. Hanson, “Strength and Dynamic fatigue characteristics of aged fiber,” *Corning Inc., Corning, NY*, 1998.

[96] P. W. France, M. J. Paradine, M. H. Reeve, and G. R. Newns, “Liquid nitrogen strengths of coated optical glass fibres,” *J. Mater. Sci.*, vol. 15, no. 4, pp. 825–830, Apr. 1980.

[97] Y. S. Shiue and M. J. Matthewson, “Stress dependent activation entropy for dynamic fatigue of pristine silica optical fibers,” *J. Appl. Phys.*, vol. 89, no. 9, pp. 4787–4793, 2001.

[98] V. V Rondinella and M. J. Matthewson, “Effect of Loading Mode and Coating on Dynamic Fatigue of Optical Fiber in Two-Point Bending,” *J. Am. Ceram. Soc.*, vol. 76, no. 1, pp. 139–144, 1993.

[99] P. K. Gupta and C. R. Kurkjian, “Intrinsic failure and non-linear elastic behavior of glasses,” *J. Non. Cryst. Solids*, vol. 351, no. 27–29, pp. 2324–2328, 2005.

[100] M. Tomozawa, “Fracture of glasses,” *Annu. Rev. Mater. Sci.*, vol. 26, no. 1, pp. 43–74, 1996.

[101] S. Yoshida, A. Hidaka, and J. Matsuoka, “Crack initiation behavior of sodium aluminosilicate glasses,” *J. Non. Cryst. Solids*, vol. 344, no. 1–2, pp. 37–43, 2004.

[102] R. K. Brow, N. P. Lower, A. J. Lang, and C. R. Kurkjian, “Structure and the intrinsic strength of glass,” *Glas. Sci. Technol.*, vol. 75, pp. 133–138, 2002.

[103] S. Ito, T. Taniguchi, M. Ono, and K. Uemura, “Network and void structures for glasses with a higher resistance to crack formation,” *J. Non. Cryst. Solids*, vol. 358, no. 24, pp. 3453–3458, Dec. 2012.

[104] A. Koike, M. Tomozawa, and S. Ito, “Sub-critical crack growth rate of soda-lime-silicate glass and less brittle glass as a function of fictive temperature,” *J. Non. Cryst. Solids*, vol. 353, no. 27, pp. 2675–2680, Aug. 2007.

[105] S. Yoshida, Y. Nishikubo, A. Konno, T. Sugawara, Y. Miura, and J. Matsuoka, “Fracture-and indentation-induced structural changes of sodium borosilicate glasses,” *Int. J. Appl. Glas. Sci.*, vol. 3, no. 1, pp. 3–13, 2012.

[106] P. J. Lezzi and M. Tomozawa, “An Overview of the Strengthening of Glass Fibers by Surface Stress Relaxation,” 2015.

[107] P. J. Lezzi, M. Tomozawa, and T. A. Blanchet, “Evaluation of residual curvature in two-point bent glass fibers,” *J. Non. Cryst. Solids*, vol. 364, pp. 77–84, Mar. 2013.

[108] J. H. Seaman, P. J. Lezzi, T. A. Blanchet, and M. Tomozawa, “Degradation of ion-exchange strengthened glasses due to surface stress relaxation,” *J. Non. Cryst. Solids*, vol. 403, pp. 113–123, Nov. 2014.

[109] P. J. Lezzi, E. E. Evke, E. M. Aaldenberg, and M. Tomozawa, “Surface Crystallization and Water Diffusion of Silica Glass Fibers: Causes of Mechanical Strength Degradation,” 2015.

[110] Q. Wang, R. K. Brow, H. Li, and E. A. Ronchetto, "Effect of aging on the failure characteristics of E-glass fibers," *J. Mater. Sci.*, vol. 51.

[111] Q. Wang, H. Li, and E. A. Ronchetto, "Effects of ageing conditions on E-glass failure strain and dynamic fatigue Effect of Iron oxide on the E glass for PPG company View project Glass for Optical and Laser Applications View project," *Eur. J. Glas. Sci. Technol. Part A*, vol. 57, no. 2, pp. 58–61, 2016.

[112] W. Weibull, "A statistical theory of strength of materials," *IVB-Handl.*, 1939.

[113] M. F. Kireenko and V. P. Pukh, "The Influence of Temperature and the Medium on the Macrocrack Growth Rate in the Glass," *Fiz. Khim. Stekla.*, vol. 16, no. 4, pp. 571–576, 1990.

[114] H. Richter, "Zum Einfluss umgebender Medien auf die Rissausbreitung in Glas in einem Zwischenbereich von Bruchgeschwindigkeiten," *Glas. Ber*, vol. 56, no. 1, pp. 402–407, 1983.

[115] V. M. Sglavo and D. J. Green, "Influence of indentation crack configuration on strength and fatigue behaviour of soda-lime silicate glass," *Acta Metall. Mater.*, vol. 43, no. 3, pp. 965–972, 1995.

[116] C. Peuker, U. Reinholz, C. Jäger, J. Pauli, and H. Geißler, "Extinction coefficients of the OH bands in the IR spectra of basic and water-enriched silicate and aluminosilicate glasses," 2003.

[117] A. Stuke, H. Behrens, B. C. Schmidt, and R. Dupree, "H2O speciation in float glass and soda lime silica glass," *Chem. Geol.*, vol. 229, no. 1–3, pp. 64–77, May 2006.

[118] U. K. Vempati and T. J. Clark, "Effect of Dissolved Water on Physical Properties of Soda-Lime-Silicate Glasses," John Wiley & Sons, Ltd, 2015, pp. 1–12.

[119] J. Deubener, H. Behrens, R. Müller, S. Zietka, and S. Reinsch, "Kinetic fragility of hydrous soda-lime-silica glasses," *J. Non. Cryst. Solids*, vol. 354, no. 42–44, pp. 4713–4718, 2008.

[120] A. L. Ruoff, "On the ultimate yield strength of solids," *J. Appl. Phys.*, vol. 49, no. 1, pp. 197–200, 1978.

[121] D. Cavaill, "Third-order elastic constants determination in soda ± lime ± silica glass by Brillouin scattering," vol. 260, pp. 235–241, 1999.

[122] F. M. Ernsberger, "Detection of Strength-Impairing Surface Flaws in Glass," *Proc. R. Soc. A Math. Phys. Eng. Sci.*, vol. 257, pp. 213–223, 1960.

[123] Y. Chiang, D. P. Birnie, and W. D. Kingery, *Physical ceramics*. J. Wiley, 1997.

[124] A. C. Hannon, B. Vessal, and J. M. Parker, “The structure of alkali silicate glasses,” *J. Non. Cryst. Solids*, vol. 150, no. 1–3, pp. 97–102, Nov. 1992.

[125] C. Huang and A. N. Cormack, “Structure and energetics in mixed-alkali-metal silicate glasses from molecular dynamics,” *J. Mater. Chem.*, vol. 2, no. 3, p. 281, Jan. 1992.

[126] T. F. Soules, “A molecular dynamic calculation of the structure of sodium silicate glasses ARTICLES YOU MAY BE INTERESTED IN,” *J. Chem. Phys*, vol. 71, p. 4570, 1979.

[127] J. Barr, “The Glass Tempering Handbook—Understanding the Glass Tempering Process,” *Self Publ.*, 2015.

[128] C. J. R. Gonzalez-Oliver, P. S. Johnson, and P. F. James, “Influence of water content on the rates of crystal nucleation and growth in lithia-silica and soda-lime-silica glasses,” *J. Mater. Sci.*, vol. 14, pp. 1159–1169, 1979.

[129] P. W. McMillan and A. Chlebik, “The effect of hydroxyl ion content on the mechanical and other properties of soda-lime-silica glass,” *J. Non. Cryst. Solids*, vol. 38–39, pp. 509–514, May 1980.

[130] M. Tomozawa, “Water in glass,” *J. Non. Cryst. Solids*, vol. 73, no. 1–3, pp. 197–204, Aug. 1985.

[131] M. Takata, M. Tomozawa, and E. B. Watson, “Effect of Water Content on Mechanical Properties of Na2O-SiO2 Glasses,” *J. Am. Ceram. Soc.*, vol. 65, no. 9, pp. c156–c157, Sep. 1982.

[132] S. A. Brawer and W. B. White, “Raman spectroscopic investigation of the structure of silicate glasses (II). Soda-alkaline earth-alumina ternary and quaternary glasses,” *J. Non. Cryst. Solids*, vol. 23, no. 2, pp. 261–278, 1977.

[133] M. Wang, J. CHeng, M. Li, and F. He, “Raman spectra of soda–lime–silicate glass doped with rare earth,” *Phys. B Condens. Matter*, vol. 406, no. 20, pp. 3865–3869, Oct. 2011.

[134] H. G. M. Edwards, K. J. Currie, H. R. H. Ali, S. E. J. Villar, A. R. David, and J. Denton, “Raman spectroscopy of natron: shedding light on ancient Egyptian mummification,” *Anal. Bioanal. Chem.*, vol. 388, no. 3, pp. 683–689, 2007.

[135] W. C. LaCourse, “How surface flaws affect glass strength,” *Glas. Ind.*, vol. 68, no. 7, pp. 14–23, 1987.

[136] M. D. Lund and Y. Yue, “Impact of Drawing Stress on the Tensile Strength of Oxide Glass Fibers.”

[137] J. O. Carnali, G. M. Lugo, A. Sharma, and H. Jain, “Inhomogeneous glass surfaces resulting from rapid forming operations–evidence from differential corrosion,” *J. Non. Cryst. Solids*, vol. 341, no. 1–3, pp. 101–109, 2004.

[138] K. C. Datsiou and M. Overend, “The strength of aged glass,” *Glas. Struct. Eng.*, vol. 2, no. 2, pp. 105–120, Oct. 2017.

[139] D. M. Martin, M. Akinc, and S. M. O. O. OH, “Effect of Forming and Aging Atmospheres on E-Glass Strength,” *J. Am. Ceram. Soc.*, vol. 61, no. 7-8, pp. 308–311, 1978.

[140] J. B. Wachtman, W. R. Cannon, and M. J. Matthewson, *Mechanical properties of ceramics*. John Wiley & Sons, 2009.

[141] L. Robinet, C. Hall, K. Eremin, S. Fearn, and J. Tate, “Alteration of soda silicate glasses by organic pollutants in museums: Mechanisms and kinetics,” *J. Non. Cryst. Solids*, vol. 355, no. 28–30, pp. 1479–1488, 2009.

[142] M. M. Curtin Carter, N. S. McIntyre, H. W. King, and a R. Pratt, “The aging of silicate glass surfaces in humid air,” *J. Non. Cryst. Solids*, vol. 220, pp. 127–138, 1997.

[143] L. Robinet, C. Hall, K. Eremin, S. Fearn, and J. Tate, “Alteration of soda silicate glasses by organic pollutants in museums: Mechanisms and kinetics,” *J. Non. Cryst. Solids*, vol. 355, no. 28–30, pp. 1479–1488, 2009.

[144] C. Wang *et al.*, “Study of surface changes on industrial glasses with AFM, FE-SEM, EDX, SNMS and LM,” *Glas. Sci. Technol*, vol. 77, no. 3, p. 103, 2004.

[145] E. Rädlein and G. H. Frischat, “Atomic force microscopy as a tool to correlate nanostructure to properties of glasses,” *J. Non. Cryst. Solids*, vol. 222, pp. 69–82, 1997.

[146] R. Gy, “Stress corrosion of silicate glass: a review,” *J. Non. Cryst. Solids*, vol. 316, no. 1, pp. 1–11, 2003.

[147] D. M. Zirl and S. H. Garofalini, “Reactions on modified silica surfaces,” *J. Non. Cryst. Solids*, vol. 122, no. 2, pp. 111–120, 1990.

[148] K. H. Schnatter, R. H. Doremus, and W. A. Lanford, “Hydrogen analysis of soda-lime silicate glass,” *J. Non. Cryst. Solids*, vol. 102, no. 1–3, pp. 11–18, Jun. 1988.

[149] H. He, L. Qian, C. G. Pantano, and S. H. Kim, “Mechanochemical wear of soda lime silica glass in humid environments,” *J. Am. Ceram. Soc.*, vol. 97, pp. 2061–2068, 2014.

[150] A. Alazizi, A. J. Barthel, N. D. Surdyka, J. Luo, and S. H. Kim, “Vapors in the ambient—A complication in tribological studies or an engineering solution of tribological problems?,” *Friction*, vol. 3, no. 2, pp. 85–114, 2015.

[151] J. Luo, W. Grisales, M. Rabii, C. G. Pantano, and S. H. Kim, “Differences in surface failure modes of soda lime silica glass under normal indentation versus tangential shear: A comparative study on Na $^+$ /K $^+$ -ion exchange effects,” *J. Am. Ceram. Soc.*, vol. 102, no. 4, pp. 1665–1676, Apr. 2019.

[152] J. Luo, H. Huynh, C. G. Pantano, and S. H. Kim, “Hydrothermal reactions of soda lime silica glass – Revealing subsurface damage and alteration of mechanical properties and chemical structure of glass surfaces,” *J. Non. Cryst. Solids*, vol. 452, pp. 93–101, Nov. 2016.

[153] K. Januchta *et al.*, “Breaking the Limit of Micro-Ductility in Oxide Glasses,” *Adv. Sci.*, p. 1901281, Jul. 2019.

[154] J. Luo *et al.*, “Chemical structure and mechanical properties of soda lime silica glass surfaces treated by thermal poling in inert and reactive ambient gases,” *J. Am. Ceram. Soc.*, vol. 101, no. 7, pp. 2951–2964, Jul. 2018.

[155] D. E. Clark, M. F. Dilmore, E. C. Ethridget, and L. L. Hench, “Aqueous corrosion of soda-silica and soda-lime-silica glass,” *J. Am. Ceram. Soc.*, vol. 59, pp. 62–65, 1975.

[156] A. Stuke, H. Behrens, B. C. Schmidt, and R. Dupree, “H2O speciation in float glass and soda lime silica glass,” *Chem. Geol.*, vol. 229, no. 1–3, pp. 64–77, May 2006.

[157] L. Greenspan, “Humidity fixed points of binary saturated aqueous solutions,” *J. Res. Natl. Bur. Stand. Sect. A Phys. Chem.*, vol. 81A, no. 1, p. 89, 1977.

VITA

Erica Ann Ronchetto was born in 1989 in Chesterfield, Missouri to Mary and Gene Ronchetto. She graduated high school from Cor Jesu Academy in St. Louis, Missouri in May 2007. She attended Missouri University of Science and Technology, formerly known as University of Missouri-Rolla, and graduated with her B.S. in Ceramic Engineering in December 2011. She began her graduate work in January 2012 at Missouri University of Science and Technology. In June 2016, she joined the research staff at PARC, A Xerox company in Palo Alto, California while continuing her graduate work at Missouri University of Science and Technology remotely. She received a Ph.D. degree in Materials Science and Engineering from Missouri University of Science and Technology in December 2019.